

# **A Microfluidic Brain Interface for In Vivo Recording of Neurochemical Activity**

THÈSE N° 7816 (2017)

PRÉSENTÉE LE 12 JUILLET 2017

À LA FACULTÉ DES SCIENCES ET TECHNIQUES DE L'INGÉNIEUR

LABORATOIRE DE MICROSYSTÈMES 4

PROGRAMME DOCTORAL EN BIOTECHNOLOGIE ET GÉNIE BIOLOGIQUE

ÉCOLE POLYTECHNIQUE FÉDÉRALE DE LAUSANNE

POUR L'OBTENTION DU GRADE DE DOCTEUR ÈS SCIENCES

PAR

**Guillaume Cédric Yves PETITPIERRE**

acceptée sur proposition du jury:

Prof. D. Pioletti, président du jury  
Prof. Ph. Renaud, directeur de thèse  
Prof. C. Pollo, rapporteur  
Prof. A. Thomas, rapporteur  
Dr B. Schneider, rapporteur



ÉCOLE POLYTECHNIQUE  
FÉDÉRALE DE LAUSANNE

Suisse  
2017



A ma petite nageuse





# Acknowledgements

This work was carried out at the laboratory of microsystems 4 (LMIS4) at the EPFL, but also involved several collaborations. This is the opportunity for me to thank the people I had the chance to meet and work with.

My greatest gratitude goes to my thesis director, Professor Philippe Renaud, for having included me in his team and supported me throughout these years. Philippe is a great person, who has always given me valuable and creative scientific inputs, providing me with the necessary freedom which makes the success of a research project. I believe that both his approach to science and people are extraordinary which certainly contributes to the success of his laboratory.

I had the chance to work in a group of very pleasant and interesting people. I wish to thank David B. and David F. who were always supportive in the good and bad moments, whether it be for providing their expertise in mathematical modeling or for "taking a breath" on a 400 m running track. I also wish to thank Elodie for being such a great person, always supportive and ready to share her expertise in entrepreneurship. My office mates Stefano and Ludovic, with whom we had numerous discussions about scientific and less scientific matters, are thanked for their open-minded attitude and critical thinking. Amélie, Sophie B., Pierre, Fabien and Pietro were always ready to share their expertise or a "late lunch" which was very pleasant. Thank you to Alberto who learned me the art of writing a strong patent. Thanks to Thomas for his generous way to transmit his (huge) knowledge in almost any scientific fields. Thank you to Arnaud for sharing his deep expertise in chemistry and for his precious and valuable contributions during the preparation of this manuscript. Thank you to Marc and Sébastien who were always keen to help. Thanks to Sylvie for being very competent and always of good mood. Thanks to Harald for being always ready to help. Thanks

---

to Carolin, Margaux, Fatemeh, Benoît and Jonathan C. for being nice colleagues. I also would like to express my sincere gratitude to André, a great person and a great entrepreneur, for his support throughout these years. André has always been a Mentor to me, sharing his huge network and deep expertise in neurotechnology and entrepreneurship.

Gratitude is deserved to the students I had the chance to supervise; they contributed to this work and taught me a great deal of soft skills. Thank you to Sophie G., Colin (2x), Renaud, Damien, Mehdi and Tiago.

The team of the neurodegenerative disease laboratory (LEN) provided a great amount of support. I especially wish to thank Philippe Colin for being so competent and helpful during the animal experimentation phase. Bernard, Sameer and Pamela are equally thanked for their strong support throughout these years. Thank you to Aurélien, Julien and Estelle from the Unit of Toxicology (CURML, University Hospitals of Lausanne and Geneva) who shared their deep expertise in mass spectrometry with me. They always made me feel like being part of their team which was very pleasant. Natalia and Liang as well as Jonathan P. M. and Marc M. are thanked for opening their laboratory doors (sometimes late) and sharing their knowledge in mass spectroscopy. I also would like to express my gratitude to Pascal who has always been supportive, open-minded and who is simply a great person. Thanks for opening the doors of your surgery room. A large thanks goes also to Marc B. who has always been supportive and of good advice (despite being on the other side of the Globe). Thank you also to Christina, Enrica (2x), Matteo, Raphael, Roger, Li and Tuan for including me in your group and the good time spent in Dublin (MicroTAS 2016). Thank you to Laurent for reviewing this manuscript. And thanks to Matthieu and Georges, for being nice persons and good friends.

I'm also lucky to have a mother who always showed interest in my work and a father who always challenged me with the good questions, thank you for that, thank you for your support. My brother, on his side, always helped me to clear my mind by talking (a lot) about aviation, thank you for these moments.

Most importantly I wish to thank my beautiful wife, Sophie, who has always been supportive and proud of me. Thank you for making my life better.

*Lausanne, April 2017*

# Abstract

Neurological disorders have a strong negative impact on the quality of life of affected patients, their close relatives as well as on the health economic system. Early diagnosis associated with better treatment outcomes remain difficult to reach. Similarly, misdiagnosis is frequent and can lead to the delivery of the wrong treatment to the patient. As a matter of fact, the therapeutic strategies developed to treat Alzheimer's Disease (AD) and Parkinson's Disease (PD), two major neurodegenerative diseases, are unfortunately only effective for reducing the symptoms. This illustrates the lack of complete understanding of the mechanisms underlining neurodegeneration. In this context, this thesis aims to contribute to a precise comprehension of the synaptic transmission, at the cellular level, by providing a biocompatible brain interface capable of collecting neurochemicals while establishing a tight electrical connection with the cerebral tissues.

The first part of this thesis deals with the design and microfabrication of a novel neural probe which includes microelectrodes and a micro-scale droplet generator for the efficient collection of extracellular fluid. The design choices and the microfabrication approach are detailed while the behavior of the device is assessed using fluidic modeling. Experimental results regarding the neural probe's mechanical strength, electrical and fluidic functions are then presented. In particular, the electrode-tissue interface is assessed using impedance spectroscopy. The probe fluidic function and its ability to perform high frequency (6 Hz) droplet segmented collection in a rapidly changing environment is experimentally demonstrated.

In a second phase is reported the successful *in vivo* testing of the neural probe in the framework of a pilot animal trial performed on rats. A custom microfabricated analysis platform enabling to efficiently detect the content of the collected brain-

---

fluid samples is presented as well. In particular a microfabricated target plate for the distribution and handling of the segmented samples during analysis is reported. This unique approach allows to maintain the temporal history of the flow-segmented samples. Combined with Inductively Coupled (ICP)-Mass Spectrometry (MS), the detection results show the presence in significant quantity of Na, Mg, K and Ca, reflecting the neurochemical state of the brain over time. Quantitative measurements are demonstrated, highlighting the power of this approach.

Simultaneous cerebral tissues electrical modulation and neurochemical recording during periods of 15 min is demonstrated in a third phase. A significant neurochemical response is detected in correlation with the electrical stimulation periods (2 x 1 min). In particular, the extracellular  $K^+$  ion concentration appears to rise during these periods which is further confirmed on each of the 3 implanted subjects. It is stated that the electrical stimulation delivered to the tissues set the neurons in a permanent hyperpolarized state, forcing a strong  $K^+$  ions efflux towards the extracellular space.

This work sets a basis for the development of novel approaches in the detection of malfunction in synaptic transmission. Future perspectives of this technology include new methods enabling earlier diagnosis of neurodegenerative diseases and more efficient treatments based on a closed-loop adjustment of electrical stimulation.

**Key words:** Neurotechnology, brain interface, neural probe, neuromodulation, electrical stimulation, neurochemicals, microchannel, microelectrode, droplet, segmented flow, mass spectrometry.

# Résumé

Les maladies neurodégénératives ont un fort impact sur la qualité de vie des patients affectés, sur leurs proches ainsi que sur le système économique de la santé. Leur diagnostic précoce, associé à des traitements plus efficaces, restent un défi. Les cas de diagnostics erronés sont fréquents, entraînant parfois l'administration du mauvais traitement aux patients. Par ailleurs, les stratégies thérapeutiques développées pour traiter les maladies neurodégénératives sont souvent symptomatiques et non thérapeutiques ce qui démontre que notre compréhension des mécanismes de neurodégénérescence est incomplète. Dans ce contexte, cette thèse vise à contribuer au décodage précis de la transmission synaptique au niveau cellulaire en développant une interface avec le cerveau biocompatible et capable de mesurer des signaux neurochimiques dans les tissus tout en stimulant électriquement ceux-ci.

La première partie de cette thèse traite de la conception et de la fabrication d'une nouvelle sonde neuronale incluant des microélectrodes et un système de collection du fluide extracellulaire par flux segmenté. Les choix de conception ainsi que les étapes de microfabrication y sont détaillés tandis que le comportement du système est prédit à l'aide d'un modèle microfluidique. Une caractérisation du fonctionnement de la sonde est ensuite présentée. En particulier, l'interface électrode-tissu est évaluée par spectroscopie d'impédance. La fonction fluidique de la sonde et sa capacité à effectuer une collection segmentée à haute fréquence (6 Hz) dans un environnement évoluant rapidement sont démontrées.

Dans un deuxième temps, la sonde neuronale est testée *in vivo* en l'implantant dans le cerveau de rats, dans la région du striatum. Une plateforme permettant l'analyse du contenu des échantillons collectés est également présentée. Notamment, un support microfabriqué dédié à la distribution et la manipulation des

---

échantillons et leur analyse est décrit. Cette approche unique permet de maintenir et reconstruire l'historique temporel du prélèvement de fluide extracellulaire par flux segmenté. Les résultats, obtenus grâce à une analyse par spectrométrie de masse à plasma à couplage inductif (ICP-MS), ont montré la présence significative de Na, Mg, K et Ca reflétant l'état neurochimique du cerveau au cours du temps. Les résultats ont également put fournir des valeurs fiables de concentration de certains métaux présents dans le liquide extracellulaire démontrant la puissance de cette approche.

Finalement, la modulation électrique des tissus cérébraux et l'enregistrement neurochimique simultanément pendant des périodes de 15 min sont démontrés. Une réponse neurochimique significative a été détectée en corrélation avec les périodes de stimulation électrique. Par exemple, la concentration d'ions extracellulaires  $K^+$  augmente pendant ces périodes (confirmé sur 3 sujets implantés). La stimulation électrique délivrée semble placer les neurones dans un état d'hyperpolarisation permanente, forçant un efflux des ions  $K^+$  des neurones vers l'espace extracellulaire.

Ce travail constitue une base solide pour le développement d'approches novatrices dans la détection de dysfonctionnement des transmissions synaptiques. Les perspectives futures de cette technologie comprennent de nouvelles méthodes permettant un diagnostic plus précoce de maladies neurodégénératives et des traitements plus efficaces basés sur un ajustement en boucle fermée de stimulation électrique du système nerveux.

**Mots clefs :** Neurotechnologie, interface cérébral, sonde neuronale, neuromodulation, stimulation électrique, neurochimique, microcanaux, microélectrode, goutte, flux segmenté, spectrométrie de masse.

# Contents

<b>Acknowledgements</b>	<b>i</b>
<b>Abstract</b>	<b>iii</b>
<b>Résumé</b>	<b>v</b>
<b>List of Figures</b>	<b>xi</b>
<b>List of Tables</b>	<b>xv</b>
<b>Glossary</b>	<b>xvii</b>
<b>1 Introduction</b>	<b>1</b>
1.1 Scope of the Thesis . . . . .	2
1.2 Context . . . . .	3
1.2.1 Microtechnology . . . . .	3
1.2.2 Clinical Neuroscience . . . . .	6
1.2.3 Motivations . . . . .	12
1.3 State of the Art . . . . .	13
1.3.1 Neural Interfaces . . . . .	14
1.3.2 Neurochemicals Monitoring . . . . .	18
1.4 Thesis Positioning . . . . .	19
1.4.1 Thesis Objectives . . . . .	19
1.4.2 Thesis Structure . . . . .	21
<b>2 Neural Probe - Design and Development</b>	<b>23</b>
2.1 Design Considerations . . . . .	23

## Contents

---

2.1.1	System Requirements . . . . .	23
2.1.2	Microfluidics - Theoretical Basis . . . . .	26
2.1.3	Microelectrode - Theoretical Basis . . . . .	31
2.2	Neural Probe - Geometry and Functions . . . . .	39
2.3	Microfabrication . . . . .	41
2.4	Neural Probe - Features . . . . .	44
2.5	Neural Probe - Microfluidic Model . . . . .	46
2.6	Conclusions . . . . .	52
<b>3</b>	<b>Neural Probe - Functional Validation</b>	<b>53</b>
3.1	Introduction . . . . .	53
3.2	Mechanical Characterization . . . . .	53
3.2.1	Penetration Test . . . . .	53
3.3	Electrical Characterization . . . . .	56
3.3.1	Impedance Spectroscopy . . . . .	56
3.4	Fluidic Characterization . . . . .	59
3.4.1	Droplet Generation - Demonstration . . . . .	59
3.4.2	High Frequency Droplet Sampling . . . . .	60
3.5	Discussion . . . . .	64
3.6	Conclusions . . . . .	66
<b>4</b>	<b><i>In Vivo</i> Neurochemical Sampling</b>	<b>69</b>
4.1	Introduction - Droplet Detection Methods . . . . .	69
4.2	Materials and Methods . . . . .	73
4.2.1	Probe . . . . .	73
4.2.2	Interface Unit . . . . .	75
4.2.3	<i>In Vivo</i> Experiments . . . . .	75
4.2.4	Analysis Method . . . . .	76
4.3	Results . . . . .	80
4.3.1	Acute Neurochemicals Sampling . . . . .	80
4.3.2	Analysis of <i>In Vivo</i> Collected Samples . . . . .	81
4.3.3	Discussion . . . . .	86
4.4	Conclusions . . . . .	88



<b>5</b>	<b>Neurochemicals Recording During Electrical Stimulation of Cerebral Tissues</b>	<b>91</b>
5.1	Introduction . . . . .	91
5.2	Modeling . . . . .	92
5.2.1	Droplet Evaporation Model . . . . .	92
5.2.2	<i>In Vivo</i> Species Diffusion Model . . . . .	98
5.3	Simultaneous Neurochemicals Sampling and Electrical Stimulation	105
5.3.1	Material and Methods . . . . .	105
5.3.2	Results . . . . .	108
5.4	Discussion . . . . .	112
5.5	Conclusions . . . . .	114
<b>6</b>	<b>Conclusions and Future Perspectives</b>	<b>117</b>
6.1	Outlooks . . . . .	121
<b>A</b>	<b>Appendix</b>	<b>141</b>
A.1	Probe Electrical Pairing Chart . . . . .	141
A.2	Electrical Stimulation Pattern . . . . .	142
	<b>List of Publications</b>	<b>143</b>
	<b>Curriculum Vitae</b>	<b>145</b>



# List of Figures

1.1	Multielectrode arrays (MEA) . . . . .	6
1.2	Cerebral microdialysis probe used in clinical settings . . . . .	10
1.3	Signal transmission between neurons . . . . .	14
1.4	Technological evolution of the electrical neural interfaces . . . . .	16
2.1	Poiseuille flow between two planes of infinite dimensions . . . . .	28
2.2	Taylor dispersion in a steady Poiseuille flow . . . . .	29
2.3	Methods for generating a segmented flow . . . . .	30
2.4	Tissue-electrode interface - modeling and typical impedance spectrum . . . . .	34
2.5	Current and potential lines from a microelectrode towards the tissues	37
2.6	Block diagram of the neural probe system . . . . .	39
2.7	Neural probe dimensions and functions . . . . .	40
2.8	Three-dimensional sketch of the neural probe active area (distal tip)	41
2.9	Microfabrication process of the neural probe . . . . .	42
2.10	Scanning electron micrography of the neural probe at intermediate step of the fabrication process . . . . .	43
2.11	Process improvement for preventing rupture of the probe metal tracks . . . . .	43
2.12	Neural probe after microfabrication . . . . .	45
2.13	Scanning electron micrography of the microchannels and the microelectrodes . . . . .	46
2.14	Probe microfluidic network . . . . .	46
2.15	Probe microfluidic equivalent model . . . . .	48
2.16	Model-based prediction of the neural probe microfluidic behaviour	50

## List of Figures

---

2.17 Qualitative plot of the pressure variation along a microchannel filled with aqueous droplets in oil . . . . .	51
3.1 Neural probe bending properties . . . . .	54
3.2 Neural probe penetration test - setup description . . . . .	55
3.3 Neural probe penetration test outcomes . . . . .	56
3.4 Impedance magnitude and phase of the microelectrodes included at the distal tip of the neural probe . . . . .	58
3.5 Fluidic connection at the probe proximal inlet/outlet . . . . .	59
3.6 Experimental setup for the testing of the droplet generation process	61
3.7 Sequence of a droplet generation process occurring within the probe distal tip . . . . .	62
3.8 Demonstration of the neural probe high frequency droplet collection process . . . . .	63
4.1 System description of the neural probe brain-fluid samples collection	74
4.2 Droplet distribution procedure prior to samples analysis . . . . .	78
4.3 <i>In vivo</i> surgery setup and probe track in the tissue post implantation	81
4.4 Sample analysis results . . . . .	82
4.5 Details of the resolution provided by the analysis of the dried spot samples . . . . .	83
4.6 Temporal evolution of the concentration found in brain-fluid samples	84
5.1 Sessile droplet evaporation modes . . . . .	93
5.2 Droplet drying process and associated evaporation mode of a brain-fluid sample . . . . .	94
5.3 Droplet evaporation model outcomes . . . . .	96
5.4 Image sequence of a water droplet during evaporation on a parylene substrate . . . . .	97
5.5 Model description of species diffusion from the cerebral tissues to the neural probe inlet . . . . .	100
5.6 <i>In vivo</i> species diffusion model outcomes . . . . .	104
5.7 Neural probe including the electrical and fluidic connectors . . . .	106
5.8 Relative abundance of Na, Mg and K found in the brain-fluid samples	109

5.9	High resolution 3-dimensional plot of the relative abundance of Mg in a selected dried spot . . . . .	110
5.10	Neurochemical response to electrical stimulation . . . . .	111
A.1	Probe electrical pairing chart . . . . .	141
A.2	Electrical stimulation pulses . . . . .	142



# List of Tables

2.1	Set of basic requirements defined for the development of the neural probe. . . . .	25
2.2	Maximum charge delivery capacity $Q_{CDC}$ for several electrode materials (Stieglitz 2004) . . . . .	38
4.1	Mean Fe, Cu and Zn concentration found in 3 the brain-fluid samples	86
5.1	Dried spot model parameters . . . . .	95
5.2	<i>In vivo</i> diffusion model parameters . . . . .	101
5.3	<i>In vivo</i> diffusion model outcomes . . . . .	101





# Glossary

<b>5-HT</b>	Serotonine
<b>AA</b>	Ascorbic Acid
<b>AD</b>	Alzheimer's Disease
<b>AP</b>	Action Potential
<b>BBB</b>	Blood Brain Barrier
<b>CCA</b>	Constant Contact Angle
<b>CE</b>	Capillary Electrophoresis
<b>CJD</b>	Creutzfeldt-Jakob Disease
<b>CNS</b>	Central Nervous System
<b>CPE</b>	Constant Phase Element
<b>CSF</b>	Cerebrospinal Fluid
<b>CT</b>	Computed Tomography
<b>CWA</b>	Constant Wetting Area
<b>Da</b>	Dopamine
<b>DBS</b>	Deep Brain Stimulation
<b>DC</b>	Direct Current
<b>DNA</b>	Desoxyribonucleic Acid
<b>DRIE</b>	Deep-Reactive Ion Etching
<b>ECF</b>	Extracellular fluid
<b>EEG</b>	Electroencephalography
<b>EMG</b>	Electromyography
<b>ESI</b>	Electrospray Ionisation
<b>ET</b>	Essential Tremors
<b>FND</b>	Functional Neurological Disease
<b>FSCV</b>	Fast Scan Cyclic Voltametry

## Glossary

---

<b>GPI</b>	Globus Pallidus
<b>HD</b>	Huntington's Disease
<b>HPLC</b>	High-Pressure Liquid Chromatography
<b>ICP</b>	Inductively Coupled
<b>IPG</b>	Implantable Pulse Generator
<b>LIF</b>	Laser Induced Fluorescence
<b>LOC</b>	Lab On Chip
<b>LOD</b>	Limit of Detection
<b>MALDI</b>	Matrix Assisted Laser Desorption/Ionisation
<b>MEA</b>	Multielectrode Arrays
<b>MEMS</b>	Microelectromechanical Systems
<b>MRI</b>	Magnetic Resonance Imaging
<b>MS</b>	Mass Spectrometry
<b>MScI</b>	Multiple Sclerosis
<b>NCS</b>	Nerve Conduction Study
<b>PCR</b>	Polymerase Chain Reaction
<b>PD</b>	Parkinson's Disease
<b>PDMS</b>	Polydimethylsiloxane
<b>PEDOT</b>	3,4-Ethylenedioxythiophene
<b>PFD</b>	Perfluoromethyldecalin
<b>PI</b>	Polyimide
<b>PNS</b>	Peripheral Nervous System
<b>PRF</b>	Peak Resistance Frequency
<b>PRS</b>	Product Requirements Specifications
<b>Re</b>	Reynolds Number
<b>SAH</b>	Subarachnoid Hemorrhages
<b>SEM</b>	Scanning Electron Micrography
<b>STN</b>	Subthalamic Nucleus
<b>URS</b>	User Requirements Specifications

# Chapter 1

## Introduction

Neuroscience is a fascinating field which aims at providing insights into the most complex organ of the human body; the brain. The brain is considered as a great biological machine which is able to sense, react, organize, store, regulate and create while it extensively contributes to what we collectively call consciousness. Although numerous efforts have been made to understand, decode and predict the mechanisms taking place in the Central Nervous System (CNS) and Peripheral Nervous System (PNS), it still remains poorly understood. Indeed the human cerebral cortex is a complex multi-level structure containing in average 86 billions neurons each connected to a few thousands of other neurons according to the latest evaluation (Azevedo et al. 2009). They communicate together and constitute a centralized control center which exert orders on the other organs of the human body. The brain is responsible for the proper working of major conscious functions (such as perception, motor control and learning) as well as unconscious ones (such as breathing, cardiac or digestive regulation). Sometimes these functions are unfortunately dis-regulated due to a progressive loss of structure or function in the neuronal network, including neuronal death. Neurodegenerative diseases such as AD, PD and Huntington's Disease (HD) are caused by such degeneration processes. These pathologies strongly affect the direct human environment of affected patients and largely impact the society. In this context, a thorough understanding of the mechanisms involved at the

## Chapter 1. Introduction

---

cellular level can contribute to provide a better understanding of the mechanisms causing the diseases and carries the hope to develop effective treatments against it. Several approaches can effectively address this need and, among all of them, neurotechnologies is a very promising one.

Neurotechnology can be defined as any technology which has a fundamental influence on how we understand the CNS or PNS functions and activities. It also includes technologies having a repair or improvement function of the brain. The development of effective medical treatments such as Deep Brain Stimulation (DBS) which treats Parkinson's disease symptoms is a famous example. The therapy consists in implanting in the cerebral tissues a neural probe comprising platinum (Pt) electrodes which constantly stimulate electrically a precise cerebral region, the Subthalamic Nucleus (STN). DBS is an alternative to drug-based treatments and is considered as an effective therapy with more than 120'000 patients implanted in the world (Fukaya et al. 2015). Cochlear implant is another successful application of neurotechnologies. The therapy consists in the direct electrical stimulation of the acoustic nerve in order to restore a sense of sound to persons affected by profound or total hearing impairment. The therapy is universally considered as a success and has been implemented in more than 320'000 patients worldwide (Gaylor et al. 2013). These two examples perfectly illustrate the effectiveness of neurotechnologies in providing novel therapies by a controlled interaction with the CNS and PNS.

### 1.1 Scope of the Thesis

Among many other features such as their biocompatibility, hermeticity and reduced dimensions, a very important requirement for cochlear and DBS implants is their ability to efficiently communicate with the nerve cells. This highlights the importance of understanding the inter-neuron signal transmissions taking place in the cerebral tissues to deliver an efficient therapy. At this level, the signal transmission is regulated and driven by two distinct phenomena; electrical and chemical impulses. The scope of this thesis is precisely to focus on the neuronal

cells inter-communications. In this context, we take advantage of the wide range of possibilities offered by the microtechnologies for producing efficient brain interfaces while remaining compatible with the size-scale of a neuronal cell ( $5\mu\text{m}$  to  $100\mu\text{m}$ ). A focus along the course of this work was to consider biocompatibility as an essential requirement. Indeed limiting tissue reactions and minimizing inflammation result in better device integration in implanted tissues. In particular this guarantees to measure the expected biological effect when the experiment involves *in vivo* testing in living animals. More generally, this thesis lies at the interface between neurotechnology, biology and microtechnology.

## 1.2 Context

### 1.2.1 Microtechnology

Microtechnology is a field which deals with systems in a size range near to the micrometer ( $1\mu\text{m} = 1 \times 10^{-6}\text{ m}$ ). Originally the field is born in the 1960s when progresses performed by the semi-conductor industry allowed to propose the first transistors (Texas Instruments) and the integrated circuits (Kilby 1959). Not only these inventions revolutionized the electronic industry, but the associated manufacturing processes allowed to improve the electronic components performances, functionalities and reliability while reducing fabrication costs and allowing a scale up of the production volumes (Kilby 1976). These progresses also largely impacted the computers which could suddenly be reduced from a large volume machine taking the space of a room to a compact portable system. Electronics was certainly the first domain to take advantage of the progresses realized in microtechnology, however, almost in parallel to these evolutions, miniaturization of mechanical components gave rise to Microelectromechanical Systems (MEMS).

## Chapter 1. Introduction

---

### 1.2.1.1 MEMS

A MEMS usually consists in an electrical system combined with actionable mechanical components that interact with their environment. The huge potential of these very small machines was foreseen in the famous lecture of R. Feynman "There is plenty of room in the bottom" (Feynman 1960). MEMS employ the same fabrication processes (lithography, film deposition, etching, etc) as developed for the silicon-based semiconductor industry. A major advantage therefore lies in the possibility to integrate micromechanical parts on the same platform than the associated microelectrical components as part of a unique production process. The discovery and characterization of piezoresistive materials (silicon and germanium) in the late 1950s contributed to the development of MEMS (Smith 1954; W. Paul et al. 1955). Early in the 1960s, the Bell labs and Honeywell made significant progresses and published different studies about thin piezoresistive silicon diaphragms which constituted the first pressure sensors and strain gauges, an early version of MEMS (Pfann et al. 1961; Tufte et al. 1962). Following these developments, many different sensors were developed. For instance, the accelerometer measuring vibrations, shocks and motion has been offered in a variation of applications ranging from the shock detector for airbag deployment to personal monitoring systems (e.g. wrist band) which measures the quality of sleep based on the body motions during night (Ciuti et al. 2015). Other examples of MEMS detectors include gyroscopes (position and rotation sensor) and thermal mass flow sensor (Bogue 2013). Nowadays, these systems are produced at ultra high volume and very low cost for consumers electronics. We certainly can claim that towards 2020 more than 2 over 3 persons in the world will carry MEMS in their pockets since a recent study confirmed the smartphone industry market penetration to reach 70% of the world population (Carson et al. 2015).

### 1.2.1.2 Microfluidics

Microfluidics, a major branch of microtechnology, deals with the precise control and handling of fluids. In microfluidic systems, fluids are constrained in sub-millimetre scale channels and driven by capillary forces or external pumps.

Typically, the functions of such microdevices includes the displacement, the mixing, the separation and other fluidic processes. Early applications of this technology emerged at the end of the 1970s with the development of silicon inkjet printer nozzles (Bassous et al. 1977). With the growing interest of the scientific community for the micromanipulation of fluids, micropumps and valves made their apparition (Van de Pol et al. 1989). Soon the chemical processes usually carried out in the laboratory were attempted to be miniaturized and performed in a single chip platform. While the miniaturization of the fluid and reagent volume would usually not impact the molecular reactions, laws of scale for molecular diffusion and heat transport enabled a dramatic increase in reaction efficiency and throughput (Dittrich et al. 2006). These so called "Lab On Chip (LOC)" systems started to represent a significant technological growth at the beginning of the 1990s when they turned out to become interesting for genomics. For instance Desoxyribonucleic Acid (DNA) microarrays used to measure the expression of a large number of genes are considered as an advanced LOC device providing new opportunities for DNA diagnostics (J. Wang 2000). Nowadays microfluidics and LOC devices developments are largely oriented towards the field of "point of care" diagnostic devices (Jung et al. 2015). These devices aims at providing *in vitro* diagnostics at the site the care is given, including at home, and address the growing need of rapid treatment associated with rapid diagnosis. Interestingly, LOC have been applied to a large range of neurobiology studies such as biochemical experimentation, morphological observations or electrophysiological investigation (Soe et al. 2012). In particular, advances realized in microfabrication processes enabled to produce Multielectrode Arrays (MEA) which are devices containing multiple electrodes organized in a planar configuration to measure *in vitro* neuronal signals. The study involving neural interfaces brought significant understanding to the electrophysiological processes taking place at the neuronal network level. The application of this technology includes electrical recording and stimulation of neuronal cells as well as drug testing and screening. Figure 1.1 (a) shows a Scanning Electron Micrography (SEM) of a neuron adhering to pillar electrodes of a MEA whereas figure 1.1 (b) presents a general view of a 64 x 64 microelectrode array device proposed by Berdondini *et al.* (Zeck et al. 2001; Berdondini et al. 2009). In the future, LOC is anticipated to become a

## Chapter 1. Introduction

---

new paradigm of instrumentation and will probably be included in the toolbox of the neuro-clinicians in order to support their decisions throughout the diagnosis phase.

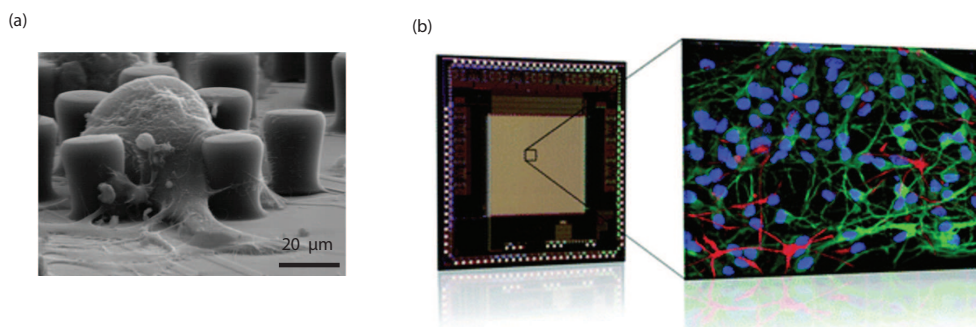


**Figure 1.1** (a) SEM view of a neuron adhering to a set of pillar electrodes part of a MEA (b) General architecture of a MEA device. The gold-colored area is structured with a 64 x 64 planar electrode array which are used to sense and stimulate a neuronal network (adapted from Zeck et al. 2001; Berdondini et al. 2009)

### 1.2.2 Clinical Neuroscience

Clinical neuroscience is a branch of medicine which deals with various types of neurological disorders. It is subdivided in 3 specialities; neurosurgery, psychiatry and neurology. While neurosurgery focuses on the surgical treatment of cerebral diseases and psychiatry is devoted to the diagnosis and treatment of mental disorders, neurology takes care of the CNS and PNS disorders. For a physician trained in neurology the clinical evaluation of a patient often starts with an examination during which the assessment of the cognitive functions, motor reflexes and status of cranial nerves and reflexes is performed. Different diagnostic methods exist to support the initial diagnostic. We distinguish imaging methods like Computed Tomography (CT) scan, Magnetic Resonance Imaging (MRI) or ultrasounds and neurophysiology methods such as Electroencephalography (EEG), Electromyography (EMG), Nerve Conduction Study (NCS), evoked potentials or lumbar puncture. All these methods largely rely on advanced technologies facilitating the clinicians decision process whether it be during the diagnostic phase or during surgeries.



### 1.2.2.1 Neuroimaging

Neuroimaging is a relatively recent discipline in medicine which has been developed with the aim to image the inner composition of the brain at a structural and functional level (Filler 2009). It usually follows a neurological examination made by a physician to further investigate a patient who may present a neurological disorder. For instance CT is a method in which multiple x-ray scans are taken in a same plane while successively rotating the source and detector around the patient. After image reconstruction it enables to build a virtual tissue slice of the body, allowing the physician to literally see "inside" the patient. CT may be indicated for the detection of traumatic brain injuries and in case of headaches (B. Lee et al. 2005; Evans 2009). A limitation to this technique may be related to the hazard represented by the x-ray radiations, although this issue is well controlled today.

MRI produces high resolution images using strong electro-magnetic fields to generate an image of the body inner anatomy without using x-rays. Its superior resolution and better contrast between white and grey matter makes it the method of choice for brain imaging and largely participates to the detection of various cerebral conditions such as epilepsy, dementia or cerebrovascular diseases (Jordan et al. 2014).

Ultrasonology, a technique in which sound waves reflected by the inner structures of the body are measured and computed to produce an image is the method of choice to monitor cerebrovascular and hemodynamic parameters of the brain. The principal advantage of this method is its low cost and high temporal resolution although it lacks resolution for the detection of soft tissues (Tzivgoulis et al. 2016).

### 1.2.2.2 Clinical Neurophysiology

While neuroimaging methods provide a representation of the brain through detailed images, sometimes the physician needs to focus more deeply on a specific CNS or PNS function. Clinical neurophysiology concentrates on the recording

## Chapter 1. Introduction

---

of bioelectrical activity of the nervous tissues whether evoked or spontaneous. It can reveal specific and precise information about the site and the extent of a lesion or dysfunction in the nervous tissues. Among the available methods, EEG is a non invasive procedure in which multiple electrodes placed on the scalp of a patient measure voltage fluctuations resulting from ionic currents in the upper level neurons of the brain (cortex). It reflects the spontaneous activity of these structures over time with excellent temporal resolution. EEG is used to diagnose epilepsy and help to locate the seizure origin and propagation pattern (Michel et al. 2012).

EMG is a method which evaluates and records the electrical activity produced by the muscles activated by neuro-electrical impulses. This approach is often indicated when the physician needs to detect abnormalities in the activation level that are linked to a neuromuscular disease or to motor control disorders. EMG is also used in motor prosthetic limb systems in order to actuate and control the robotic device. EMG is usually performed in combination with NCS to measure the nerve conductivity. NCS is a procedure which evaluates the conduction velocity in motor and sensory nerves of the human body. It is minimally invasive since the approach involves transdermal stimulation using electrodes placed on the patient skin while conduction needles are also used for direct *in vivo* nerve stimulation. NCS along with EMG are indicated when there is pain in a limb, weaknesses due to spinal nerve compression and for the detection of some other neurological disorders (Chichkova et al. 2010).

Evoked potentials is another method where electrical potentials are recorded from nervous structures following the voluntary stimulus of a sense organ. Visual, auditory and tactile stimuli are voluntarily presented to the patient in order to elicit a CNS response. The reversed process consisting in stimulating the nervous tissues and controlling the intended effect on a patient is practiced as well. It is extremely useful when intraoperative neurophysiological monitoring is required. Indeed certain crucial neural structures (spinal cord, white matter, etc.) which need to be preserved are recorded during surgeries in order to guide the neurosurgeons action (e.g tumor resection). This aims at extending as much as possible the surgical treatment while limiting the risk of future neurological

deficits. The impact of such methods is high; it has permitted to significantly reduce the morbidity and improve the quality of life of patients treated for glioma tumors (resective surgeries) (De Witt Hamer et al. 2012; Duffau et al. 2005).

As exposed in this chapter, clinical neuroscience largely makes use of different imaging and bioelectric measurement methods to diagnose and treat affected patients. The brain biochemistry accompanying cerebral disorders or injuries can provide equally important physiological information to the clinicians during diagnostic and post-treatment. Lumbar puncture is a complementary diagnostic tool which consists in the collection of Cerebrospinal Fluid (CSF) with a needle inserted into the spinal cord canal accessed from the back of the patient. The analysis of the collected liquid gives precious information regarding the diagnosed disease. The advantage of such an approach is that it is a relatively simple medical procedure whereas the analysis results may, for instance, exclude infections, inflammatory and neoplastic disease affecting the CNS (Sexton 2011; Shlamovitz 2007).

Similarly to lumbar puncture, cerebral microdialysis involves the sampling and analysis of liquid collected from discrete brain locations. Here the Extracellular fluid (ECF) collection is performed continuously with a microdialysis probe inserted in the brain. A microdialysis probe consists in a catheter in which a continuous perfusate fluid circulation is performed while, at the distal tip, the catheter contains a membrane through which ECF molecules are incorporated in the perfusate to be later analysed. Figure 1.2 shows a market-approved cerebral microdialysis (MD) probe system. The method allows to monitor the cerebral energy metabolism changes over time before being detectable in the peripheral vascular system. The recorded parameters comprise the glucose concentration level as well as the ratio between the lactate and pyruvate metabolites which reflects the mitochondrial state at the cellular level. It is widely used in neurocritical care units to monitor patients after cerebral ischemia (Nordström 2010). A decrease of the glucose level and an increase in the lactate/pyruvate ratio is associated with poor outcomes after Subarachnoid Hemorrhages (SAH) and traumatic brain injuries (Timofeev et al. 2011). Another application of cerebral microdialysis is the determination of the cerebral perfusion pressure optimal level

## Chapter 1. Introduction

after traumatic brain injuries (Nordstrom et al. 2003). Among the limitations of the method we can cite the temporal resolution which is poor (typically of 10 min to 20 min) and makes the method only compatible with the monitoring of slowly occurring neurochemical changes (Bourne 2003).

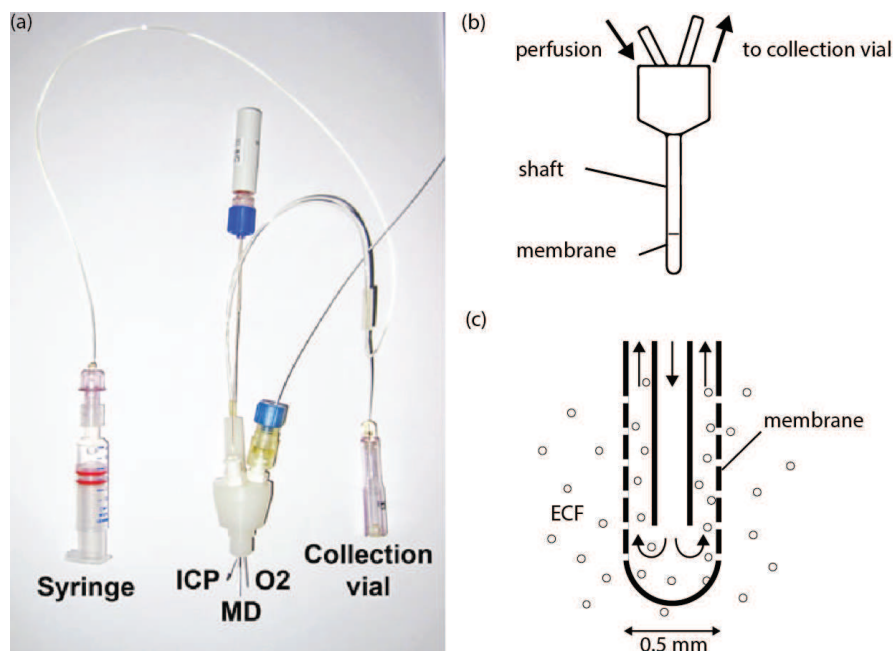


**Figure 1.2** (a) Cerebral microdialysis (MD) probe used in clinical settings. The system also includes an intracranial pressure sensor (ICP) and a brain tissue oxygen sensor (O<sub>2</sub>). A syringe pump delivers the perfusate solution to the probe and the microdialysate is collected from the collection vial. (adapted from R. J. Shannon et al. 2013) (b) Microdialysis probe including the shaft and the distal part of the catheter which contains the membrane. (c) Detail and inner structure of the microdialysis catheter tip when exchanging molecules with the ECF.

### 1.2.2.3 Diagnostics

As it is the case in many medical fields, a successful treatment in neurology is only possible when an accurate diagnostic has been performed and an indication clearly identified. As discussed in chapter 1.2.2.2, the clinical evaluation starts with the patient examination which aims at evaluating the cognitive and motor function. This initial step is often followed by a deeper evaluation using imaging

or neurophysiological methods aiming at confirming the presence of the disorder. However, neurological misdiagnosis can occur; essential tremor, one of the most common neurological disorder, gets often mistaken for PD (in 1 over 3 patient) while epileptic patients experiencing non-convulsive seizures might be misdiagnosed for primary psychiatric illnesses (Jain et al. 2006; Mirsattari et al. 2011). A retrospective study performed on more than 1100 subjects diagnosed and treated for the Creutzfeldt-Jakob Disease (CJD) indicated that 32% of them were, in fact, negative to prion disease (Chitravas et al. 2011). Identically, Multiple Sclerosis (MScl) is a CNS disease reported to be commonly misdiagnosed in 10 to 15% of cases, some studies even talking about 35% (group of 366 patients) (Poser 1997; Solomon et al. 2013). In MScl, the radiographic analysis and over-reliance on MRI interpretation is a common contemporary mistake leading to misdiagnosis (Solomon et al. 2013). In Functional Neurological Disease (FND) like in MScl, the diagnosis is difficult to establish since we lack understanding in the pathophysiological mechanism involved. FND patients present normal brain structure although they experience strong symptoms such as blackouts, weaknesses, movement disorders and sensory symptoms (Stone et al. 2010).

These various examples demonstrate that neurological disorders might be difficult to identify resulting in undiagnosis or misdiagnosis. Consequences can be serious as affected patients may not receive the adequate medication and appropriate treatment. This highlights the need for better understanding and characterizing the disorder development and propagation mechanisms. Novel tools and methods are required in order to achieve this goal.

It is commonly known that neurodegenerative diseases begins 10 to 20 years prior to clinical manifestation and diagnosis (Sheinerman et al. 2013; Hampel et al. 2011). Although the molecular mechanisms behind the pathologies are diverse, neurodegenerative diseases present common processes such as retraction of neurites, dysfunction and destruction of synapses and ultimately neuronal death (Bredesen 2009). It is for instance the case in AD and PD. AD is an irreversible neurodegenerative disease characterized by a progressive evolution causing memory losses at the beginning, language problems, disorientation and loss of motivation in severe manifestations. Recent studies reports that 6% of

## Chapter 1. Introduction

---

persons aged over 65 are affected in the US which has a huge economical impact on the health system (Reitz et al. 2014). In PD, the second most common neurological disorder (after AD), the symptoms usually include motor and non-motor dysfunctions such as rest tremor, bradykinesia, rigidity and loss of postural reflexes with serious consequences on the quality of life of affected individuals (Jankovic 2008; Wu et al. 2011). Both conditions (AD and PD) are most often diagnosed late after the onset of the disease. In PD striatal dopamine content is already reduced by 80% or more when clinical signs of the condition may be identified (Marsden 1990). In AD, diagnosis may be delayed because the symptoms appear often at a moment when the patient family and close environment may interpret the symptoms as being normal given the age of the person (Miranda et al. 2011).

Today available medications are rather slowing down the progression course of the neurological disorders than having a curing effect. However these treatments, especially for PD and MScl, are more effective when started earlier, in the mild phase, and result in a prolonged quality of life for the affected patients (Noyes et al. 2013; Pahwa et al. 2010; Hauser 2009). Ultimately, the physicians would like to identify asymptomatic individuals at risk for developing the disease (Petersen 2009). This shows there is a need for detection methods enabling earlier diagnosis of neurological disorders. Early detection will probably be only possible when associated with a better understanding of the pathophysiological mechanisms behind the disorders.

### 1.2.3 Motivations

The high occurrence of misdiagnosis cases in the detection of neurological disorders demonstrate that their manifestation translates in subtle symptoms which are difficult to identify. Although many progresses have been made to decode the pathophysiological mechanisms involved in AD and PD, two major degenerative diseases, we today still lack a complete understanding of the degenerative phenomena involved. The neuroscientists need better tools than existing neurophysiological solutions which will eventually translate in a new detection method

or therapy in the future. Providing a precise comprehension of the synaptic transmission, at the cellular level, implies to understand how the neurochemically mediated connections between neurons function and how they are affected by the neurodegenerative action. As stated by DeKosky *et al.*, this could allow to address 2 major unmet needs; the identification of effective medication for the treatment of neurological disorders and the earlier initiation of the treatment (DeKosky *et al.* 2003). The objective of this work is to develop novel methods for performing advanced neurophysiological studies in the brain. The use of microtechnology methods will enable to provide minimal invasive solutions by reducing the size of the device.

## 1.3 State of the Art

### 1.3.0.1 Synaptic Transmission

The human brain is composed of 86 billions neurons forming a great network capable of processing complex informations (Azevedo *et al.* 2009). A neuron is basically composed of a soma containing the nucleus prolonged by dendrites and an axon terminated by synapses. This specific cell is electrically excitable and capable of propagating Action Potential (AP) to other neurons via its axon and synapse while its dendrites serve to bring signals received by neighbouring neurons. Transmission of information in the brain is driven by electrochemical processes. When a neuron propagates an AP that ends-up in the synapse it stimulates the release of chemical agents in the synaptic cleft, the neurotransmitters. These neurotransmitters travel to the post-synaptic neuron and generate (or inhibit) a new action potential as represented in figure 1.3. Besides this rather classical description based on spatially-specific neurochemical exchanges (taking place in the synaptic cleft) neurons may also influence themselves by "volume transmission" consisting in a general change of molecular composition in a given region. The continuation of an AP propagation between two neural cells depends on the temporal and spatial summation of these multiple inputs received by the distal neuron. As the generation and propagation of AP is due to ionic exchanges



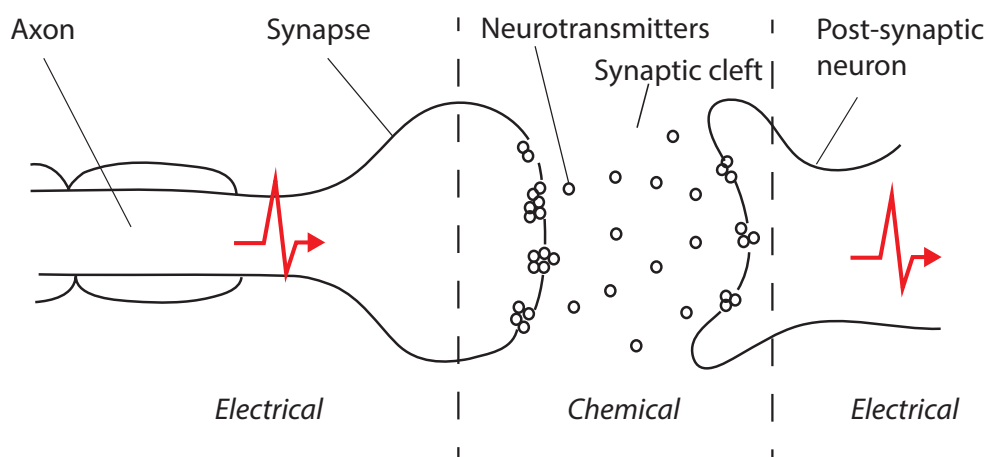


**Figure 1.3** Schematic representation of signal transmission between neurons. The incoming action potential provokes the release of endogenous chemicals, the neurotransmitters, when reaching the synapse. Neurotransmitters diffuse in the synaptic cleft and reach the post synaptic neuron to generate a new action potential. The signal transmission is based both on electrical and chemical processes.

taking place through the neuron membrane, its depolarization has an impact on the external medium ionic composition (Hodgkin and Katz 1949). Therefore, extracellular recordings of the electrical potentials is an efficient strategy for monitoring the intracellular signal propagation.

### 1.3.1 Neural Interfaces

#### 1.3.1.1 Wire Electrodes

As introduced in the precedent chapter the inter-neuron communication is essentially based on electrochemical processes. Due to a relatively straight forward implementation, electrical signal acquisition was the first method explored by the neuroscientists for interfacing neuronal cells. Probably inspired by the work performed by Hodgkin and Huxley in their study about the conduction in nerves, the first *in vivo* devices were constituted of a glass-isolated micro Pt wire (diameter in the  $100\mu\text{m}$  range) of which the conductive distal tip was the recording site (Hodgkin and Huxley 1952; HajjHassan et al. 2008). They were developed in the 1950s and allowed to observe and better understand in real time how a



single neuron functions *in vivo* and how multiple neurons interact with each other (Gesteland et al. 1959). Serial displacements of the wire electrode at the sensorimotor cortex level provided deeper understanding of the brain structure function but quickly the need for larger arrays providing multisite recording capacity appeared. Such systems comprised first several wires assembled together before to be surpassed by the potential of silicon microfabricated multi-site recording arrays (Terzuolo et al. 1961; Verzeano et al. 1960). However a particular class of ultra small wire-electrode consisting of a single carbon fibre (diameter of  $7\mu\text{m}$ ) was soon proposed as an efficient neural recording device (Armstrong-James et al. 1979). As a matter of fact carbon wire electrodes largely contributed to the understanding of the mechanisms involved in inter-neuron communication when they were identified as an electrochemically stable material and proposed to perform Fast Scan Cyclic Voltametry (FSCV) *in vivo* (Millar et al. 1985). In this method, cyclic voltametry is performed in cerebral tissues at very high scan speed (up to  $10^{-6}\text{ V/sec}$ ) and allows to monitor the release of certain neurotransmitters with sub-second precision (Perry et al. 2009). Although the method benefited from a high temporal resolution (reaching 10 Hz) it remained mainly limited to the study of Dopamine (Da) which has a well distinguishable oxidation peak compared to other interfering electroactives species present in brain tissues. Latest technological advancements of micro-wire devices concerns the addition of permeable 3,4-Ethylenedioxythiophene (PEDOT)-Nafion composite membrane or vertically-aligned carbon nanotubes at the conducting tip allowing for selective detection of Da or ascorbate, respectively (Xiang et al. 2014; Vreeland et al. 2015).

#### 1.3.1.2 Silicon-based Devices

The group of Robert L. White from Stanford University pioneered when they proposed to use integrated circuit manufacturing processes to create multielectrode arrays (Mercer et al. 1978). These first devices comprised a molybdenum substrate and Pt metallic conductors as shown in figure 1.4 (a). Soon the base material of these devices became rigid silicon substrate with Pt-deposited electrodes. The technology progressed and the integrated circuit became part of the recording

## Chapter 1. Introduction

---

device itself, allowing to provide a better decoding of the brain functions (Bragin et al. 1995). The Utah array developed by the group of Richard A. Normann provided for the first time a rigid 100 channels probe grid organized in a 3D network (Campbell et al. 1991) as shown in figure 1.4 (b). This tool was proposed as a reliable neural interface to perform recordings and stimulation at the level of the sensorimotor cortex (Maynard et al. 1997). Sophisticated microfabricated

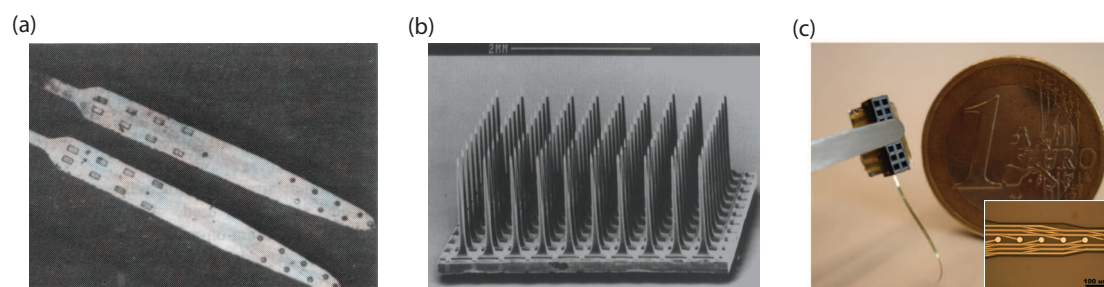


**Figure 1.4** Technological evolution of the electrical neural interfaces. (a) First reported microfabricated molybdenum-platinum neural probes. Each probe carries 8 Pt electrodes. (adapted from Mercer et al. 1978) (b) SEM of the Utah intracortical electrode array. The structure integrates a  $10 \times 10$  electrodes array arranged in a compact manner. A platinum layer is deposited on the 1.2 mm tall tips. (adapted from Maynard et al. 1997). (c) Flexible polymer-based multielectrode array. Polyimide is used as substrate and insulator material for the Pt tracks. (adapted from Mercanzini, Cheung, et al. 2007)

approaches allowed for spatially differentiated analysis by taking advantage of the multi-electrode arrays configuration when used in combination with electrochemical FSCV measurements (Garris et al. 1997; Zachek et al. 2010). Although the method presents an excellent temporal resolution, a limit for FSCV detection is its restricted field of use which remains linked to Da analysis. Interestingly, simultaneous analysis of Da and Serotonin (5-HT) was also demonstrated to be feasible (in a controlled analytical setup, not *in vivo*) despite the usual difficulties to discriminate these species from Ascorbic Acid (AA) (Anastassiou et al. 2006). A recent study proposed a material improvement with boron-doped diamond as electrode for performing FSCV in cerebral tissues (Hébert et al. 2015). This approach would present the advantage to be MRI compatible in the perspective to permanently implant such a structure in the brain.

### 1.3.1.3 Polymer-based Devices

As the applications for *in vivo* neural recording continued to grow, the neurophysiologists started to encounter several limitations with silicon-based devices. Chronic injuries that were caused during implantation, brittle characteristics of silicon and long-term tissue reaction severely impacted their functionality (Williams et al. 1999). As a response to these limitations, a new category of biocompatible polyimide-based devices integrating platinum electrodes were proposed (Metz, Oppliger, et al. 2000; T. Stieglitz et al. 2000; Rousche et al. 2001). A major advantage of these technologies is their mechanical flexibility as illustrated in figure 1.4 (d). A direct application appeared, the nerve cuff electrodes, which allowed to perform neural recordings with a flexible device wrapped around the periphery of a nerve (Rodriguez et al. 2000). Inflammatory tissue reaction in acute and chronic use was showed to be minimized with polyimide-platinum combined devices (Mercanzini, Cheung, et al. 2007; Mercanzini, Colin, et al. 2009). Biocompatible polymer-based neural interfaces have imposed themselves as the material of choice for developing performant long-term implantable electrical interfaces. The latest neural probe technology includes ultra thin, ultra flexible injectable mesh electrodes (Xie et al. 2015). The device re-conciliate the neural probes with the basic requirements for efficient chronic recording in neuronal tissues by providing a very dense network of recording sites and a highly flexible substrate compatible with the mechanical properties of the cerebral tissues.

### 1.3.1.4 Fluidic Devices

In parallel to the evolution of electrical neural probes, as microfabrication methods improved, fluidic microchannels were successfully integrated on electrical neural probes. They constituted a technological "add-on" for the electrical neural probes by providing a fluidic access to the implanted tissues. The main motivation was here to bypass the Blood Brain Barrier (BBB) which is usually a difficult limit to cross for standards drug-based approaches. A first application was therefore to perform drug screening with different chemical agents in the cerebral tissues by monitoring the electrical activity response of the neurons (J. Chen et al. 1997).

More recently, polymer-based probes combining microelectrodes and microfluidic channels on the same device were presented. Altuna *et al.* implanted SU-8 (negative photoresist epoxy) probes in anaesthetized rat brains and demonstrated a high correlation between drug delivery and consecutive increased electrical activity (Altuna, Bellistri, et al. 2013). The stretchable Polydimethylsiloxane (PDMS) device proposed by Minev *et al.* also demonstrated the potential of simultaneous electrical and fluidic stimulation to restore voluntary locomotion in a rat affected by a paralyzing spinal cord injury (Minev et al. 2015).

### 1.3.2 Neurochemicals Monitoring

#### 1.3.2.1 Microdialysis

As emphasized in the last chapter the fluidic function of neural probes remained mainly limited to liquid delivery *in-situ*. An explanation to this restricted field of use could be provided by the existence of another method called microdialysis. Microdialysis probes were developed by neuroscientists for the extraction of brain fluids such as CSF. Their working principle is based on establishing a gradient of concentration between two compartments separated by a semi-permeable membrane to drive a molecular diffusion inside the probe. Their successful operation for quantifying molecule levels in neuronal tissue demonstrated by Ungerstedt *et al.* contributed significantly to the use of this method in neuroscience (Ljungberg et al. 1978; Zetterstrom et al. 1984). These devices were largely used for the monitoring of neuromodulators concentration in cerebral tissues. The role of adenosine in mediating sleep was decoded using microdialysis. It revealed that the adenosine concentration in ECF increases during long-lasting awake periods while it tends to restore during sleep periods (Porkka-Heiskanen et al. 1997). Microdialysis was also used to establish the link existing between the glutamate concentration rise following brain ischemia and its probable toxic effect on cerebral tissues (Benveniste et al. 1984). Although promising applications were developed using microdialysis probes they present some major limitations. The probes are still relatively large with a typical diameter of 200  $\mu\text{m}$  to 400  $\mu\text{m}$  and

a sampling length of 1 mm to 4 mm, thus drastically limiting spatial resolution when recording in cerebral tissues (Kennedy 2013). Furthermore, the temporal resolution achieved with these systems is limited to 10 to 20 minutes which make them incompatible with the time scale of the neurochemical exchanges taking place inbetween neurons (Aris 1956; Kennedy 2013).

### 1.3.2.2 Push-pull Perfusion

Push-pull perfusion is an *in vivo* sampling method consisting in perfusing a fluid in the tissues with a micro cannulae while re-collecting the same fluid with another adjacent cannulae; the perfusate being for a short period of time in direct contact with the ECF tissues. The method was first reported in 1961 by J. Gadhum and used *in vivo* to perform biochemical behavior studies (Tilson et al. 1970). These systems were first operated at high flow rate ( $\sim 50 \mu\text{Lmin}^{-1}$  to  $200 \mu\text{Lmin}^{-1}$ ) resulting in substantial lesions to the brain tissues (Redgrave 1977; Cepeda et al. 2015). Low-flow push-pull perfusion ( $< 50 \text{ nL/min}$ ) was demonstrated to be less invasive than currently available microdialysis options (Cepeda et al. 2015). The first low-flow push-pull perfusion devices introduced consisted in concentrically assembled capillary tubing while, only recently, the group of R.Kennedy proposed a microfabricated push-pull device (Kottegoda et al. 2002; W. H. Lee, Thomas R. Slaney, et al. 2013). The latest evolution of this device consisted in incorporating a nanoporous membrane at the tip of the probe thus turning the system into a microdialysis application and loosing spatial resolution (the sampling zone is 4 mm long) (W. H. Lee, Ngernsutivorakul, et al. 2016).

## 1.4 Thesis Positioning

### 1.4.1 Thesis Objectives

The comprehension of the phenomena involved at the neuronal level implies both a thorough understanding of the electrical and chemical processes involved. The

## Chapter 1. Introduction

---

understanding of the interplay between electrical processes and correlated chemical processes is equally important. Implanted minimally invasive approaches are preferable for the collection of relevant and precise information at the cellular level. As highlighted in the state of the art (1.3), there are today only a few devices combining the features of chemical and electrical interactions. Furthermore, their field of use has been limited to fluidic delivery and simultaneous electrical recording (sometimes stimulation) which is very limiting. Today a method allowing for a reliable electrical interface with the cerebral tissues and a direct access to the brain metabolites overpassing the low spatial and temporal limitations of the microdialysis is missing.

The objective of this thesis is to address this limitation and contribute to the field of electrophysiology by developing new interaction strategies with the cerebral tissues. The implementation of microfabrication methods for the integration of electrical and microfluidic features on the same device will allow to perform precise, time-resolved, neurochemicals collection while remaining in close proximity to the tissues. This work further explores the versatility provided by the MS analysis method for the detection of the molecules extracted from brain-fluid samples.

More generally, such a tool could be a great platform for completing our understanding of the brain functions. It is thought that introducing combined interaction functions (chemical and electrical) could potentially lead to the development of new therapies. Today's existing therapies such as DBS or cochlear stimulation are exclusively based on electrical neuromodulation which is probably limiting the extent of the therapeutic effect. As presented in this chapter, diagnosis of neurological disorders can be challenging with the current methods. This work sets a basis for the development of novel approaches in the detection of malfunctioning synaptic transmission. Future application of the technology could enable earlier diagnosis of neurodegenerative diseases with a probable impact on extending the quality of life of affected patients.

### 1.4.2 Thesis Structure

The first part of this work deals with the design and microfabrication of the neural probe and with the functional testing of the device (chapter 2 and 3). In a second phase is reported the first *in vivo* testing of the probe in the framework of a pilot animal trial performed on rats (chapter 4). The detection method implemented in order to analyze the collected samples is detailed in this section as well. The third part deals with the second *in vivo* trial of the neural probe where neurochemical response to electrical stimulation of cerebral tissues is investigated (chapter 5).





# Chapter 2

## Neural Probe - Design and Development

This chapter addresses the main topics which enabled the design and development of the neural probe. It begins with a list of requirements regarding the functions to be integrated into this device which will further guide its development throughout this work. Then theoretical considerations for microfluidics and microelectrodes design are made before introducing the characteristics and features of the neural probe. Its advanced microfabrication method is described while providing some details regarding process optimization. This chapter closes with the description of a microfluidic model of the probe allowing to predict the behavior of the system. It is worth mentioning this chapter is partly inspired from a scientific article recently published by the author (Petit-Pierre et al. 2016).

### 2.1 Design Considerations

#### 2.1.1 System Requirements

In medical device development, the project starts with the definition of the User Requirements Specifications (URS) and Product Requirements Specifications

## Chapter 2. Neural Probe - Design and Development

---

(PRS), based on the intended use and the needs of the final equipment user. In the context of this work, the requirements answer to the specific needs of the neuroscientist in term of interaction possibilities with the neuronal environment (electrical and fluidic) and in term of connections to the control and measurement systems (existing equipments). As discussed in chapter 1, the neural probe will include:

1. Microchannels for ECF collection
2. Microelectrodes for neuromodulation and neural recording

Starting from there, table 2.1 shows a set of requirements which have been defined and respected along the development course of the neural probe.

Among the most important requirements such as the system spatial and temporal resolution, the probe biocompatibility requirement is a major element which guided the design. Indeed the probe is intended to be inserted in cerebral tissues and should limit body reaction such as inflammation or fibrosis. Even if the device is intended to be used in an acute application <sup>1</sup>, maximal care should be given to minimize the local reaction of the brain which could impact the measurements. The structure of the probe includes Polyimide (PI), SU-8, Pt and Ti. PI is well known for its excellent biocompatibility associated with its good mechanical properties (Richardson et al. 1993; Y. Sun et al. 2009; Seo et al. 2004). SU-8 is an epoxy photoresist which also demonstrates good biocompatibility properties (Nemani et al. 2013; Cho et al. 2008). Pt and Ti are considered as biocompatible metals; Pt is widely used as electrode materials for pacemakers, DBS systems or cochlear implants while Ti is traditionally used for Implantable Pulse Generator (IPG) casings or orthopaedic implants.

In addition to the precedent considerations, the system must be compatible with a reliable detection method suitable for low volume fluid samples (in the order of tens of nanoliter). The chosen analytical method should provide detailed information regarding the sample contents, in particular it should provide access

---

<sup>1</sup>In medical devices development, the mention "long term" relates to an implantation time over 29 days (FDA definition) (Sall 2013)

## 2.1. Design Considerations

**Table 2.1** Set of basic requirements defined for the development of the neural probe.

#	Requirements	Description	Type
<b>1. Indication for use</b>			
1.0	Intended use	The device shall ensure the collection of fluid and the delivery of electrical stimulation to the neuronal tissues	must
1.1	Short term	The device is operated in an acute mode (single use)	must
1.1	Long term	The device should be compatible with long term implantation	should
<b>2. Physical dimensions and configuration</b>			
2.0	Size	Device implanted tip does not exceed a section area of $250\ \mu\text{m} \times 250\ \mu\text{m}$	must
2.1	Fluidic interaction	The device includes a microfluidic system for neurochemical sampling	must
2.2	Electrical interaction	The device includes microelectrodes for tissues neuromodulation and recording	must
2.3	Proximal connecting zone	The device includes a proximal connection zone to couple with the fluidic and electrical driving/recording equipment	must
<b>3. Materials</b>			
3.0	Biocompatibility	Materials in contact with the tissues should be biocompatible and limit tissues reaction	must
<b>4. Performances - mechanical/electrical/fluidics</b>			
4.0	Temporal resolution	The system provides a method for sampling at high temporal resolution	must
4.1	Spatial resolution	Every probe tip active elements are situated on the same surface in close proximity	must
4.2	Device life-time	The system shall remain functional for at least 2 h of continuous operation	must
4.3	Mechanical strength	The device tensile, compression and bending strength shall be sufficient to ensure its integrity during normal handling	must
4.4	Electrical conduction	The device electrical tracks shall have a low Direct Current (DC) resistance to properly conduct electrical signals to/from the microelectrodes	must

## Chapter 2. Neural Probe - Design and Development

---

to the molecular information in direct relationship with the neuronal exchanges taking place in the brain (ionic species involved, neurotransmitters, signaling proteins, etc). Finally, the method must demonstrate high sensitivity and a low detection limits without being affected by the high content of salts which will probably be contained in the brain samples.

### 2.1.2 Microfluidics - Theoretical Basis

#### 2.1.2.1 Basic Laws

The physical properties of microsystems are subjected to subsequent behaviour change compared to larger scale system. This can somehow be unintuitive. For instance, if we consider the ratio between volume forces, such as the gravity, and the surface forces, such as surface tension, the scaling law of this relation can be expressed by:

$$\frac{\text{surface forces}}{\text{volume forces}} = \frac{l^2}{l^3} = l^{-1} \lim_{x \rightarrow 0} \rightarrow \infty \quad (2.1)$$

where  $l$  (m) is a characteristic length of the system. Equation 2.1 shows that the volume forces becomes largely unimportant when scaling down to the microscale. Instead surface forces becomes dominant. This must be taken into account when designing microfluidic systems.

In fluid mechanics, the Reynolds Number (Re) is a dimensionless quantity which is important for predicting the flow pattern of a given fluid in different flow conditions. Re is defined as the ratio between the inertial forces to the viscous forces of a fluid as it reads in the following relation:

$$Re = \frac{\rho V L_0}{\eta} \quad (2.2)$$

where  $\rho$  (kg/m<sup>3</sup>) is the fluid density,  $V$  (m/s<sup>2</sup>) the average fluid velocity,  $L_0$  (m) is a relevant length of the system and  $\eta$  (Pas) is the fluid viscosity. Re calculation is relevant for finding the transition from a laminar to a turbulent flow regime.

## 2.1. Design Considerations

---

At microscale though, the flow of a fluid through a microchannel is characterized by a low  $Re$  (often  $Re < 1$ ) (Bruus 2008). At low  $Re$  number, the flow remains laminar which means no turbulence can be created in this regime. The particles transported in a fluid can therefore be transported with a relative predictable manner. An impacting consequence for microfluidic manipulation is that the mixing can be difficult to perform; two adjacent flows meeting in a single channel will remain separated, for instance.

Poiseuille (or Hagen-Poiseuille) flow describes the pressure driven flow in a channel at steady-state conditions. It derives from a class of solutions to the Navier-Stokes equation (assumptions: incompressible and newtonian fluid) and is of major importance to describe the basic behavior of fluid manipulation in microchannel networks and LOC systems. When a fluid is driven through a long, straight and rigid channel, the resulting pressure drop  $\Delta P$  (Pa) from the flow  $Q$  ( $m^3/s$ ) is described by:

$$\Delta P = R \cdot Q \quad (2.3)$$

$$\Delta P = \frac{8\eta L}{\pi r^4} \cdot Q \quad \text{for circular cross section} \quad (2.4)$$

$$\Delta P = \frac{12\eta L}{wh^3(1 - 0.630\frac{h}{w})} \cdot Q \quad \text{for rectangular cross section} \quad (2.5)$$

Relation 2.3 indicates the flow is proportional to the fluidic resistance  $R$  of a channel for a given pressure drop along the same channel. The fluidic resistance is dependent on the channel cross section geometry and length  $L$  (m). In equation 2.4,  $R$  is defined for a circular channel geometry of radius  $r$  (m) while in 2.5,  $R$  is given for a rectangular cross section of width  $w$  (m) and height  $h$  (m) (with  $h < w$ ). The latter is commonly used in microfluidic design because most of the channels are realized using photolithography methods resulting in channels of rectangular cross section.

## Chapter 2. Neural Probe - Design and Development

In a Poiseuille flow, the flow  $v_x(z)$  has a parabolic profile as expressed in the following relation, a solution to the Navier-Stokes equation taking into consideration the no-slip conditions at the channel walls:

$$v_x(z) = \frac{\Delta P}{2\eta L}(h-z)z \quad (2.6)$$

where two parallel and fixed plates of infinite width and of length  $L$  (m) subjected to a pressure drop  $\Delta P$  were considered (Bruus 2008). This parabolic flow is represented in figure 2.1 in an  $xz$ -plane, the system being invariant in the  $y$  direction.

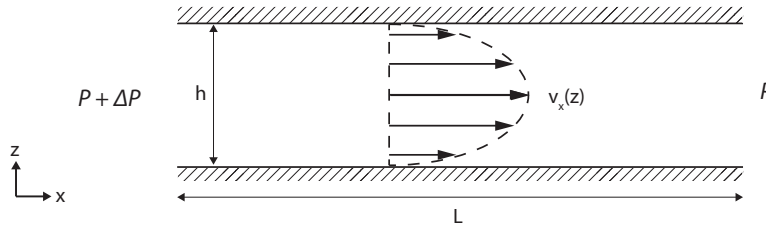


**Figure 2.1** Representation of a Poiseuille flow in an  $xz$ -plane of two parallel plates spaced by  $h$ , with a infinite dimension in the  $y$  direction. The fluid is flowing through the channel in the  $x$  direction due to a pressure difference of  $\Delta P$  over the distance  $L$ .

The Poiseuille equations (2.3, 2.4, 2.5) indicate the fluidic resistance  $R$  is linearly dependent on the channel length  $L$ . However,  $R$  is quadratically dependent on the cross section area of the channel. These elements are impacting the microfluidic driving equipment; long channel of small cross section area can require a huge pressure difference to establish a flow.

In neural probe technology, microfluidic channels are still an excellent option for establishing a precise chemical interaction with the tissues. Successful integration of microfluidic channels in polymer-based neural devices were recently demonstrated by several groups (Altuna, Bellistri, et al. 2013; Minev et al. 2015). In these examples the microfluidic channels were used in order to perfuse drugs in the medium. One can also envision to use microchannels to sample molecules from the tissues as it is the case in microdialysis. An issue with this method is the Taylor dispersion occurring in the sampling tube which limits the temporal resolution that can be achieved (Aris 1956). Taylor dispersion is an effect in

## 2.1. Design Considerations

which a finite distribution of solute in a liquid flowing through a tube tends to spread under the combined action of molecular diffusion and the variation of velocity over the cross-section (Taylor 1953). A representation of this effect is shown in figure 2.2. Figure 2.2 (a) shows the initial configuration ( $t = 0$ ) of a considered homogeneous band of solute (represented in dark gray). If the molecular diffusion is neglected the plug gets stretched around a paraboloid shape as it is subjected to a steady Poiseuille flow  $\mathbf{v}$  oriented along the  $x$  axis as showed in figure 2.2 (b). The molecular diffusion driven by concentration gradients tends to counteract the longitudinal spreading: in the front end it brings solute particles towards the channel wall whereas at the front back it brings the particles near the center ( $z$  axis). The deformed solute shape gets evened out and is enlarged compared to the initial compact configuration as represented in figure 2.2 (c). As a consequence the temporal history of the solute is distorted which results in a loss of resolution.

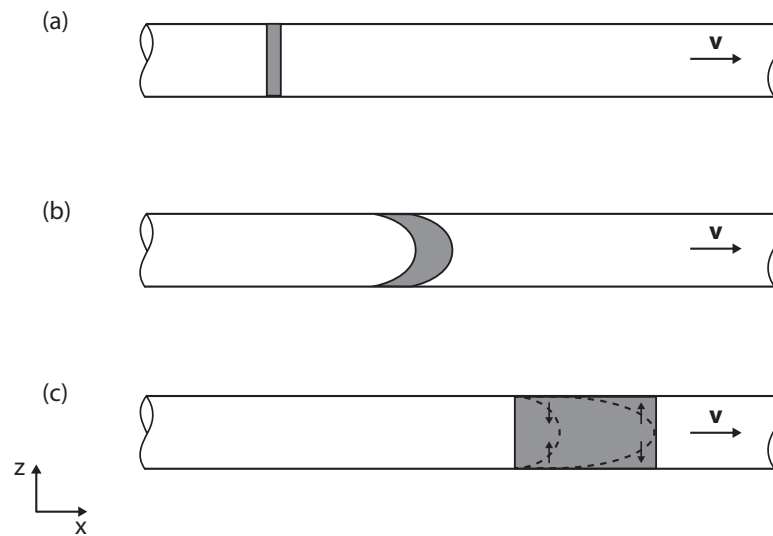


**Figure 2.2** Sketch of the Taylor dispersion that occurs in a cylindrical tube subjected to a steady Poiseuille flow  $\mathbf{v}$  along the  $x$  axis. (a) Initial condition; the solute is compact and homogeneous. (b) After a while, the solute tends to disperse in a paraboloid shape. (c) Under radial molecular diffusion indicated by the vertical arrows, the solute is evened out and enlarged compared to the initial situation.

An answer to the Taylor dispersion issue could be found in the implementation of segmented flows and droplets transport within the probe microfluidic channels. The segmentation of the collected liquid by a non-aqueous phase limits Taylor

## Chapter 2. Neural Probe - Design and Development

---

dispersion because each droplet includes a sub-sample enclosed in a defined space. If the droplet is conserved in the same state and does not fuse with another one during the transportation to the analysis spot, the temporal resolution of the sampling, defined by the time between two generated droplets, is maintained.

### 2.1.2.2 Droplet Microfluidics

Tremendous work on droplet microfluidics has been carried out with the perspective to use this method for Lab-on-a-Chip applications. Droplet microfluidics is based on the separation of a continuous phase by sections of an immiscible fluid or by gas bubbles. One of the motivations in developing this technology was to avoid axial dispersion occurring in non-segmented flows (Seemann et al. 2011). Several ways to generate droplets were demonstrated. With the T-junction configuration, the break-up of a continuous stream is caused by the meeting with a second perpendicular immiscible stream and the consequent shear stress generated as showed in figure 2.3 (a) (Song et al. 2003). Figure 2.3 (b) shows another method called flow-focusing which uses two streams of continuous phase to narrow a perpendicular dispersed liquid in a cross junction until the pinch-off takes place (Anna et al. 2003). These methods are of particular interest when combined with biological applications.

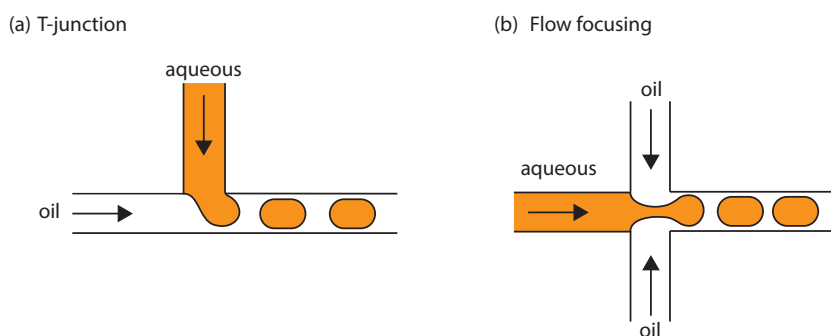


**Figure 2.3** (a) In the T-junction configuration, droplets are generated when a continuous aqueous stream meets a perpendicular immiscible phase. (b) In the flow-focusing method, two opposed streams meet a perpendicular aqueous phase which is narrowed until the creation of droplets.

The chemistode presented by Chen *et al.* typically combines the field of droplet



microfluidics with biology (D. Chen et al. 2008). This device aims to manipulate chemical signals instead of electrical signals as usually done with electrodes. The chemistode includes PDMS V-shaped microchannels. It uses droplets surrounded by an oil carrier phase in order to deliver or record molecular signals to/from a biological substrate such as a cell or tissues. Although the chemistode opens new perspectives regarding chemical interaction, it is however not designed with implantable grade material and therefore excludes *in vivo* neurological applications. In another application, Slaney *et al.* presented a push-pull probe combining microdialysis with droplets segmentation (T. R. Slaney et al. 2011). In their approach, after the extraction, the liquid was separated by an oil phase which improved temporal resolution and facilitated the analysis of the samples. However, this method required the development of an external segmentation device connected to the output flow of the probe. Furthermore, it does not address the diffusion which still occurs between the sampling spot and the generation of the droplets.

### 2.1.3 Microelectrode - Theoretical Basis

#### 2.1.3.1 Tissue-electrode interface

Microelectrodes as electrical neural interface have been extensively studied in the past 60 years. They can take various shapes, from the single Pt wire to flexible multi-electrode arrays. The electrode-tissue interface is usually characterized using impedance spectroscopy (Metz, Bertsch, et al. 2004; Mercanzini, Colin, et al. 2009; Altuna, Menendez de la Prida, et al. 2012). Impedance is an electrical measure of a system resistance to the passage of an alternative current. It is defined as the quotient between an applied potential  $V(t)$  varying with the time  $t$  (typically a sinusoidal variation) and its resulting current  $I(t)$ . When written as complex values, the relation reads:

$$Z(f) = \frac{V(t)}{I(t)} \quad (2.7)$$

## Chapter 2. Neural Probe - Design and Development

---

where  $f$  is the oscillation frequency. For simplification purpose, sinusoidal voltages and currents can be written as a complex function where their real part is the actual voltage and current. Consequently, they are expressed by:

$$V(t) = V_0 e^{i2\pi f t} \quad (2.8)$$

$$I(t) = I_0 e^{i(2\pi f t - \theta)} \quad (2.9)$$

where  $i$  is the imaginary number,  $V_0$  and  $I_0$  are the voltage and current amplitude, respectively, and  $\theta$  the phase shift between the voltage and current. The complex expression of impedance  $Z$  becomes:

$$Z = \frac{V_0}{I_0} e^{i\theta} = |Z| e^{i\theta} \quad (2.10)$$

where  $|Z|$ , the impedance modulus, is the ratio between the current and voltage amplitude whereas the impedance phase  $\theta$  represents the phase shift between them. Relation 2.10 can also be written as:

$$Z = R + i \cdot X \quad (2.11)$$

where  $R$ , the real part, is called the resistance and represents the opposition to the current in the situation where no shift between the voltage and current occurs.  $X$ , the imaginary part, is the reactance and contributes when a shift occurs. In electrodes in contact to biological tissues, this shift is mainly capacitive; it represents the ability of a material or biological matter to store charges. Impedance spectroscopy is the measurement of the impedance value for a wide range of frequencies for a given system. This provides a comprehensive understanding of the electrode-tissue electrical interaction. Impedance is often represented in a Bode plot ( $\log(|Z|)$  vs.  $\log(f)$  and  $\theta$  vs.  $\log(f)$ ), the frequency range being generally comprised between 100 Hz and  $1 \times 10^7$  Hz. Figure 2.4 (c) shows a typical impedance spectroscopy plot ( $|Z|$  and  $\theta$ ) recorded with  $50 \mu\text{m}$  circular Pt electrodes introduced in a mouse brain tissues (Bédurier et al. 2015).

## 2.1. Design Considerations

---

A metal placed in an electrolytic environment such as the brain ECF is subjected to chemical reactions, oxidation and reduction, involving the medium ions and the metal electrode. This results in the accumulation of charges at the electrode surface and in the accumulation of ions in the solution, in close proximity to the metal surface. This specific arrangement is called an electrical *double layer*. Although the formal electrical description of the double layer consists in a Helmholtz capacitance  $C_H$  in series with a Gouy-Chapman capacitance  $C_{GC}$ , experimental results have shown that a Constant Phase Element (CPE) is a good model of this interface. Electrode surface micro-geometry (roughness) gives rise to a fractal electrical equivalent model composed of a combination of resistances and capacitances (Levie 1965). This fractal configuration is better described by a CPE than a capacitance. A thorough description of the metal-tissue/electrolyte interface would also take into consideration electrochemical exchanges occurring at the electrode surface in a non-equilibrium situation. In particular, a resistance to the charge-transfer process ( $R_{CT}$ ) and a Warburg impedance ( $Z_W$ ) representing the ions accumulated or depleted in proximity with the electrode are sometimes considered. This subject will not be covered in detail here but the interested reader is referred to (Kovacs 1994).

A typical electrode-tissue interface configuration is represented in figure 2.4 (a). The model elements comprise; (i) a neural probe made of a dielectric insulating material (light orange) and a metal electrode (yellow), (ii) the neuronal tissue (light grey). In figure 2.4 (b) an equivalent electrical circuit from the probe microelectrode to a large counter electrode models the interface. In particular, the tissue electrical resistance  $R_{bulk}$  is arranged in series with the CPE while a dielectric capacitance  $C_{dielectric}$  (probe insulation) is mounted in parallel to the first two elements. Figure 2.4 (c) is a typical impedance spectrum of such a system recorded with a circular Pt microelectrode (diameter  $d = 50\mu m$ ) implanted in cerebral tissues of a mouse (adapted from Bédurier et al. 2015). We note the system impedance ( $|Z|$ ) is capacitive at low frequencies (from  $f = 100$  Hz to  $1 \times 10^5$  Hz) before reaching a resistive plateau (at  $f = 1.5 \times 10^5$  Hz) matching with the moment the phase is closest to zero. At this point, the impedance value corresponds to the external tissue resistance,  $R_{bulk}$ , as described by the Peak Resistance Frequency (PRF) method (Mercanzini, Colin, et al. 2009; Bédurier et al.

2015).

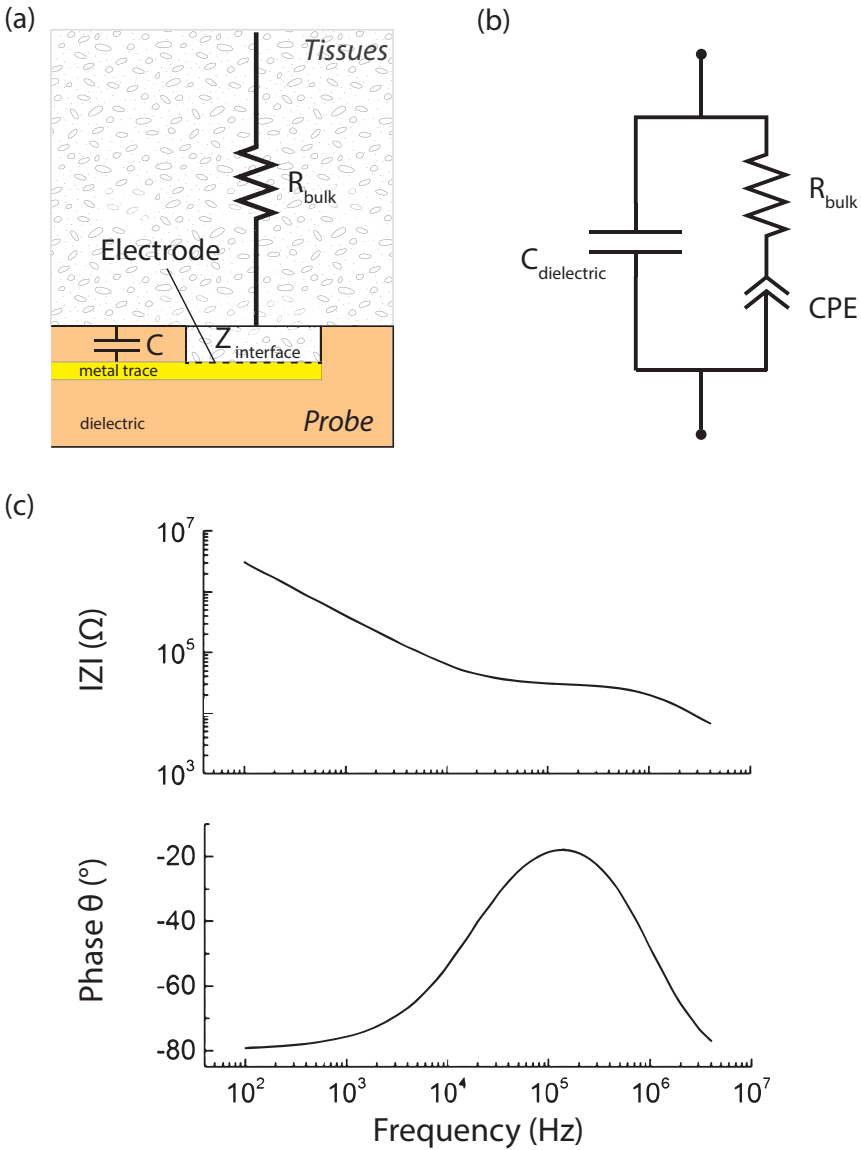


**Figure 2.4** (a) Representation of the tissue-probe interface with the different contributing elements. The probe is made of a dielectric material (light orange) on which is patterned an electrode in contact with the tissues (yellow).  $R_{bulk}$  is the tissues resistance,  $C$  is the dielectric capacitance between the metal trace (isolated) and the tissue and  $Z_{interface}$  represents the tissue-electrode impedance. (b) Equivalent electrical model.  $Z_{interface}$  is represented by a CPE, which best describes the electrode-tissue interface at the considered frequencies. (c) Typical impedance spectrum recorded from a mouse brain (adapted from Bédier et al. 2015)

### 2.1.3.2 Electrode Geometry

The geometrical configuration of an electrode determines the principal characteristics of the electrical interaction with the tissues. We distinguish monopolar (or unipolar) microelectrodes from multipolar electrodes. Monopolar microelectrodes are electrodes in the microscale range (main dimension from  $10\mu\text{m}$  to  $50\mu\text{m}$ , in general) connected to a much larger counter electrode via a conductive medium (such as biological tissues). Monopolar circular electrodes are the most represented in neural probe technology (Mercanzini, Colin, et al. 2009; Altuna, Bellistri, et al. 2013; Bédier et al. 2015). The bipolar electrode denomination is used when an electrode is connected to a single adjacent electrode, the multipolar denomination when an electrode is connected to multiple adjacent electrodes. Planar circular microelectrodes are well represented in neural interfaces as (i) this geometry is well compatible with the microfabrication processes which further allows to minimize electrode surface roughness and (ii) they are axis-symmetrical thus avoiding any charge accumulation at edges.

In monopolar configuration, the current density is mainly concentrated in direct proximity to the electrode and diverge in the tissue as represented in figure 2.5 (a). The consequence of this inhomogeneous current density distribution is that almost all the contribution to the impedance is provided by a small tissue volume nearby the electrode. The current and potential lines produced by a planar monopolar disc electrode of radius  $a$ , electrically isolated on its border, submerged in an infinite biological medium and exposed to a half-spherical counter electrode placed at infinite distance has been reported by Newman in 1966 as showed in figure 2.5 (b) (adapted from Newman 1966). In this description, rotational elliptic coordinates have been used and defined as follow:

$$z = a\xi\tau \tag{2.12}$$

$$r = a\sqrt{(1 + \xi^2)(1 - \tau^2)} \tag{2.13}$$

## Chapter 2. Neural Probe - Design and Development

---

where  $a$  is the electrode radius,  $z$  is the normal distance to the electrode,  $r$  is the distance to the axis of symmetry of the system,  $\xi$  are equipotential lines and  $\tau$  are the current lines. Laplace's equation can be solved analytically in this system of coordinates and gives rise to the following expression for the potential  $\Phi_z$ :

$$\frac{\Phi_z}{\Phi_0} = 1 - \frac{2}{\pi} \arctan(\xi) \quad (2.14)$$

where  $\Phi_0$  is the potential at the electrode surface ( $\Phi_z = \Phi_0$  at  $\xi = 0$ ) (Newman 1966). In figure 2.5 (c),  $\frac{\Phi_z}{\Phi_0}$  was computed for a  $10\mu\text{m}$  radius disc electrode and for  $\tau = 1$ ; the current line orthogonal to the disc electrode. A rapid decrease of the potential is observed; at  $z = 10\mu\text{m}$  (= electrode radius) the potential is decreased by 50% whereas at  $z = 63\mu\text{m}$ , the potential is decrease by 90 %. This means that almost 90% of tissue contribution to the impedance is produced by a half sphere of tissue of a radius equivalent to 3x the electrode diameter. For recording as for stimulation applications, one must take into account that the volume of tissues which is either recorded or stimulated is in the same order of magnitude than the electrode main dimension.

### 2.1.3.3 Electrode Materials

The most comprehensive experience regarding the use of implantable electrode is related to the cardiac pacemakers that have been used in clinical practice for more than 50 years. Neuromodulation applications such as DBS greatly benefited from the experience gathered in this field, especially regarding the electrode materials and their stability in the body. In term of electrode material, we distinguish noble metal electrodes such as Pt from non-noble metal like stainless steel. An important electrode material characteristic is the maximum charge delivery capacity  $Q_{\text{CDC}}$ .  $Q_{\text{CDC}}$  is a measure of all the reactions that contribute to the charge transfer from an electrode to an electrolyte; it is defined as the area under the voltage-current curve (also voltamogram) recorded in a cyclic voltammetry setup. This value also includes any effects (and technologies) which influence the surface roughness of an electrode thereby modifying its active area.  $Q_{\text{CDC}}$  values obtained from

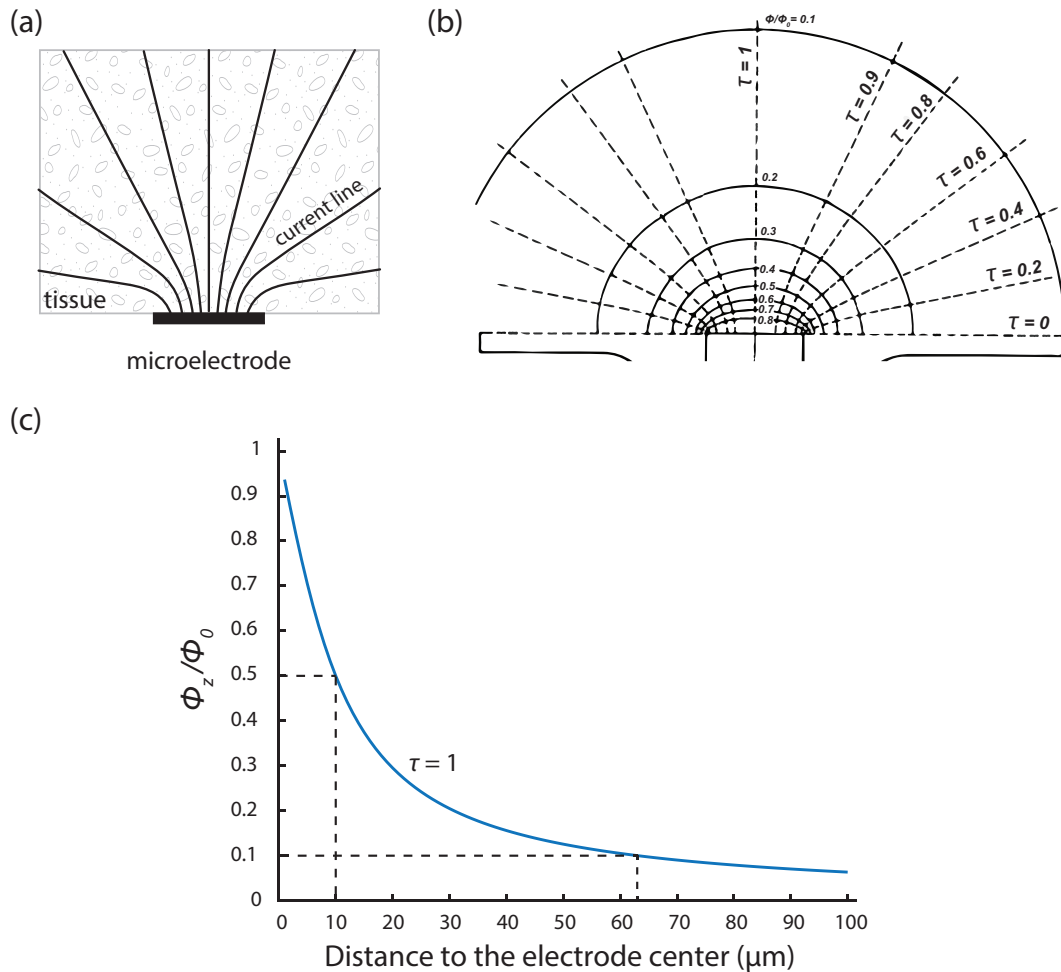


**Figure 2.5** (a) Dispersion of current lines in the tissues from a microelectrode to a counter electrode placed at an infinite distance and whose surface is infinitely large. (b) Analytical solutions to the current and potential lines generated by a planar monopolar electrically insulated disc electrode placed in an infinite biological medium and opposed to a half spherical counter electrode placed at the infinite.  $\tau$  are the current lines,  $\frac{\Phi}{\Phi_0}$  the equipotential lines (adapted from Newman 1966). (c) Potential drop (relative to  $\Phi_0$ ) perpendicular to a disc electrode (current line  $\tau = 1$ ) of radius  $r = 10 \mu\text{m}$ . The tissues potential contribution is reduced by 50 % at a distance equivalent to the microelectrode radius.

pulse tests<sup>2</sup> for gold, stainless steel and platinum are given in the table 2.2 (Stieglitz 2004). Among the noble metals such as gold, platinum and iridium, platinum (Pt) and its alloys are certainly the most widely used for implantable

<sup>2</sup>Common electrode characterization test investigating the electrode behavior under real stimulation conditions. The interested reader is referred to chapter 6.3 of the reference (Stieglitz 2004) for a complete description.

## Chapter 2. Neural Probe - Design and Development

---

**Table 2.2** Maximum charge delivery capacity  $Q_{CDC}$  for several electrode materials (Stieglitz 2004)

Electrode material	Maximum Charge Delivery Capacity $Q_{CDC}$ ( $\mu\text{C cm}^{-2}$ )
Gold	20
Stainless steel	50
Platinum	75

electrodes. Pt charge delivery and injection capacity is well characterized. The chemical reactions occurring at the interface with a saline solution includes the chemically reversible charging process of the double-layer as well as electrode surface oxidation or reduction. Generally, a maximum allowed electrode charge density of  $50 \mu\text{C cm}^{-2}$  is admitted to remain in the safe limit in implantable use (Fontaine et al. 2009; Grill 2005). Under this threshold, neither corrosion nor plating of Pt occurs.

Common non-noble metals for electrode material include the stainless steel 316 LVM, a nickel-cobalt alloy also called Elgiloy, and the MP35N, a cobalt-nickel-chromium-molybdenum alloy. A characteristic of these metals is that they form a passive film at their surface to protect from corrosion. When they are used to stimulate the tissues they inject charges by Faradic processes involving oxidation and reduction of this protective layer. Corrosion occurs if the material is driven above its safe charge injection limit resulting in the breakdown of the passive layer. In this undesired situation the metal dissolves in the solution while the water is hydrolyzed resulting in electrode failure and degradation of the biological tissues. In noble metals this phenomenon is very limited compared to non-noble metals, which may explain why Pt is a common implantable electrode material.

The goal of this subsection was to briefly introduce some material notions in implantable electrodes. For further details, the interested reader is referred to the book chapter written by Thomas Stieglitz where a thorough description regarding electrode materials for recording and stimulation application is presented (Stieglitz 2004).



## 2.2 Neural Probe - Geometry and Functions

In the following, we propose a novel concept of neural probe integrating Pt electrodes and a microfluidic T-junction in the distal tip. The collection system allows for a controlled sampling of fluid in droplets (nanoliter range) separated by non-aqueous segments. This approach solves the diffusion problem occurring from the collection point to the analysis of the sample. It allows for a fast sampling rate and therefore a high temporal resolution (under the second). As mentioned in chapter 1, microfabrication methods can be employed in order to address the specific requirements regarding size and biocompatibility of the device. Working with micro-scale devices brings the question of the connectivity with the macro-environment. Microelectrodes with a thickness of a few tens of nanometers deposited on flexible polymers can be challenging to connect to electrical wire in the millimeter range. Therefore, the design of the probe will include the development of an interface unit to join the macro and the micro environment. A block diagram representing the elements included in the device is shown in figure 2.6. The neural probe is a central element of this architecture; its distal tip (probe active area) is intended to be implanted in the tissues while its proximal side (probe connective area) is intended to be connected to the microfluidic and electrical control units.

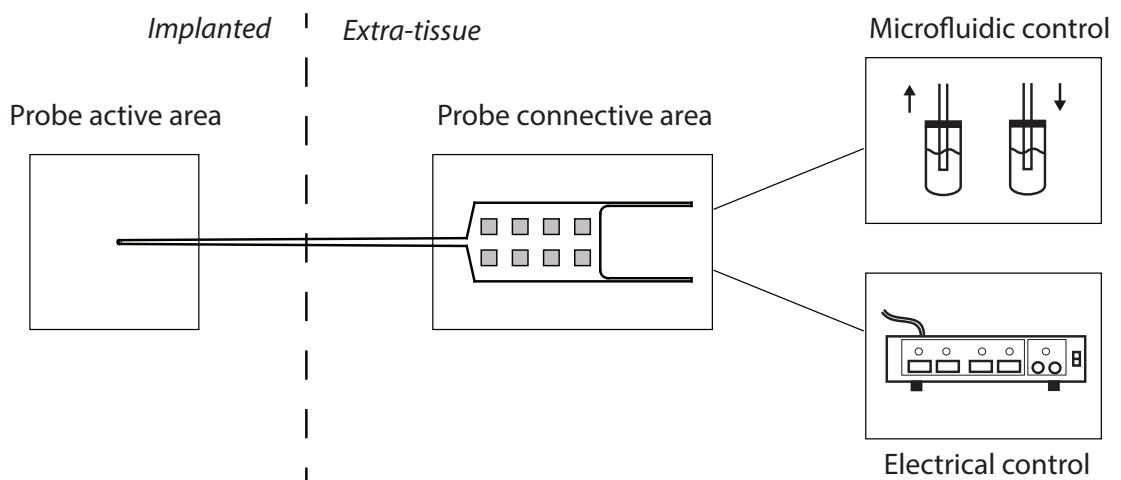


**Figure 2.6** Block diagram of the neural probe. Only the tip of the probe will be implanted in the tissues. The extra-tissue region includes the connective zone which serves of interface with the microfluidic and electrical control.

## Chapter 2. Neural Probe - Design and Development

Figure 2.7 (a) shows a top view of the probe as well as its main dimensions. The elongated probe tip presents the advantage to leave some space between the animal and the connective zone during the *in vivo* manipulations. The proximal zone contains the electrical contacts as well as 2 fluidic entries, an inlet and an outlet, situated at the extremity of each probe leg as shown in figure 2.7 (b) (details B and C). Figure 2.7 (b) shows the microchannels path (orange continuous line) which connects the proximal fluidic inlet and outlet to the sampling inlet included at the distal tip, as pointed out in detail A. There, the u-shape path of the channel meets with the probe tip inlet in a T-junction configuration.

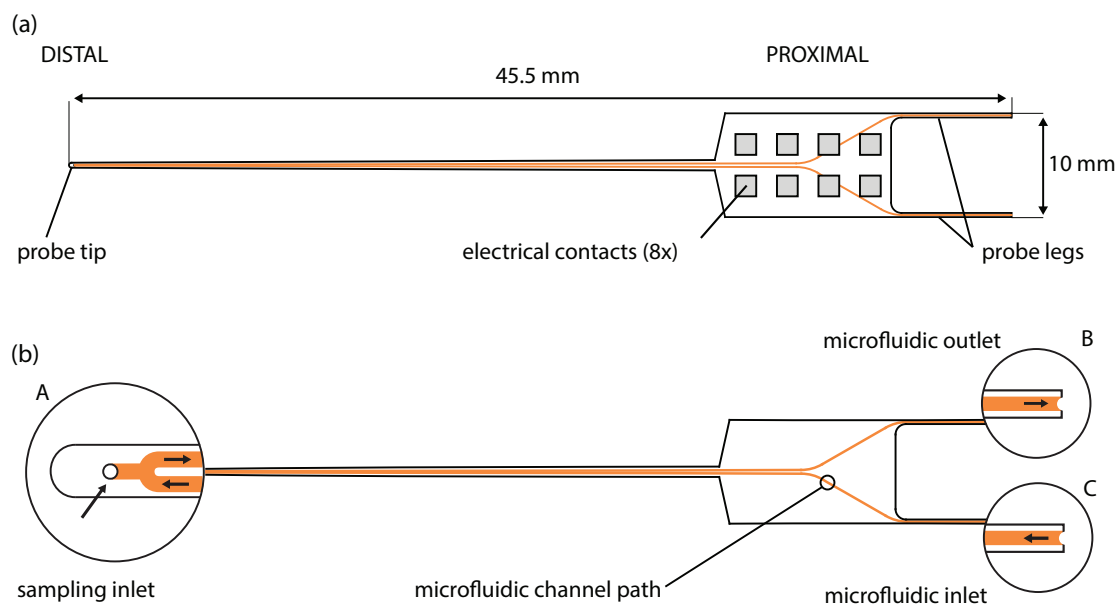


**Figure 2.7** (a) Overall neural probe dimensions. The proximal contacts are electrically connected to the probe tip microelectrodes whereas the microfluidic network is represented in orange (b) Detail of the 3 fluidic entries of the probe; at the tip (A), the proximal outlet (B) and inlet (C). The black arrows indicate the flow direction.

The probe tip region is detailed in figure 2.8. Figure 2.8 (a) shows the circular microelectrodes spatial configuration and their dimension. We note the round-shaped probe tip designed for an atraumatic insertion in cerebral tissues. Figure 2.8 (b) shows the monolithically integrated microfluidic channels connecting with the sampling inlet. Two droplet detection electrodes in contact with the inner space formed by the microchannel are shown as well. Their surface area are  $80 \times 80 \mu\text{m}^2$ . These electrodes are meant to count the aqueous droplets separated by

oil plugs by monitoring the change of conductivity between these 2 phases.

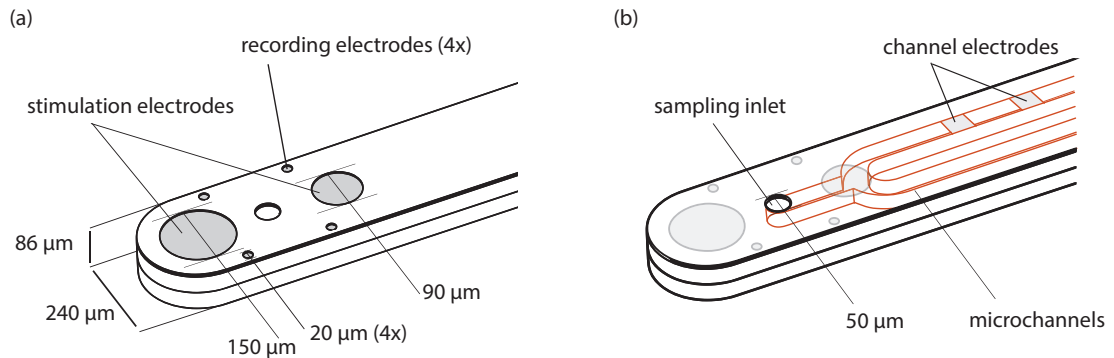


**Figure 2.8** 3D sketch of the atraumatic distal tip configuration. (a) Main dimensions of the probe tip. Two large stimulation electrodes ( $150\mu\text{m}$  and  $90\mu\text{m}$ ) as well as 4 recording electrodes ( $20\mu\text{m}$ ) are included on the top layer of the probe. (b) Detail of the microfluidic channel network (in orange) at the probe tip, on the same device. The sampling inlet ( $50\mu\text{m}$ ) joins the main u-shape microchannel

## 2.3 Microfabrication

We used here a rather unconventional approach for the microfabrication of the devices. Instead of starting with the back of the probe and ending with the probe top layer, the opposite procedure was followed. It allowed to concentrate every active elements on the same surface of the final device. The active elements include the Pt electrodes and the sampling inlet assembled on a PI base. The main steps of the fabrication process are summarized in Figure 2.9.

As it can be observed, two silicon wafers were processed in parallel. On the first wafer, a  $1\mu\text{m}$  thick WTi(200 nm) - Al(800 nm) sacrificial layer was sputtered. Then, a  $3\mu\text{m}$  PI layer was spin-coated and patterned using photolithography. Before the etching step, a process optimization step was implemented: a reflow of the photoresist mask (AZ-92XX) at  $115^\circ\text{C}$  during 2 min was performed. By transferring the pattern to the PI, this allowed to generate a conical profile rather than a vertical wall between the two levels of the metal layer (electrical tracks and electrodes). A 350 nm sandwich Ti-Pt-Ti metal layer was then sputtered and

## Chapter 2. Neural Probe - Design and Development

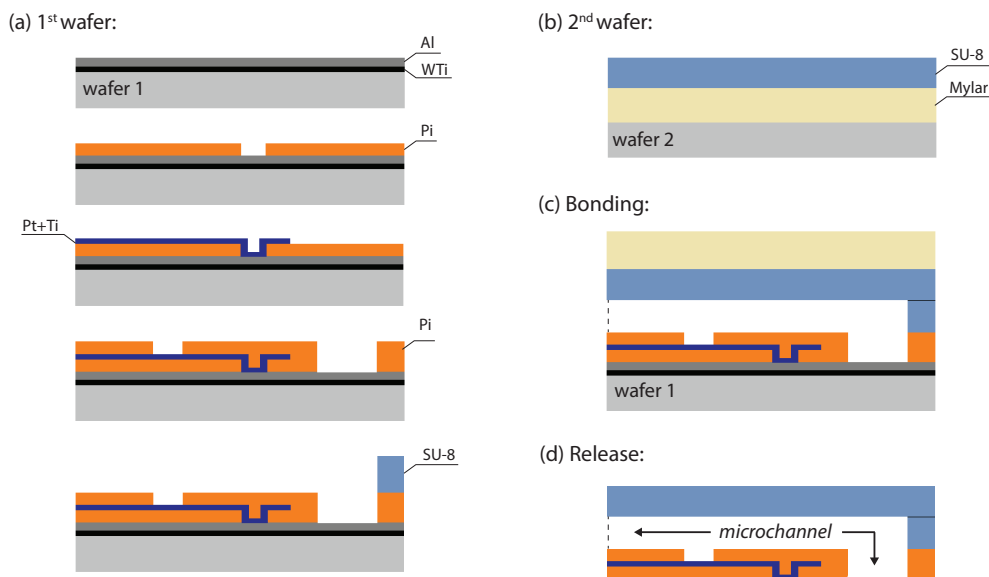
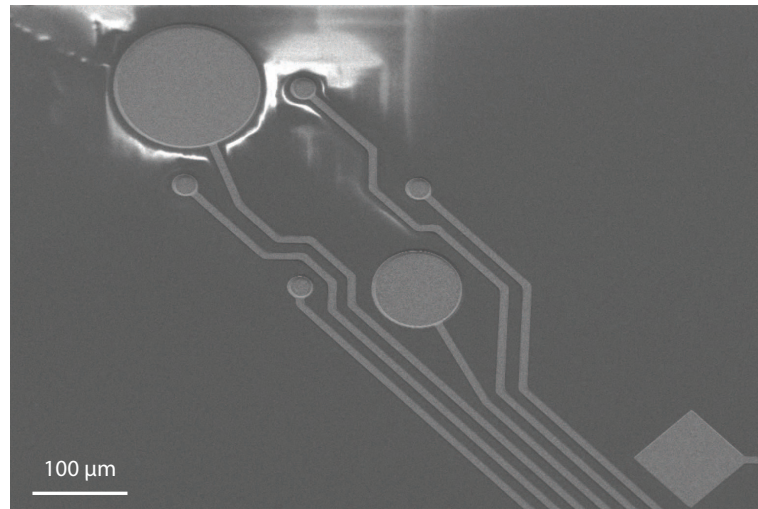


**Figure 2.9** Main fabrication steps of the neural probe. (a) The first wafer includes PI, Pt (platinum) electrodes and SU-8 (microchannels wall). (b) The second wafer includes a Mylar film and a SU-8 layer (microchannels cover). (c) The bonding is performed by lamination before the final release of the probe (d).

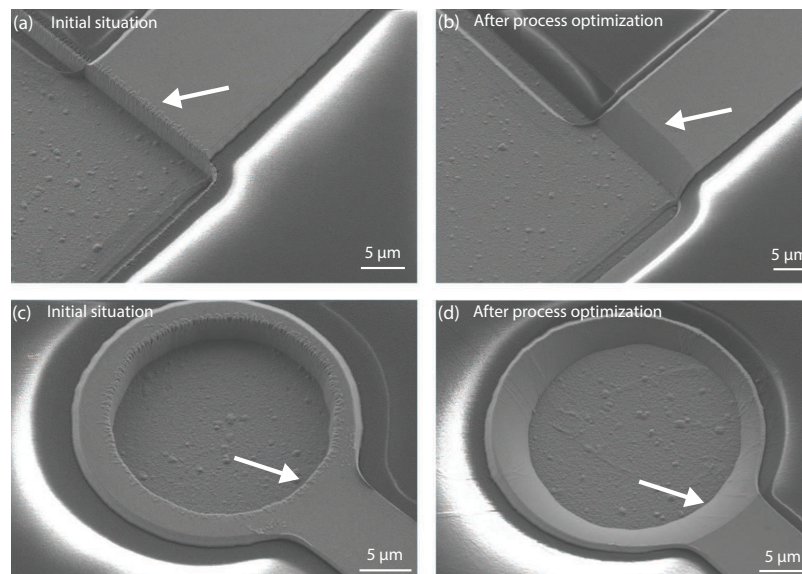
etched to form the electrodes and the electrical tracks. Figure 2.10 shows an intermediate step of the microfabrication process (after metal deposition and etching) focusing on the probe tip region. We notice the circular electrodes are situated on a lower level ( $3\mu\text{m}$  under) than the electrical tracks.

Figure 2.11 (a) and (c) show specific transition areas where the change of level occurs without process optimization (without photoresist reflow). The transition between the upper and bottom level is vertical, thin and prone to damages if the film is bent. In contrast, figure 2.11 (b) and (d) show the same regions on another sample on which photoresist reflow was performed prior to metal deposition. The metal transition between the two levels is much smoother while the thickness of the trace (transition section) is only slightly thinner than on a flat surface.

The electrical insulation between the metal traces was obtained with a second spin-coated PI layer patterned by photolithography. It allowed to open electrodes included into the microfluidic channel as well as the sampling inlet. Finally, a  $40\mu\text{m}$  thick SU-8 photoresist layer was deposited and patterned by photolithography. It served as a structural material forming the microchannel walls.



**Figure 2.10** Detail of the distal region of the neural probe comprising the set of microelectrodes at an intermediate fabrication process step. The SEM picture was taken after the metal deposition and the electrical tracks etching. The electrode surfaces are a step under ( $3\mu\text{m}$ ) the level of electrical tracks.



**Figure 2.11** Effect of photoresist reflow prior to PI etching and metal deposition. (a) and (c) show regions of electrical track level change when no reflow was performed prior to metal deposition. In comparison, (b) and (d) show the same regions on different devices where a reflow was performed. The metal transition from the two levels is much smoother in this case.

A  $50\mu\text{m}$  Mylar film was laminated on the second wafer. A droplet of water was applied between the wafer and the Mylar foil to enhance the bonding (Steigert

## Chapter 2. Neural Probe - Design and Development

---

et al. 2008). Then, a  $40\ \mu\text{m}$  thick SU-8 layer was spin-coated over the film and soft-baked. After this step, the Mylar film with the SU-8 layer on the top was peeled off the second wafer. Then, the Mylar and SU-8 structure were flipped bottom-up and assembled on the top of the first wafer. The bonding between the SU-8 layers was obtained by lamination applying heat ( $60\ ^\circ\text{C}$ ) and a compression force (36 kg, between the rolls). A final photolithographic step (exposition through the Mylar film) allowed to reinforce the bonding.

The release of the probes was performed by anodic dissolution of the sacrificial layer according to the method proposed by Metz *et al.* (Metz, Jiguet, et al. 2004). After the release, the devices were dipped in a 10:1 HF-DI water solution for 10 s to remove the Ti layer above the Pt layer.

The previously described process was optimized over 5 fabrication batches. The most challenging step consisted in the bonding between the top and bottom layers of SU-8. The roller lamination as well as the exposition through the Mylar film allowed to improve drastically the reliability and brought the production yield from 15% to 85 % after implementation (each wafer includes 32 neural probes).

### 2.4 Neural Probe - Features

A neural probe including microfluidic channels, recording and stimulation electrodes was successfully fabricated. A microscale T-junction droplets generator has been included in the tip of the probe. This enables the collection and the direct segmentation of the extracted fluid. The proximal area of the probe includes two legs which constitute the input and output of the microfluidic channels. On the same region, the electrical contacts ( $2\ \text{mm} \times 2\ \text{mm}$ ) allow to make the connection with the electrodes of the distal tip. Two microfluidic channels of rectangular section ( $40\ \mu\text{m} \times 80\ \mu\text{m}$ ) cross the structure from the legs to the tip of the probe. They join at the distal tip where they form a T-junction with a third microchannel connected to the sampling inlet ( $D = 80\ \mu\text{m}$ ). Close to the sampling inlet, two stimulation electrodes with a diameter of  $150\ \mu\text{m}$  (distal) and  $100\ \mu\text{m}$  (proximal) are distributed longitudinally. The proximal stimulation electrode is smaller in



## 2.4. Neural Probe - Features

order to provide sufficient room for the electrical tracks ( $10\mu\text{m}$ ) passing nearby. Four recording electrodes with a diameter of  $20\mu\text{m}$  are distributed in a tetrode-like configuration. This permits to discriminate signals from individual neurons when recording. Square electrodes ( $80\mu\text{m} \times 80\mu\text{m}$ ) are integrated inside the channel, facing down. Each of these elements is presented in figure 2.12. The white dashed-line highlights the path of the microfluidic channels. A zoom on the distal tip shows the electrodes.

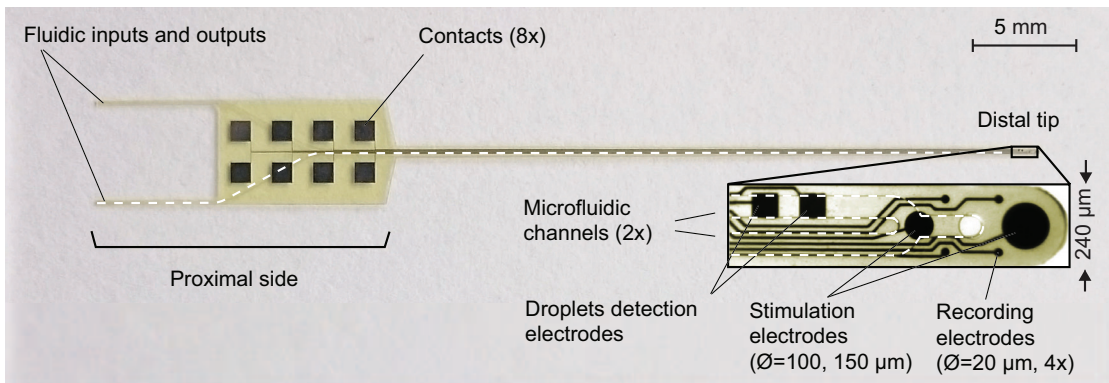


**Figure 2.12** Polyimide and SU-8 based neural probe after microfabrication. The device includes stimulation and recording Pt (platinum) electrodes as well as 2 microfluidics channels joining at the distal tip to form a T-junction (droplets generator). The white-dashed line represents the microchannels pathway.

On the left of figure 2.13 is presented a cross section view of the probe tip performed with a scanning electron microscope (SEM, LEO 1550). The openings of the two microchannels as well as the 8 electrical tracks assembled on the top of the structure are well distinguishable. We observe that a slight misalignment occurred between the SU-8 cover and the rest of the structure during the bonding. On the right of figure 2.13, a SEM picture shows the two stimulating electrodes as well as the 4 recording electrodes. The sampling inlet at the middle of the tetrode electrodes can be observed as well (white arrow).

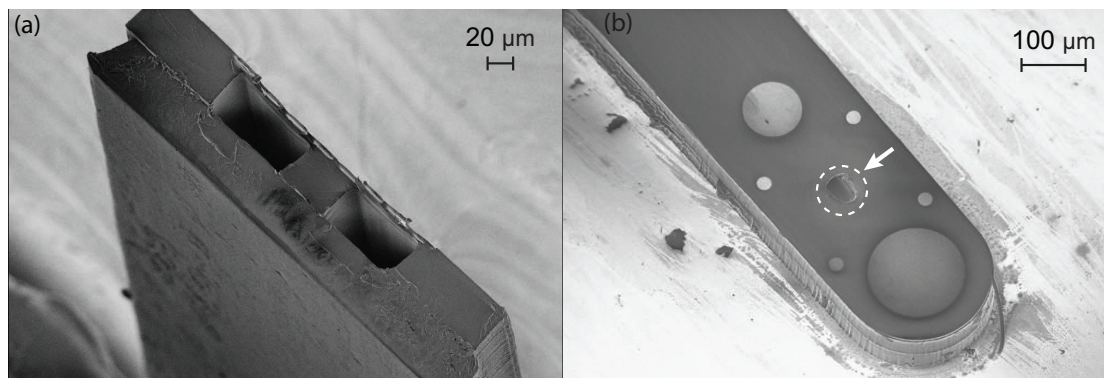


**Figure 2.13** (a) SEM picture of the probe tip after a cross-section cut. The microchannels are open, and, on the top of them, we observe the 8 electrical tracks. (b) The stimulation and recording electrodes as well as the sampling inlet (white arrow) are integrated on the same surface, in close proximity to each other.

## 2.5 Neural Probe - Microfluidic Model

The probe microfluidic network is composed of 3 entries which connect in a T-junction as represented in figure 2.14. Figure 2.14 (a) details the distal tip of the neural probe where the droplet generation occurs by controlling the Perfluoromethyldecalin (PFD) input  $Q_{in}$  and output  $Q_{out}$  flows.  $Q_{sampled}$  is the resulting inflow of the aqueous phase external to the probe. Figure 2.14 (b) is an equivalent fluidic T-junction model of this system.

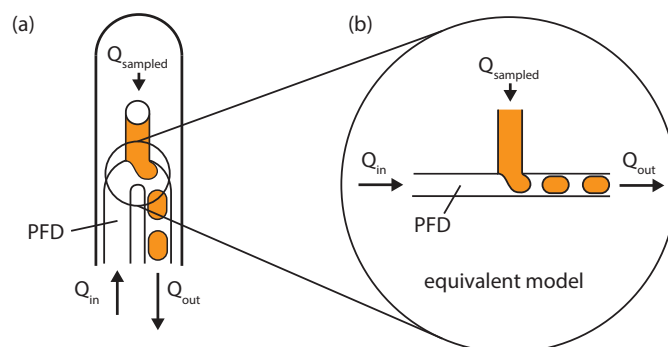


**Figure 2.14** (a) Microfluidic network at the distal tip of the neural probe. This 3 entries system is composed of the flows  $Q_{in}$ ,  $Q_{out}$  and  $Q_{sampled}$ . In this system, the white phase is the PFD whereas the aqueous phase is orange. (b) T-junction analogy modelling the probe tip microfluidic system.



## 2.5. Neural Probe - Microfluidic Model

---

At the junction of the channels, the mass conservation condition requires the sum of flows equal zero:

$$\sum_i Q_i = 0 \quad (2.15)$$

This relation, together with equation 2.3, are similar to the fundamental laws of electricity. Indeed the linear pressure-flow relationship is analogous to Ohm's law  $U = R \cdot I$  binding the current  $I$  to the potential difference  $U$ . The mass conservation is reminiscent of Kirschhoff's law  $\sum I = 0$  at electrical nodes of circuits. It is therefore interesting to establish a link between the fields of electronics and microfluidics; the electrical current, the potential and the electrical resistance becoming the flow, the pressure and the fluidic resistance, respectively. This is of interest for modeling the behaviour of microfluidics. Figure 2.15 is a fluidic equivalent model of the probe showed in figure 2.7. In this model the intersection **T** represents the junction at which the microchannels connect, where the T-junction droplet formation occurs.  $P_T$  is defined as the pressure at this intersection,  $P_{ext}$  is the external pressure at the probe distal tip, near to the sampling inlet,  $P_{in}$  is the pressure applied at the proximal inlet and  $P_{out}$  is the pressure applied at the proximal outlet.  $R_1$  is the channel fluidic resistance from the proximal entries to the point **T** which is equivalent in both the upper and bottom channel by symmetry.  $R_2$  is the fluidic resistance from the distal tip sampling inlet to the point **T**.  $Q_{in}$ ,  $Q_{out}$  and  $Q_{sampled}$  are the resulting flow from the pressure difference between the point **T** and the microchannel inlet, outlet and the sampling inlet, respectively. We make here the hypothesis the channel walls are rigid and the fluid is incompressible; we therefore didn't consider any capacitance in this model. By the mass conservation law we can write:

$$Q_{sampled} + Q_{in} = Q_{out} \quad (2.16)$$

which, as established earlier (2.3) when introducing the pressure driven Poiseuille flow, can be further expressed:

$$\frac{P_{ext} - P_T}{R_2} + \frac{P_{in} - P_T}{R_1} = \frac{P_T - P_{out}}{R_1} \quad (2.17)$$

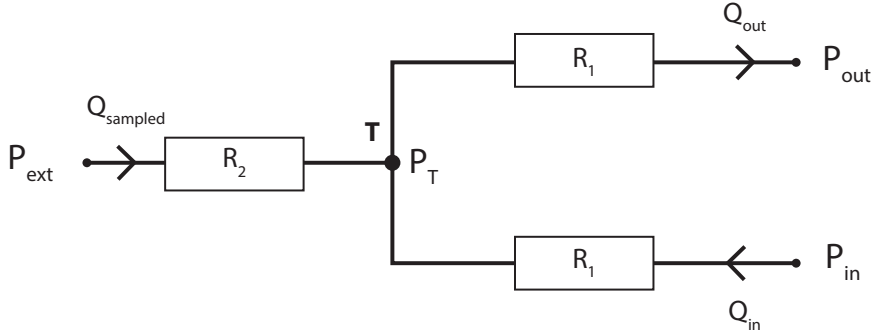


**Figure 2.15** Probe microfluidic equivalent model. In this system  $P_T$ ,  $P_{ext}$ ,  $P_{in}$  and  $P_{out}$  are the pressures,  $R_1$  and  $R_2$  are the fluidic resistances whereas  $Q_{in}$ ,  $Q_{out}$  and  $Q_{sampled}$  are the flows while **T** is the microchannels intersection.

This equation can be solved for  $P_T$  and, consecutively, the flows are expressed by:

$$Q_{sampled} = \frac{P_{ext}}{R_2} - \frac{R_1 P_{ext} + R_2 (P_{in} + P_{out})}{2R_2^2 + R_1 R_2} \quad (2.18)$$

$$Q_{in} = \frac{P_{in}}{R_1} - \frac{R_1 P_{ext} + R_2 (P_{in} + P_{out})}{R_1^2 + 2R_1 R_2} \quad (2.19)$$

$$Q_{out} = \frac{R_1 P_{ext} + R_2 (P_{in} + P_{out})}{R_1^2 + 2R_1 R_2} - \frac{P_{out}}{R_1} \quad (2.20)$$

Figure 2.16 (a) shows the linear relationship between the collected flow  $Q_{sampled}$  and a pressure difference  $\Delta P$  applied between  $P_{in}$  and  $P_{out}$ ,  $P_{in}$  being fixed at an arbitrary value of + 10 mbar relative to a pressure reference  $P_{ref}$ .  $P_{ext}$  equals  $P_{ref}$ , the local pressure, fixed at 1013.25 mbar (standard pressure at mean sea level) whereas the microchannel width ( $w$ ) and height ( $h$ ) accounts for  $80 \mu\text{m}$  and  $40 \mu\text{m}$ , respectively. One may note the external fluid can be collected only when  $\Delta P > 10$  mbar, as expected.

The impact of a pressure variation occurring in the implanted medium on the sampling process may also be evaluated with this model. Figure 2.16 (b) displays

## 2.5. Neural Probe - Microfluidic Model

---

the  $Q_{\text{sampled}}$  variation function of a  $P_{\text{ext}}$  for constant condition at the probe entries;  $P_{\text{in}} = P_{\text{ref}} + 10 \text{ mbar}$  and  $P_{\text{out}} = P_{\text{ref}} - 40 \text{ mbar}$  (meaning  $\Delta P = 50 \text{ mbar}$ ) where  $P_{\text{ref}}$  still equals  $1013.25 \text{ mbar}$ . We can extract from this graph the sensitivity to an external change of pressure  $S = 0.20 \text{ nLs}^{-1} \text{ mbar}^{-1}$  which is rather large. In *in vivo* conditions,  $P_{\text{ref}}$  should remain constant and should not disturb the sampling process though. The intracranial pressure in humans is slightly higher than the local pressure and remains stable over time; standard values range between  $+ 9.3$  to  $+ 20 \text{ mbar}$  ( $= + 7$  to  $+ 15 \text{ mmHg}$ ) (Czosnyka et al. 2004; Chapman et al. 1990).

The third plot in figure 2.16 (c) assesses the impact of the fluidic resistance  $R_2$  increase which may be a situation occurring if tissues gets inside the probe and clog the sampling inlet. The system conditions have been fixed to  $P_{\text{in}} = P_{\text{ref}} + 10 \text{ mbar}$  and  $P_{\text{out}} = P_{\text{ref}} - 40 \text{ mbar}$ ,  $P_{\text{ref}} = P_{\text{ext}} = 1013.25 \text{ mbar}$  and the microchannel width-to-height ratio to  $\frac{w}{h} = 2$ . Interestingly we observe the system is relatively resilient against clogging;  $Q_{\text{sampled}}$  starts dropping significantly only when the channel section reaches a half of the initial area  $A_0$  ( $A_0 = 40 \mu\text{m} \times 80 \mu\text{m}$ ).

In the precedent description, we did not take into account that the upper microchannel was a biphasic droplet segmented flow. The modeling of a two-phase flow is substantially more complex than a single-phase flow. Indeed, new elements must be included in the description such as the contribution of interfaces between the two phases as well as the capillary effects with the microchannel walls. Let's consider such a situation where a carrier fluid, the PFD imiscible phase, transports the aqueous droplet collected from the tissues. We also make here the reasonable hypothesis the droplet radius is larger than the channel length scale, which means the droplet occupies most of the channel cross section and is therefore flattened in the channel. A non-trivial description of the total pressure drop along the channel can be written (Bretherton 1961; Wong et al. 1995; Fuerstman et al. 2007):

$$\Delta P = \Delta P_{PFD} + \Delta P_{drop} + \Delta P_{caps} \quad (2.21)$$

## Chapter 2. Neural Probe - Design and Development

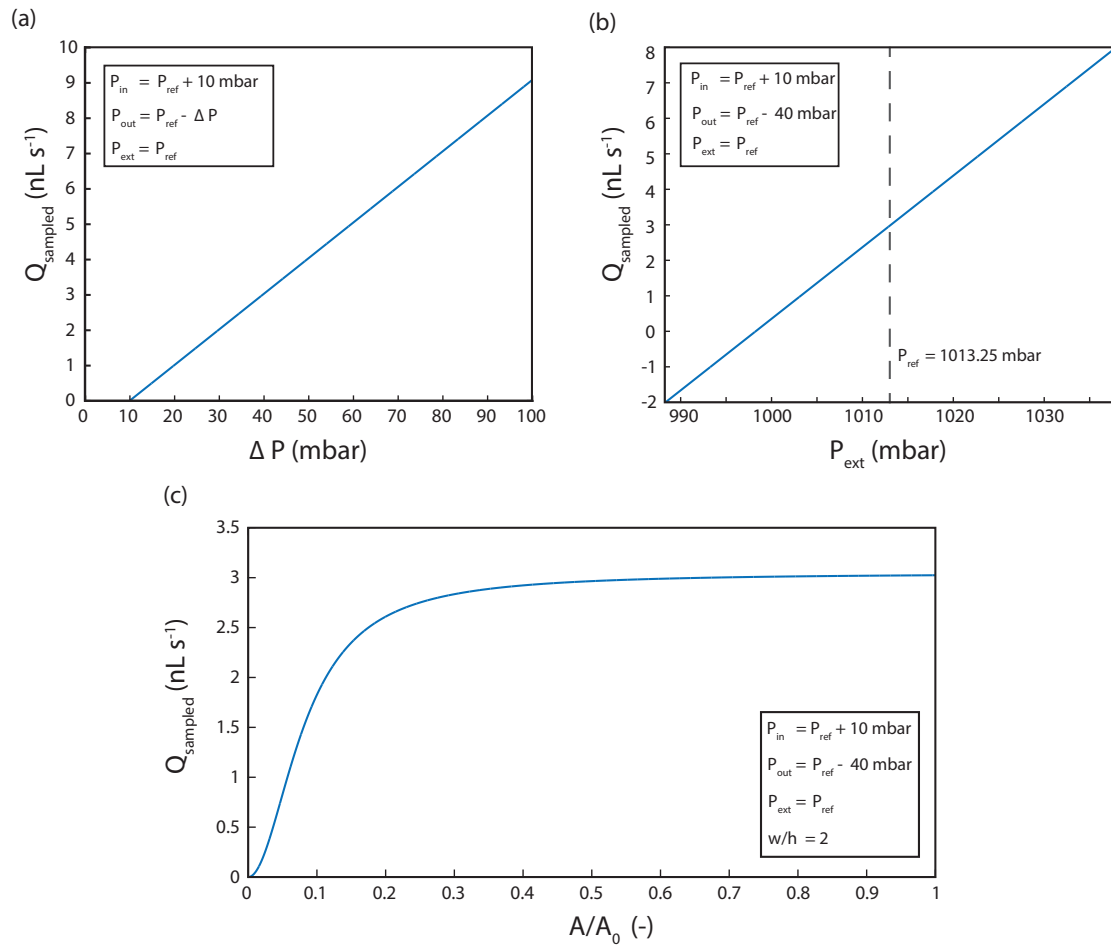


**Figure 2.16** Model-based prediction of the neural probe microfluidic behaviour with different parameter variations. The model parameters fixed for each plot are given in the legend of each graph. All model pressure entries are relative to a reference pressure  $P_{\text{ref}} = 1013.25 \text{ mbar}$ . (a)  $Q_{\text{sampled}}$  dependence over  $\Delta P$ , a pressure difference applied between  $P_{\text{in}}$  and  $P_{\text{out}}$ ,  $P_{\text{in}}$  being fixed to a pressure of  $P_{\text{ref}} + 10 \text{ mbar}$ . (b)  $Q_{\text{sampled}}$  plot function of the local variation of  $P_{\text{ext}}$ . (c)  $Q_{\text{sampled}}$  resilience over the increase of the fluidic resistance  $R_2$  consecutive to a cross section change.  $A_0$  is the initial area of the cross section where the width ( $w$ ) to height ( $h$ ) ratio is maintained constant;  $w/h = 2$ .

where we distinguish three contributing terms  $\Delta P_{\text{PFD}}$  the pressure drop in the carrier fluid,  $\Delta P_{\text{drop}}$  the pressure drop in the aqueous droplet and  $\Delta P_{\text{caps}}$  the pressure drop at the front and rear ends, or caps, of each droplet.

The formulation for  $\Delta P_{\text{caps}}$  was first proposed by Bertherton for a circular cross section channel and adapted to a rectangular cross section by Wong *et al.* (Bertherton 1961; Wong *et al.* 1995). The pressure contribution of the droplets caps is the

## 2.5. Neural Probe - Microfluidic Model

consequence of the asymmetrical deformation of the front interface (flattening) compared to the rear (elongating) due to the droplet displacement in the carrier fluid (Bretherton 1961). Figure 2.17 provides a qualitative plot of the pressure drop contributing terms in such a flow for viscous droplets (in our condition,  $\lambda = \frac{\mu_{drop}}{\mu_{PFD}} = \frac{8.9e-4 \text{ (Pa s)}}{6.4e-3 \text{ (Pa s)}} = 0.14 \Rightarrow \lambda \sim 1$ ) (adapted from Baroud et al. 2010).

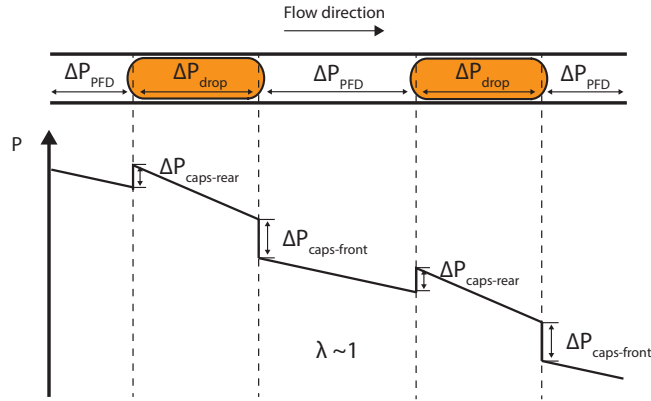


**Figure 2.17** Qualitative plot of the pressure variation along a microchannel filled with viscous droplets carried by an imiscible PFD phase.  $\lambda = \frac{\mu_{drop}}{\mu_{PFD}}$ . (adapted from Baroud et al. 2010)

The equation 2.21 can be written:

$$\Delta P = R_h \cdot Q_{PFD} + R_h \cdot Q_{drop} + n \cdot c_{lambda} \frac{\gamma}{H} Ca_d^{2/3} \quad (2.22)$$

where  $R_h$  is the fluidic resistance,  $Ca_d = \frac{\mu U}{\gamma}$  the dimensionless capillary number ( $U$  = the fluid velocity,  $\gamma$  = the surface tension),  $c_{lambda}$  a dimensionless parameter that depends on  $\lambda$  and on the geometry<sup>3</sup> and  $n$  the number of droplets. We distinguish the two linear contributions from the fluid inside the droplets and from the outside (= PFD carrier fluid). The only non linear term comes from the droplets caps contribution at the interface PFD/droplet whose pressure jumps scales as  $Ca_d^{(2/3)}$  and takes discrete values as it depends on the number of droplets  $n$  in the upper channel. We can quantitatively compare the contribution of the term  $\Delta P_{caps}$  to the other pressure drop contributions. For instance, for a flow of viscous water droplets ( $\lambda = 0.00089 \text{ Pas}$ ) transported at a velocity of  $3 \text{ mm s}^{-1}$  in

<sup>3</sup>explicited in (Wong et al. 1995)

a carrier fluid of viscosity  $\lambda = 0.0064$  Pas flowing through a rectangular channel of width  $W = 80 \mu\text{m}$  and height of  $40 \mu\text{m}$  with an interfacial tension between the PFD and the water of  $\gamma = 3.5 \times 10^{-2} \text{ Nm}^{-1}$  (Peters et al. 2013), we find  $\Delta P_{\text{caps}} = 0.0992$  mbar per droplet which is not negligible since up to 75 droplets (droplet length of 300 nL considered) can fill the channel during sampling. It could therefore be interesting to extend the precedent single phase flow model to a biphasic flow model in order to predict the behavior of the neural probe microfluidic system more accurately. In the scope of this thesis though, we will limit our description to the single phase flow model which gives a good first approximation of the neural probe microfluidic network behavior.

## 2.6 Conclusions

In this chapter we went through the theoretical basics useful for the design and development of micro-scale devices which include electrical and fluidic components. The main requirements for the development of the neural probe were defined. Among these requirements the biocompatibility remained one of the major point. In order to minimize the impact of the device *in vivo*, microfabrication methods were employed and allowed to reduce the dimensions of the probe and integrate the following elements in close proximity to each other:

- A droplet generation mechanism connected to a monolithically integrated microfluidic channels
- Microelectrodes for stimulation and recording

The microfabrication process proposed enabled to produce the devices with a yield reaching 85 %. A fluidic model of the probe enabling the prediction of the behavior of the system under defined conditions was proposed as well. The next chapter will address the testing of the probe functional testing prior to performing *in vivo* experimentation.

# Chapter 3

## Neural Probe - Functional Validation

### 3.1 Introduction

In this chapter is addressed the functional validation of the neural probe main functions. Characterization tests are performed regarding the device mechanical, electrical and fluidic properties. In particular, the mechanical probe strength is assessed and its ability to be inserted in the neural tissues tested. The electro-chemical behavior of the probe microelectrodes is assessed as well. Finally, the droplet collection mechanism is evaluated for the monitoring of a rapid molecular change occurring in a controlled medium, as it can be the case in the neural tissues. It is worth mentioning that this chapter is partly inspired from a scientific article recently published by the author (Petit-Pierre et al. 2016).

### 3.2 Mechanical Characterization

#### 3.2.1 Penetration Test

Traditionally, neural interfaces have been constructed with little regards to their mechanical properties. For instance, silicon-based neural recording systems

### Chapter 3. Neural Probe - Functional Validation

---

have been widely used and function as good electrical interfaces. But their material stiffness creates an important mismatch with the viscous neural tissues environment (B. Lee et al. 2005). According to the requirements defined at the beginning of chapter 2 (table 2.1) the neural probe mechanical strength must be sufficient to ensure its integrity during surgical handling and device operation. Microfabrication yield after process optimization has been showed to be relatively high (85 %) which ensures a good device finish and mechanical integrity. Apart from manipulation, the neural probe must remain stiff during penetration in the brain tissues which represents one of the major mechanical stress the shank is subjected to. Due to the device small dimensions and the low materials Young's modulus ( $E_{SU-8} = 2.0 \text{ GPa}$ ), the neural probe is flexible as it is shown in figure 3.1. It can be bent without structural damage at a radius of roughly 6.5 mm. As introduced in chapter 1 flexible polymer materials are advantageous since they are better accepted in the brain tissues than rigid silicon-based neural probe (Rousche et al. 2001; Mercanzini, Colin, et al. 2009). In particular they are less prone to tissues damage following micro-motion occurring between the brain and the probe (B. Lee et al. 2005). However this property does not serve the implantation process as the probe structural stiffness must be high enough not to brake or buckle during penetration in the tissues. In order to assess the

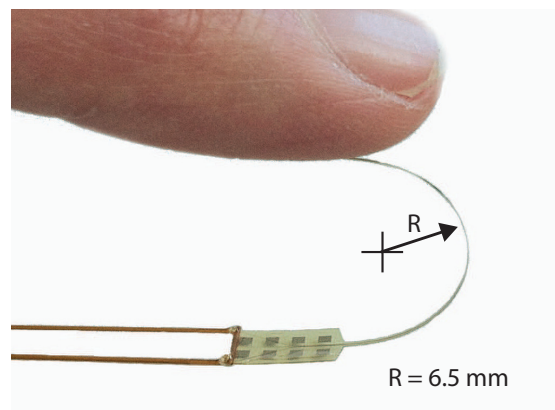


**Figure 3.1** Neural probe flexibility during a qualitative bending test. The probe can be bent at a radius of  $r = 6.5 \text{ mm}$  without any impact on its mechanical integrity.

probe ability to enter the brain tissues, penetration tests were performed in brain phantoms. Brain phantoms act as mechanically equivalent media simulating cerebral tissues mechanical properties. Two different phantoms were prepared; a



### 3.2. Mechanical Characterization

2.2 % agarose gel and a gelatine solution prepared from commercially available product (gelatine sheet). Figure 3.2 (a) shows an equivalent model of the experiment in which a vertical displacement of magnitude  $d$  (oriented towards the  $z$  axis) is applied to the probe and the resulting  $F_{ph}$ , the reaction force of the brain phantom is monitored. The experimental setup consisted in a  $z$ -axis linear stage (vertical motion), two brain phantoms prepared in transparent cups, a neural probe and a precision lab scale (Ohaus Pioneer 210GX). The neural probe mounted on the linear stage (not visible) after insertion in the brain phantom placed on the lab scale is showed in figure 3.2 (b). The reaction force

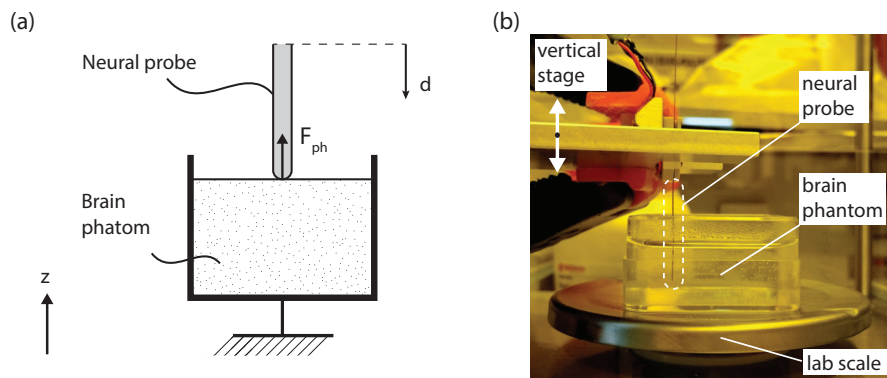


**Figure 3.2** (a) Model of the penetration test performed. The neural probe is vertically displaced along the  $z$  axis until penetration in the brain phantom over a distance  $d$ . The maximum force reached along the course of displacement is recorded. (b) Experimental setup. Brain phantom were prepared and placed in transparent cup over a lab scale. The neural probe was mounted on a  $z$ -axis stage (vertical displacement) and implanted in the brain phantom until a penetration depth of 8 mm was reached while recording the force

$F_{ph}$  exerted by the medium over the probe was recorded along a translation of  $d = 8 \text{ mm}$  performed at a velocity of roughly  $1 \text{ mms}^{-1}$ . Each experiment was repeated 3 times on the two brain phantoms. Maximum force during insertion in the agarose gel reached  $6.21 \pm 0.48 \text{ mN}$  while in the gelatine it reached  $3.50 \pm 0.98 \text{ mN}$ . In every experiment the neural probe remained vertical and didn't show any buckling behaviour. A recent study about the mechanical properties of mouse brain during penetration of neural probe reported a maximum force reached upon shank insertion in the cortex to be in the range of 2.5 mN (probe diameter  $d = 200 \mu\text{m}$ , insertion speed  $0.8 \text{ mms}^{-1}$ ) (Sharp et al. 2009). As indicated in figure 3.3, the results obtained with our experiment are both of higher magnitude than

## Chapter 3. Neural Probe - Functional Validation

---

this value obtained *in vivo*. In particular, the probe was submitted to a force twice larger when tested against penetration in the 2.2 % agar gel (brain phantom 1). As a result, it is expected the probe insertion in the rodent brain should not cause any issue.

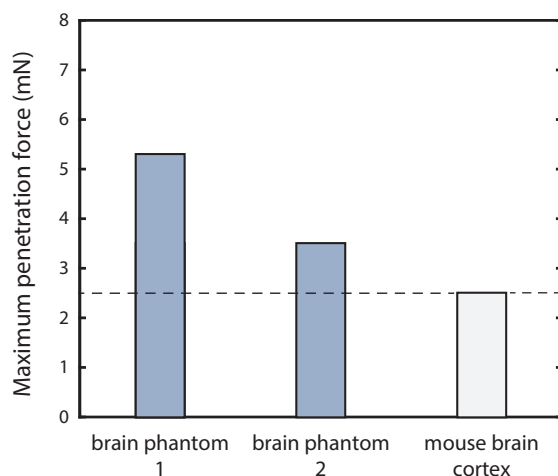


**Figure 3.3** Maximum force reached during penetration tests in brain phantom 1 (agarose gel 2.2 %) and 2 (gelatine). The results obtained are compared to the *in vivo* maximum insertion force reported for mouse brain cortex penetration with a probe of similar geometry. In both phantoms, the neural probes withstand the test perfectly, the probe trajectory remained vertical and no buckling occurred.

## 3.3 Electrical Characterization

### 3.3.1 Impedance Spectroscopy

In a first approach, the electrochemical behaviour of the electrode/electrolyte interface was examined using impedance spectroscopy compared with a silver/silver-chloride reference electrode (Ag/AgCl). The measurements were conducted using a commercially available impedance analysis system (Agilent 4294A, Agilent technologies). Impedance modulus and phase were recorded at discrete frequencies in the 100 Hz to 5 MHz range. The probe and the counter electrode were immersed in a saline solution (0.9 % NaCl pH 7.0,  $\rho = 16 \text{ mS cm}^{-1}$ ) and the impedance

spectroscopy performed at an oscillation amplitude of 50 mV.

The electrode-electrolyte behaviour was approximated by an equivalent circuit including a resistive and capacitive element as introduced in chapter 2.1.3 (Mercanzini, Colin, et al. 2009; Altuna, Menendez de la Prida, et al. 2012). Figure 3.4 (a) introduces the equivalent electrical circuit of this situation. The interfacial capacitance is here approximated by a constant phase element (CPE) which best describes the double layer behaviour at the interface with the solution. We also considered a charge transfer resistance ( $R_{CT}$ ), an element which models the resistance to the charge transfer process taking place at the electrode surface. The CPE and the  $R_{CT}$  assembled in parallel are combined in series with a spreading resistance ( $R_s$ ) and a bulk resistance ( $R_{bulk}$ ) as shown in figure 3.4 (a). Finally, the probe dielectric insulation is modeled by a capacitance ( $C_{dielectric}$ ) in parallel to these previous elements. Figure 3.4 (b) and (c) show a typical impedance/phase spectrum for the recording electrode ( $D = 20\mu\text{m}$ ) and the stimulation electrode ( $D = 150\mu\text{m}$ ), respectively. The spectra obtained are in accordance with similar devices previously characterized with the same method (Merrill et al. 2005; Mercanzini, Cheung, et al. 2007; Bédurier et al. 2015). Using the Peak Resistance Frequency method (PRF), we observe a difference of one order of magnitude between the spreading resistance of the  $20\mu\text{m}$  electrode ( $R_s = 2.0 \times 10^4 \Omega$ ) and the  $150\mu\text{m}$  ( $R_s = 3.1 \times 10^3 \Omega$ ) when the phase is closest to zero (Mercanzini, Colin, et al. 2009). This gap is explained by the difference in size of the electrode ( $20\mu\text{m}$  vs.  $150\mu\text{m}$ ), the spreading resistance being inversely proportional to the diameter of the circular electrode (Newman 1966). Additionally, the electrical resistance of each track was measured with a 4 points probe station (SüssMicrotec, PM8). The measurements were performed track by track, between the proximal contact and the corresponding electrode at the distal tip (see figure 2.12). Contacting the electrodes integrated in the microfluidic channels required the delamination of the bottom SU-8 layer in order to access the conductive metal layer. Each electrode was successfully connected and the track electrical resistance ranged from  $652 \Omega$  to  $781 \Omega$  (longer tracks are slightly more resistive). Compared to the values found for  $R_s$  using the PRF method, the contribution of the tracks electrical resistance will only slightly affect the system since the values are at least 4 times smaller.

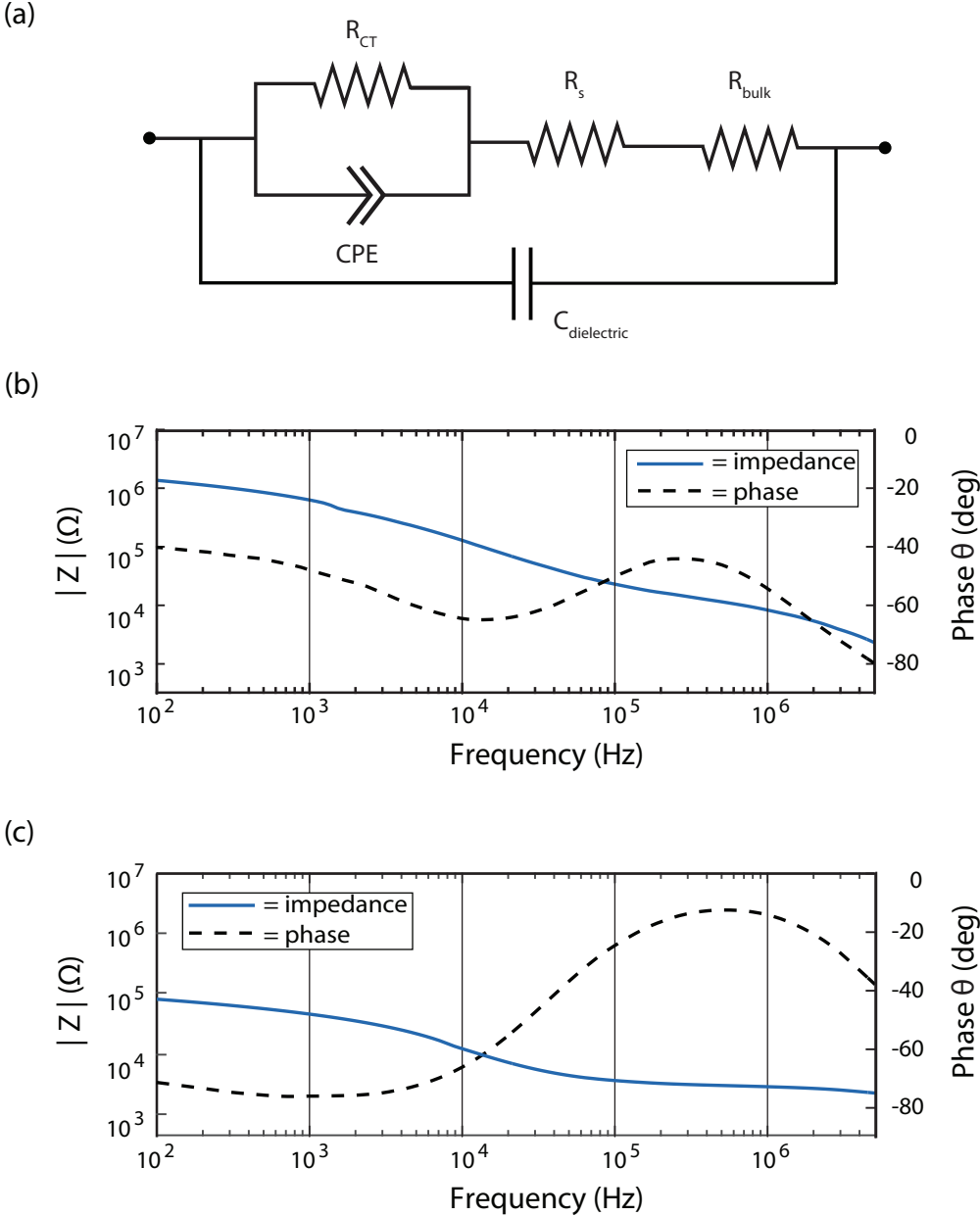


**Figure 3.4** (a) Equivalent electrical model for an electrode-electrolyte interface. (b) Impedance magnitude and phase for a  $20\ \mu\text{m}$  recording electrode (c) and a  $150\ \mu\text{m}$  stimulation electrode.

## 3.4 Fluidic Characterization

### 3.4.1 Droplet Generation - Demonstration

The T-junction included at the distal tip of the probe acts as a droplet generation system and is a crucial element of the technology developed in this work. The droplet generation process is controlled by modulating the flow of the PFD carrier phase which circulates in the microchannels of the probe. The PFD is injected in the proximal fluidic inlet, circulates toward the distal tip and returns to be re-collected in the proximal fluidic outlet. In order to connect the probe with the fluidic driving control, fused silica capillaries (ID =  $250\ \mu\text{m}$ , OD =  $360\ \mu\text{m}$ ) were bonded to the probe legs. The capillary were chosen large enough to be introduced over the probe legs. They were assembled with epoxy glue according to figure 3.5 in order to ensure a liquid-tight and pressure-resistant connection. Each capillary (length = 40 cm) is connected to a pressure-driven reservoir filled

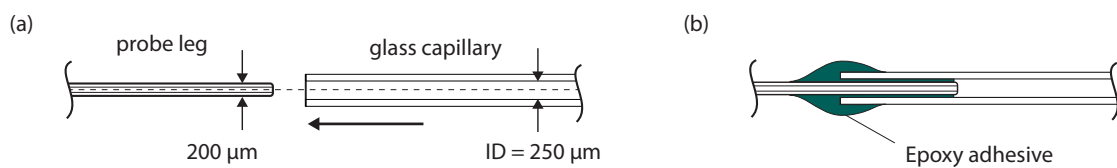


**Figure 3.5** Drawing of the solution implemented to ensure a watertight connection between the neural probe proximal inlet/outlet (probe leg) and the fused silica capillaries. (a) The capillary is big enough to be inserted over the probe leg. (b) Tight bonding is performed using epoxy adhesive.

with PFD and controlled by a pressure driving unit (Fluigent, module MFCS-MZ). This system enables to apply a positive or negative pressure at the probe proximal inlet/outlet with respect to the ambient pressure. As introduced in chapter 2.5, the fluidic behaviour of the probe can be modelled by a 3 entries system linked by the T-junction (included in the probe distal tip).  $Q_{\text{in}}$  and  $Q_{\text{out}}$  are the flow resulting from the pressure applied on each microchannel of the probe.  $Q_{\text{sampled}}$  is the extracted flow from the sampling inlet. A droplet generation triggered by the actuation of  $P_{\text{in}}$  and  $P_{\text{out}}$  is possible when the following conditions are met

## Chapter 3. Neural Probe - Functional Validation

---

(see equation 2.16 in chapter 2.5):

$$P_{in} > P_{ext} > P_{out} \quad (3.1)$$

where  $P_{ext}$  is the pressure at the probe distal sampling inlet. Figure 3.7 shows a sequence in which a droplet is generated. In order to obtain this result a dedicated setup was designed allowing to collect clear water in the PFD carrier phase while focusing on the probe distal tip with a camera (IDS, uEye UI-1240SE) as represented on figure 3.6. The top layer of the neural probe is made out of a  $6\ \mu\text{m}$  thick PI substrate providing a direct optical access to the microchannels. Figure 3.7 demonstrates the generation of a water droplet included in the PFD carrier fluid. At  $t = 0\ \text{s}$ , the droplet is in preparation and still attached to the sampling inlet, at  $t = 0.126\ \text{s}$  the droplet detaches and then propagates along the channel. At the end of the sequence we notice that the next droplet is already in preparation. For this demonstration, a constant pressure difference between  $P_{out}$  and  $P_{in}$  of  $\Delta P = 50\ \text{mbar}$  was applied. This enabled to generate droplets of  $0.62\ \text{nL}$  at a frequency of  $0.13\ \text{Hz}$ . Higher frequencies can be obtained by increasing  $\Delta P$ .

### 3.4.2 High Frequency Droplet Sampling

In the last experiment it was demonstrated how the droplet collection process occurs in standard conditions. In this section we demonstrate the probe ability to capture a rapid molecular composition change with its high frequency droplet sampling mechanism.

#### 3.4.2.1 Experimental Setup.

In this experiment, two syringes filled with blue-colored water and clear water are both connected to the same tube, called in the following the shared tube (Saint-Gobain, Tygon, ID=0.51 mm, OD=1.52 mm). They are operated independently by 2 syringe-pumps (Cetoni, Nemesys) and are employed in order to generate an optically detectable molecular composition change in the shared tube. A neural

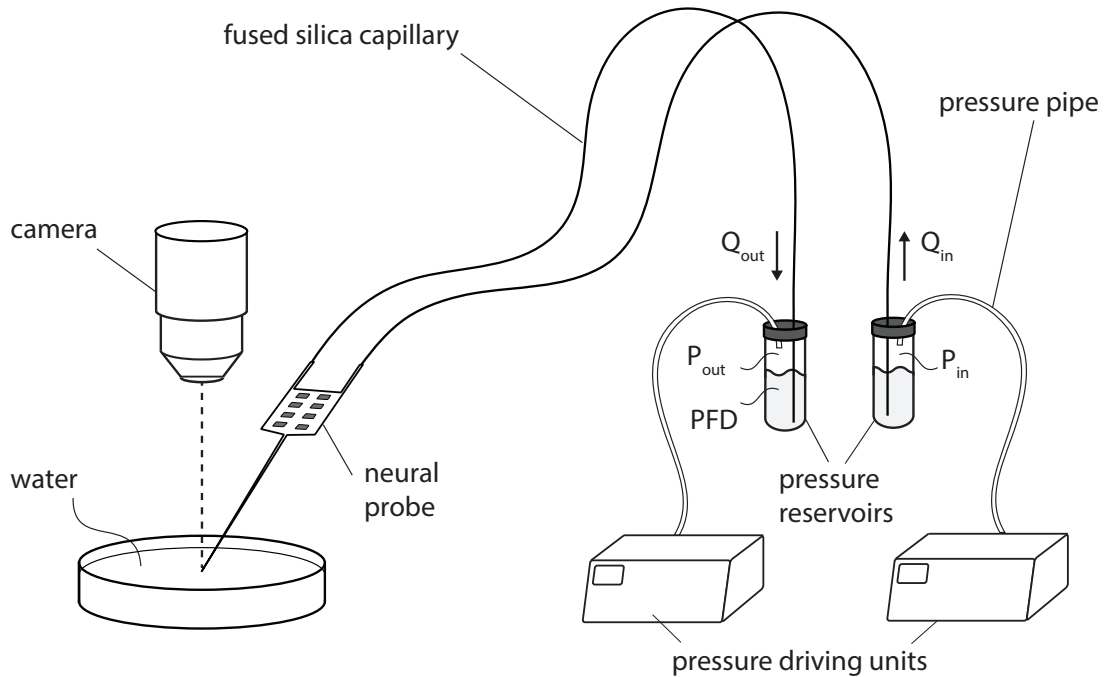


**Figure 3.6** Experimental setup for the testing of the droplet generation process. The neural probe is actuated by two pressure driving units which generate a fluid motion through the capillaries and towards the probe microchannels. With this setup, water droplets separated by PFD phase are generated while the process is recorded with an optical camera.

probe is inserted in the same tube. It is operated by two pressure-pumps, as in the precedent setup, and actuated in order to continuously collect droplets of the water circulating in the shared tube. A first measurement of the mean light intensity through the tube, before the sampling spot, is performed with a photodiode (Vishay, model BPW34) and an amplifier (Stanford Research System, SR570). A second measurement of the mean light intensity, focused on the passing droplet on the microchannel of the probe, is performed with a microscope (Zeiss, Axiowert S100 TV). The signal is recorded using a camera (IDS, uEye UI-3600CP) and the mean light intensity of images computed using the software ImageJ. A representation of this experimental setup can be seen in figure 3.8 (a).

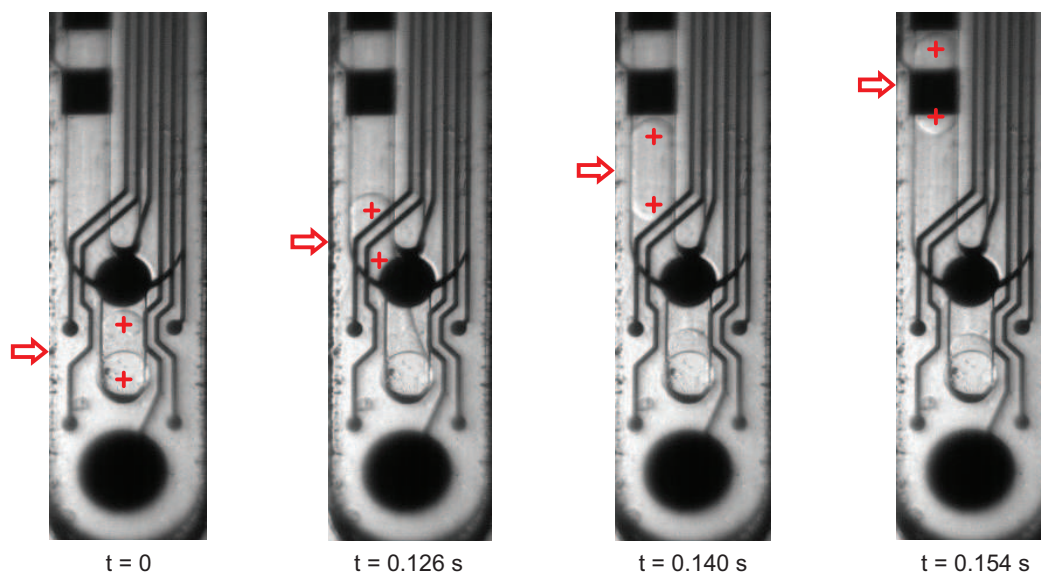


**Figure 3.7** Sequence of a water droplet generated in a PFD carrier phase occurring at the T-junction. At  $t=0$ , the droplet (volume = 0.62 nL) is in preparation. The droplet detaches ( $t=0.126$  s) and propagates along the microchannel (from  $t=0.140$  s to  $t=0.154$  s). The red crosses underline the beginning and the end of the droplet.

### 3.4.2.2 Experimental Conditions

A fast transition from clear water to blue water was generated in the tube. In order to obtain this effect, the tube was first filled with clear water and flushed during 5 s at a flow rate of  $10 \mu\text{Ls}^{-1}$  using the syringe pumps. Then, the clear water syringe pump was switched off. The droplet sampling process was started by modulating the pressure applied to the PFD circuit connected to the probe. A pressure of  $P_{\text{in}} = 50$  mbar and  $P_{\text{out}} = -400$  mbar was applied (relatively to the local pressure). Then, the flow of blue dyed water from the second syringe pump was turned on at a value of  $10 \mu\text{Ls}^{-1}$ . This resulted in the generation of a fast color change in the tube recorded both before the sampling spot (A), via the photodiode, and after the sampling spot (B) with a camera focused on the droplets passing in the probe, as illustrated in figure 3.8 (b). When the mean light intensity measurement was stabilized in both spots (A and B) the recording was stopped.



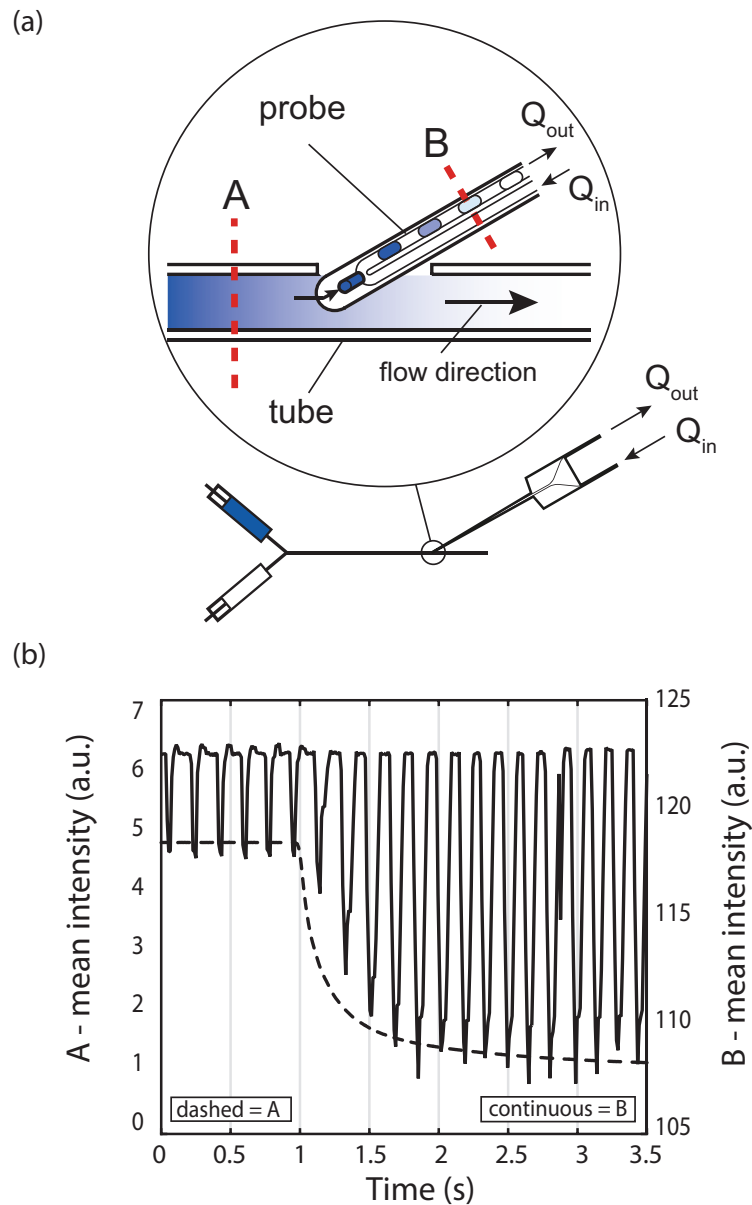


**Figure 3.8** (a) Representation of the setup designed in order to validate the effectiveness of the droplet sampling mechanism. (b) Mean intensity measured at position A, before the sampling spot and at position B, on the passing droplets. Strong temporal correlation between both measurements is demonstrated.

### 3.4.2.3 Results

Under these conditions, fast color changes were generated and captured within the sampling system of the probe. In the bottom of figure 3.8, the concentration

## Chapter 3. Neural Probe - Functional Validation

---

change measured at the location A (dashed line) and B (continuous line) is shown. On measurement A (located before the sampling spot) we can note a fast decrease of intensity starting at time  $t = 1$  s that stabilizes after 2.5 s. The major part of this transition occurs in 1.5 s. On measurement B, the light intensity through the probe microchannel is presented. Each peak corresponds to a passing droplet thus demonstrating a fast collection frequency of 6 Hz. Under these conditions, the mean volume of a droplet was 0.84 nL. The level at which the signal returns after every droplet passes corresponds to the signal intensity of the PFD phase. A strong correlation regarding the time at which the change occurs and the shape of the curves is demonstrated on measurement A and B. This suggests that the droplet sampling mechanism included in the neural probe is able to thoroughly capture a rapid change of concentration occurring in the external liquid flowing in the shared tube.

### 3.5 Discussion

Achieving high temporal resolution during *in vivo* sampling in brain tissues is a challenge since neurotransmitters release typically occurs in the range of the second (Venton et al. 2006; Rossel et al. 2003). The maximum achieved sampling rate of this device was 6 Hz (meaning a droplet every 170 ms). It indicates we should be able to capture in real time a concentration change of a neurotransmitter occurring in the brain with this tool. One of the main limitation to this approach relates to the maximum volume of interstitial liquid we can remove from the tissue without causing any damage. Since the volume of each droplet is 0.84 nL, it represents, at a frequency of 6 Hz, a removal of an equivalent constant flow reaching  $302 \text{ nLmin}^{-1}$ . The impact of direct sampling in the neural tissue was demonstrated to be minimized when the flow rate was kept under  $50 \text{ nLmin}^{-1}$  and the total volume removed under  $2.5 \mu\text{L}$  (Kennedy et al. 2002). Our approach could deplete quickly the medium since the probe flow rate is 6 times higher than  $50 \text{ nLmin}^{-1}$ . However, the effect of depletion can be strongly limited by performing the sampling during short periods of time typically during 1 minute or less which would be fully compatible with our approach. In this

situation and with the parameters cited above ( $302 \text{ nLmin}^{-1}$  during 1 min), the total volume removed is 302 nL which seems acceptable. We can even imagine to generate single droplets "on-demand" with fast burst of pressure. Another approach for limiting the depletion would be to replace the liquid removed by an equivalent volume of physiological solution injected at the same spot. It could easily be implemented by adding a microfluidic channel on the probe dedicated to this function.

Regarding the time resolution, there are good chances to further increase the sampling rate by driving the system at a superior difference of pressure between the entries. This will result in the reduction of the space between droplets (PFD segment volume) and the increase of the droplets volume as supported by Gupta *et al.* (Gupta et al. 2009). Increasing the volume of the droplets is a benefit regarding the analysis of the samples. A limitation can however be related to the actuation system which must be fast and compatible with high pressure controls. Admitting that such equipment is available, special care will be needed to reinforce the fluidic connections within the neural probe. In preliminary tests, the neural probe was connected to syringe pumps that could operate the system at high flow rate. In this configuration, fluidic connection failures were observed when the flow rate reached a value above  $1 \mu\text{L}/\text{sec}$ , meaning a pressure in the range of 1.5 bar (with our geometry).

Now that the sampling process has been proven to be functional, one may define an analysis method compatible with the sample configurations (droplet train). Most detection methods require a minimal sample volume and are characterized by a maximum achievable sensitivity (Kennedy 2013). High-Pressure Liquid Chromatography (HPLC) coupled to electrochemical or fluorescence detection would have been good candidates but are incompatible with the current volume of the droplets ( $V = 0.84 \text{ nL}$ ). It is too small compared to the typical  $10 \mu\text{L}$  to  $20 \mu\text{L}$  injected sample volumes (Zapata et al. 2009). Electrospray Ionisation (ESI)-MS has also been proposed as a compatible method for analyzing samples segmented in droplets (T. R. Slaney et al. 2011). However this method would require the addition of a reagent of identical volume in each droplet before analysis which is certainly very challenging to control. Another method achieving high

## Chapter 3. Neural Probe - Functional Validation

---

sensitivity with low sample volume (pL to nL) is Capillary Electrophoresis (CE) combined with Laser Induced Fluorescence (LIF). This would require further developments in order to sort and manipulate the droplets of interest while still controlling their sequence. Droplet segmentation guarantees the temporal resolution of the measurement. However, a limit to this approach is that it renders difficult the interface with existing analysis methods. Indeed, during the analysis, droplets cross-contamination must be avoided whereas droplets order must be maintained to keep a consistent sampling time-history. The PFD phase may also clog the analytic equipment quickly (such as a HPLC column). The solution to this challenge will certainly consist in associating to the analysis a specific and tailor-made sample preparation platform compatible both with the droplet train and the detection equipment.

### 3.6 Conclusions

In this chapter were assessed the main functions of the neural probe with regards to the future *in vivo* application of the technology. The device combines, in one single tip, recording and stimulation electrodes with a micro-scale droplet generator. In particular, the mechanical property of the probe and its ability to be implanted in the brain tissues was assessed. The tests performed showed that:

- The probe stiffness is high enough and withstand almost twice the compression stress reached during insertion in mouse cerebral cortex

The electrochemical behaviour of the microelectrodes was tested in a saline solution (0.9 % NaCl pH 7.0). The impedance spectra recorded showed that:

- The electrode-electrolite interaction behaviour is similar to equivalent device proposed in the literature
- The stimulation electrodes will affect a larger tissue volume than the recording electrodes.

### 3.6. Conclusions

---

The probe's fluidic functions were assessed as well. The probe has been proven to efficiently reconstitutes a rapid (1.5 ms) molecular change occurring in a controlled medium in which droplet collection was continuously performed:

- The sampling temporal resolution reached a frequency of 6 Hz (one droplet every 170 ms) which is compatible with the time-range of fast synaptic signal exchanges.

The neural probe efficiently answers the requirements regarding mechanical integrity, electrical and fluidic performances while providing high spatial and temporal resolution.



# Chapter 4

## *In Vivo* Neurochemical Sampling

In this chapter is addressed the first *in vivo* testing of the neural probe and an associated analysis method. The probe has been implanted in rat brains as part of a pilot animal study in order to demonstrate the validity of the proposed approach in real conditions. In parallel, a dedicated surface-based MS detection method providing an efficient way of analyzing the collected samples organized in a droplet-train was developed and tested. The results of the *in vivo* trial as well as the results of the detection are reported. It is worth mentioning this chapter content is inspired from a scientific article recently submitted for publication by the author of this manuscript.

### 4.1 Introduction - Droplet Detection Methods

The neural probe allows to collect with high resolution (under the second) droplets separated by an oil phase. This method allows to maintain the temporal resolution as defined by the lapse of time between the generation of two droplets. When applied to brain micro-sampling, the main challenge of this approach remains the analysis of the samples confined in low-volume, low-concentrated and non-purified samples surrounded by non-aqueous carrier phase. As the neural probe functions has been thoroughly discussed in the precedent chapters, this

## Chapter 4. *In Vivo* Neurochemical Sampling

---

introduction addresses in details the droplet detection methods. Droplet analytical platforms are an important element which contributed to the development of the field of droplet microfluidics. A large number of techniques for droplet contents analysis have been proposed (Gu et al. 2014). Here we will concentrate on the most promising ones with respect to our application.

Fluorescence detection is an optical method based on the analysis of the light emission of an atom or molecule which previously absorbed light or an electromagnetic radiation. This process is consecutive to the increase of the molecule energy state by an incoming excitation light followed by a return to a normal energy level during which the fluorescent emission occurs at a wavelength longer than the exciting one. The method is useful for the detection and quantitative measurements of analytes concentration. The application of this technique includes fluorescence monitoring of reverse transcription of Polymerase Chain Reaction (PCR) within agarose droplets or enzyme kinetic measurements in droplets formed out of a fluorescein concentration gradient (Zhang et al. 2012; Bui et al. 2011). A promising application of the technology was proposed in a study about a microfluidic device for fast immunoassay detection based on a fluorescent detection (chip-integrated) which monitors a droplet bi-phasic flow. The device enabled highly sensitive detection (14 pmol sensitivity) of congenital hypothyroidism (TSH hormone), a frequent occurring disease of the newborns (1:3000 to 1:4000) (Ali-Cherif et al. 2012). The limit to fluorescent detection remains that a fluorescent label must, in most cases, be bound to the molecule of interest which may be an issue. Indeed the process of adding this label involves complex droplet manipulation and implies that the label is existing, which is often not the case.

Electrochemical detection has also been proposed as an effective method for the analysis of droplets content. The technique is based on the detection of the oxidation or reduction reaction of an analyte. The electroactive analyte is subjected to an electrical potential while the resulting oxydation or reduction current change is recorded with two electrodes. Thus glucose detection in microdroplets using Pt and Ag/AgCl electrodes or graphene-cobalt oxide needles achieving high sensitivity was demonstrated (Lindsay et al. 2007; X. Wang et al.



#### 4.1. Introduction - Droplet Detection Methods

---

2012). In droplet-segmented flow configuration, the setup generally employs electrodes integrated within a fluidic channel which successively contact the droplets when they pass by. For instance, on-chip approaches with integrated droplet electrochemical detection were proposed for enzyme kinetics and rapid kinetics reaction detection (Han, W. Li, et al. 2009; Han, Chang, et al. 2012). Similarly, Pt black-covered electrodes integrated in a microfluidic chip detector has been used for glucose detection in human blood serum (Gu et al. 2014). Detection of Da at ultra-low Limit of Detection (LOD) (5 pmol) was demonstrated using a microfluidic chip containing a band electrode covered with carbon nanotubes for electrochemical detection (Sansuk et al. 2013). Although the principle was shown on a monophasic flow, there are good chances to use the same method on a bi-phasic droplet flow which would certainly provide valuable information regarding neurotransmitter content in the samples. The main issue with electrochemical detection relates to the electrode surface cleanliness, a crucial parameter for a stable detection, which is difficult to maintain after several analysis cycles. Another problem may arise from the difficulty to distinguish between two different species with close oxidation or reduction potential contained in a same sample. Regarding this aspect, ECF-containing sample analysis without purification step will most probably be very challenging as the ECF contains multiple interfering elements.

ESI is a technique used in MS in which a high potential field (kV range) is generated between a liquid (sample) and the MS detector creating an aerosol (or a spray) of charged molecules towards the detector. The method has been proven to be compatible with droplet segmented flows (S. Sun et al. 2014; Kelly et al. 2009; Pei et al. 2009). In bi-phasic segmented flows, the oil phase is not charged and does not form a spray but is rather washed away from the conical spray when the potential is kept under 1 kV to 1.5 kV (Q. Li et al. 2010). High throughput, label-free screening of enzyme inhibitor was demonstrated using droplet segmented flows analyzed with ESI-MS (S. Sun et al. 2014). In another recent study, a microfluidic chip incorporating a droplet flow and a surface electrode demonstrated ESI occurring from a spynhole (Gasilova et al. 2014). The droplet MS detection took place without sample dilution or oil removal which is particularly convenient. ESI-MS is proven to be a versatile method permitting to

## Chapter 4. *In Vivo* Neurochemical Sampling

---

extract a lot of information from a given sample regarding its composition and elements/molecules concentration without being disturbed by the oil phase of a bi-phasic flow. However, the ESI approach suffers from a low tolerance to salts as they tend to strongly cover the signals of other molecule of interest contained in the sample. This can be an issue for the analysis of brain ECF-extracted samples which contains a high quantity of biological salts.

Surface sample-based MS are powerful methods characterized by a high sensitivity to solid samples and limited preparation steps. The configuration of the reading zone (sample target) is often associated with an xy-stage which makes it compatible with various samples configuration including a set of droplets distributed at known position. ICP-MS is well known for the quantification of elements in biological samples at the trace and ultratrace level ( $< 1$  ppm) (J Sabine Becker, Zoriy, et al. 2010). The combination of a laser ablation (LA) system with ICP-MS provides a spatial dimension to the analysis. It has been recently used to determine the elements distribution (mapping or imaging) in thin tissue sections of brain ( $20\ \mu\text{m}$  to  $30\ \mu\text{m}$  thick) which contributed to the understanding of the biological processes involved in this region (J. Sabine Becker et al. 2007; J Sabine Becker, Matusch, et al. 2010; Sabine Becker 2013; B. Paul et al. 2015). In particular, neurological studies focusing on monitoring the changes in concentration of Mn, Fe, Cu and Zn occurring in Parkinson's diseased (PD) rats were recently performed (Hare et al. 2009; Matusch et al. 2010; Sussulini et al. 2012). However, the analysis based on thin-tissue brain sections require the sacrifice of the animal and only reflects the elements image of a tissue at a given point in time, which restricts the analysis to rather static observations.

It is believed that adapting surface-based MS detection such as ICP on droplet-collected brain-fluid samples could give rise to a reliable approach to recover biological events and analyze their accompanying neurochemistry. The droplet collection system gives access to a new dimension, the time evolution of the neurochemicals captured at a precise location in the brain. The droplets, stored in a capillary, constitute a spatio-temporal pattern reflecting the extracted liquid composition overtime. In order to perform the detection we propose a specific parylene base plate (a target reader) on which the droplet samples can be easily

distributed and isolated at known positions. This parylene base plate will play the role of interface between a specific sample configuration (droplet train) and an advanced analysis method (surface-based MS).

## 4.2 Materials and Methods

### 4.2.1 Probe

A neural probe combining microelectrodes and a microfluidic channel system (monolithic integration) has been designed and assembled. The distal tip includes a T-junction droplet generator which enables the collection and the extraction of ECF-containing fluid plugs separated by an inert oil (perfluoromethyldecalin, PFD). Extensive explanation regarding the fabrication process as well as characterization of the system can be found in chapters 2 and 3. Compared to the precedent probe design, an additional fluidic channel was bonded (EPO-TEK 301-2FL, Epoxy Technology) on the same surface than the one containing all the active elements, its outlet being in close proximity to the sampling inlet ( $300\ \mu\text{m}$ ). It is made of a fused silica capillary (ID =  $50\ \mu\text{m}$  and OD =  $196\ \mu\text{m}$ ) and is used for the perfusion of a low flow saline solution (0.9 % NaCl) in the area where the microsampling occurs. The capillary is smaller than the width of the probe ( $240\ \mu\text{m}$ ) which makes it compliant with the system compactness and minimally invasive feature. Figure 4.1 (a) shows schematically the neural probe device during collection of brain-fluid samples. The neural probe includes two microfluidic entries (proximal side) which can be operated separately via two pressure-driven reservoirs (Fluigent, module MFCS-MZ) filled with PFD. Two fused silica capillaries (ID =  $250\ \mu\text{m}$ , OD =  $360\ \mu\text{m}$  and length = 40 cm) connects the probe microfluidic entries with the reservoirs. The collection capillary is filled with brain fluid samples while the injection capillary is filled with PFD only. This system enables to apply a positive or negative pressure (relatively to local pressure) on the microchannels filled with PFD, thus controlling the droplet generation process occurring at the probe distal tip (Petit-Pierre et al. 2016). Figure 4.1 (b) shows the distal tip of the neural probe including the main elements

## Chapter 4. *In Vivo* Neurochemical Sampling

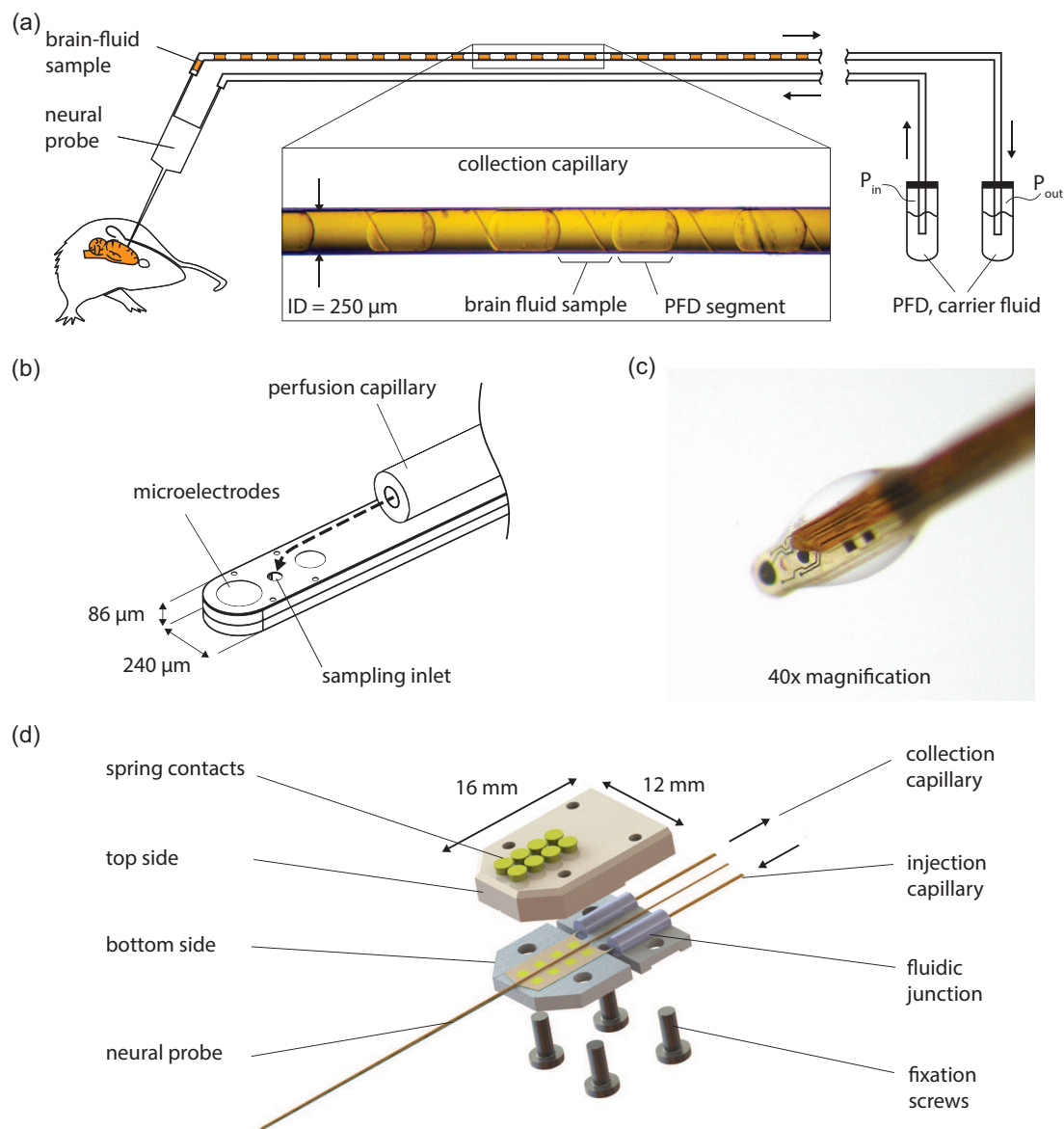


**Figure 4.1** (a) The brain-fluid samples are extracted using the neural probe and collected in a capillary. The samples are organized in a droplet train separated by PFD. The system is controlled by two pressure pumps. (b) The perfusion capillary is situated in close proximity to the main elements included on the neural probe distal tip. The dashed line shows the path of the injected perfusate before being recollected in the sampling inlet (push-pull function). (c) A drop of saline solution is released via the perfusion capillary demonstrating the functionality of the system. (d) 3D exploded view of the interface unit comprising the neural probe clamped between the bottom and the top parts.

such as the sampling inlet, the microelectrodes and the perfusion capillary. The pathway of the injected perfusate before being recollected in the sampling inlet is represented by the dashed line. On figure 4.1 (c), a drop of saline solution is released via the same capillary demonstrating the functionality of the system. It can be noted that the drop efficiently wets the probe tip including the sampling inlet.

### 4.2.2 Interface Unit

Polymer-based neural probes are often difficult to interface because they are mechanically flexible and therefore difficult to manipulate or to connect to harder materials. We solved this issue by designing an interface unit particularly small and light allowing for a reliable connection to the electrical contacts as well as the fluidic microchannels of the probe. Figure 4.1 (d) shows an exploded 3D view of the main elements of the interface unit in which the probe can be clamped after connecting the top and bottom part. Four fixation screws are used to connect the parts together while the electrical connection is made with gold spring contacts. The materials used to build the interface unit were chosen for their good biocompatibilities (peek, stainless steel, silicone, gold) which makes the system compliant with *in vivo* experimentation.

### 4.2.3 *In Vivo* Experiments

All experiment procedures were performed in accordance with the local animal care authorities. A Sprague Dawley female rat (Charles river laboratory) weighing 270 g was included in the experiment. The procedure was performed under Isoflurane anaesthesia (4 % at induction, 2 % for maintenance) and included, prior to any surgical act, a preliminary analgesia by buprenorphine injected under the neck skin (Temgesic, 0.1 mg/kg). The subject was fixed in a stereotactic frame allowing to precisely target and reach the brain striatum while maintaining the anesthesia. Stereotactic coordinates were set to + 0.5 mm anterior, + 3.0 mm lateral and - 5.0 mm ventral from bregma and the toothbar was set to - 3.3 mm. First

## Chapter 4. *In Vivo* Neurochemical Sampling

---

a craniotomy was performed on the subject using a drill; the external diameter of the hole being relatively small with 0.8 mm. Then the probe was implanted slowly in the tissues while injecting the saline solution through the perfusion capillary at a constant flow rate of 50 nL/min in order to avoid clogging. Two minutes after the target area was reached, the droplet sampling system was turned on. During this phase, a positive pressure  $P_{in} = 50$  mbar and a negative pressure  $P_{out} = -400$  mbar was applied (relatively to the local pressure) during 20 min. 10 s prior to starting the sampling, saline solution (0.9 % NaCl) was injected at a flow rate of 100 nL/min using the perfusion capillary. The saline perfusion was maintained during the entire sampling procedure. After the sampling, the probe was slowly retracted from the tissues. After the procedure, the rat brain was transcardially perfused with a 4 paraformaldehyde containing saline solution. 25  $\mu$ m slices were cut from the brain in the region of the implantation using a Microtome (Leica biosystems) and placed in a sodium azide solution. The slices were first separated and stained (1 min in cresyl violet dye) and then rinsed with ethanol and toluol solvents. At the end of the experiment, the collection capillary in which the droplets were collected was disconnected from the probe and stored at - 20 °C. Particular level of attention was provided to maximize the animal well-being along the *in vivo* experiment phase.

### 4.2.4 Analysis Method

#### 4.2.4.1 Parylene Base Plate Fabrication

One of the fundamental feature of the neural probe presented in this work is to maintain a high temporal resolution by keeping a spatial separation between each collected droplet. A focus of this work was therefore to maintain this separation as well as the correct order between droplets at every step of the analytical process. For this purpose, a parylene-based substrate was developed and built using microfabrication methods. A float glass wafer was first piranha cleaned, and then coated with a 2  $\mu$ m parylene layer. An Excimer laser (Optek LSV3) was then used to drill 20  $\mu$ m holes with a specific pattern on the parylene membrane.

The laser parameters were adjusted in order to drill the holes until reaching the float glass wafer without altering its surface (power 2.5 kJ, attenuation 50 %, 15 repetitions, repetition rate 50 Hz). Argon gas protection was used in order to limit redeposition of the burned waste on the substrate. After manufacturing the parylene base plate comprised a grid of holes equally spaced according to an optimized pattern which could efficiently capture aqueous droplets.

### 4.2.4.2 Droplets Distribution Procedure

The developed parylene base plate described above allowed to easily distribute, one by one, the droplets on the parylene membrane thus avoiding any cross-contamination or loss of order. As showed in figure 4.2 (a), the droplet distribution procedure consisted in slowly moving the collection capillary filled with brain-fluid samples parallel to the parylene surface while applying a positive flow of  $0.02 \mu\text{l}/\text{min}$  using a syringe pump (Cetoni, Nemesys). A parylene base plate typically includes 2 rows of 5 similar holes, the holes being 2 mm spaced (x and y direction) while the beginning and the end of the series are signalled by a cross shape (laser machined). In order to validate this novel, tailor-made parylene base plate and accompanying distribution method, a red-colored water droplet enclosed between 2 PFD plugs stored in a capillary was distributed over a parylene hole and monitored until complete drying. Figure 4.2 (c) shows a sequence of images during which the drying process occurs (140 s, at room temperature under microscope light). The PFD (clear liquid) evaporates rapidly (35 s) while the red-colored droplet takes longer to dry (140 s). This is due to the high affinity of the PFD with the parylene membrane tending to spread the oil and increase the exchange surface while the contrary occurs for the water droplet. A slight recentering of the water sample over the parylene hole occurs during the first 20 seconds which is beneficial for the line by line analysis defined with the laser ablation system coupled to ICP-MS. The final diameter of the dried spot is  $180 \mu\text{m}$ . Once dried, the samples are easier to manipulate and compatible with different surface-based analysis methods. Compatible MS-based approaches would typically comprise matrix assisted laser ionization mass spectrometry (MALDI-MS), secondary ion mass spectrometry (SIMS) or desorption electrospray ionization



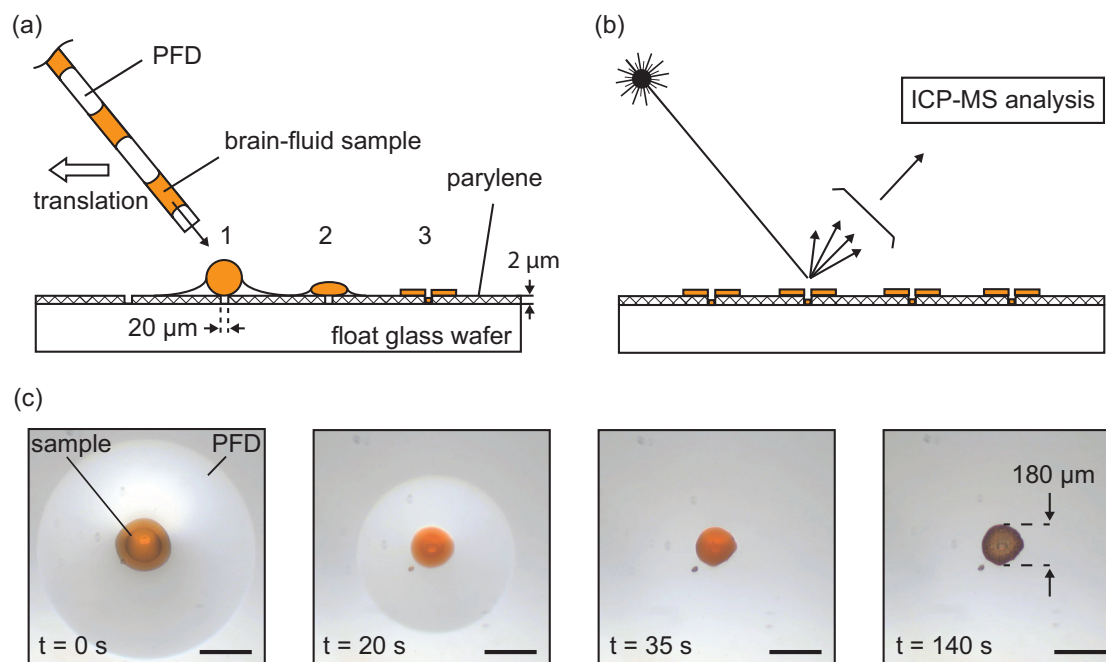


**Figure 4.2** (a) Droplet distribution procedure on the parylene base plate. The brain-fluid samples are distributed on  $20\mu\text{m}$  drilled holes in a  $2\mu\text{m}$  thick parylene layer. This substrate tends to fix the aqueous samples in position while the parylene tends to pull away the PFD oil (b) After drying, the brain-fluid samples are laser ablated and analyzed using ICP-MS. (c) Drying sequence which shows the evolution of a red-colored water droplet and the adjacent PFD carrier phase (scale bar =  $200\mu\text{m}$ )

mass spectrometry (DESI-MS).

#### 4.2.4.3 LA-ICP-MS

As a first approach, the analysis were performed using an inductively coupled quadrupole-based mass spectrometer (7700 series ICP, Agilent technologies) coupled to a solid state laser ablation system (NWR213, ESI). This equipment comprised a focused Nd:YAG system used to laser ablate the sample material. The resulting products were then transported by helium (carrier gas) into the inductively coupled plasma (ICP) which ionized the samples. The positively charged ions were then extracted from the plasma and analyzed in a quadrupole mass spectrometer (MS) which separated them with respect to their mass-to-charge ratio to be finally detected by the ion detector. This system is known for



detecting metals and several non-metal elements at extremely low concentration ( $< 1$  ppm) and is commonly used to perform cerebral bioimaging on brain tissue sections (J. Sabine Becker et al. 2007). The parameters used to perform the analysis of the brain-fluid samples were defined as the following; laser energy density  $5.2 \text{ J/cm}^2$ , energy output 17 %, laser focus spot size  $100 \mu\text{m}$ , laser pulse duration 20 ns, repetition rate 20 Hz, scanning speed  $100 \mu\text{ms}^{-1}$  and the carrier gas flow rate 800 ml/min, MS acquisition rate 1 Hz. Two-dimensional (2D) imaging was performed on the previously described parylene base plate after the distribution of the brain-fluid samples as showed in figure 4.2 (b). A defined area ( $10 \text{ mm} \times 2 \text{ mm}$ ) comprising 5 spots of interest as well as 5 control spots was laser ablated in 3 passes (space between 2 spots = 2 mm, distance between 2 lines = 1 mm). The first pass performed the measurement over the 5 spots of dried brain-fluid samples, the second pass was set over an area covered with parylene only and the third pass went over 5 control spots constituted of saline solution (0.9 % NaCl). All data were processed using Matlab and visualized using MSiReader (Robichaud et al. 2013).

### 4.2.4.4 Quantification

A standard calibration solution (Multi-element 2A, Agilent technologies) was used to generate the calibration curves employed for quantifying the metal elements found in the brain-fluid samples. Deionized water solutions with known concentration of metal standards ( $27$  elements,  $100 \text{ ngmL}^{-1}$ ,  $1 \mu\text{gmL}^{-1}$  and  $10 \mu\text{gmL}^{-1}$ ) were prepared. In order to mimic the final configuration of the *in vivo* collected samples, droplet trains of standards solution separated by PFD plugs were prepared using a flow focusing system driven by 2 syringe pumps (Cetoni, Nemesys). The droplets were collected in capillaries and then distributed over a parylene base plate according to the process described in paragraph 4.2.4.2. LA-ICP-MS analysis was performed on these samples and calibration curves were constituted considering the maximum concentration value averaged over 5 droplets.

### 4.3 Results

#### 4.3.1 Acute Neurochemicals Sampling

Acute neurosampling in rat brain tissues using an advanced droplet collection system included within a polymer-based probe was successfully demonstrated for the first time. Figure 4.1 (a) shows a portion of a collection capillary filled with brain-fluid samples separated by PFD segments. We observed a regular spacing between the samples while the volume of each sample is similar with an average of  $17.9 \pm 1.8$  nL (mean  $\pm$  SD, n= 10). Interestingly, a change of the capillary inner surface properties occurred. Indeed, prior to use, the inner surface of the collection capillary was rendered hydrophobic using a silanization process. In preliminary tests, the PFD segments showed high affinities with the inner surface. After the passage of the first brain-fluid samples, we noticed the contact angle between the glass surface and the PFD was rather  $135 \pm 5^\circ$  which confirmed the inner surface of the capillary returned to a hydrophilic state. This rapid change is probably due to the binding of proteins against the inner capillary glass surface. Since the only liquid injected at the sampling spot is a saline solution (0.9 % NaCl), this also proves qualitatively that the collected liquid samples captured molecules from the ECF. Figure 4.3 (a) shows the surgical setup during a measurement session. The neural probe is maintained in the interface unit which is fixed to the stereotactic-guided arm and can therefore be precisely implanted in the targeted brain area (striatum). Figure 4.3 (b) shows a coronal slice selected from this set which comprises the probe track in the tissues. The entry point as well as the end of the probe course can be identified in the upper brain structures (cortex region) and in the deeper region (top and bottom arrows, respectively). The probe track is difficult to identify, more particularly in the deeper region (striatum) where the impact on tissues is hardly distinguishable. This proves the approach is minimally invasive. The probe tip location is free of any void which confirms that no cavities are created by the perfusion and that a tight link between the probe and the tissues probably occurs.

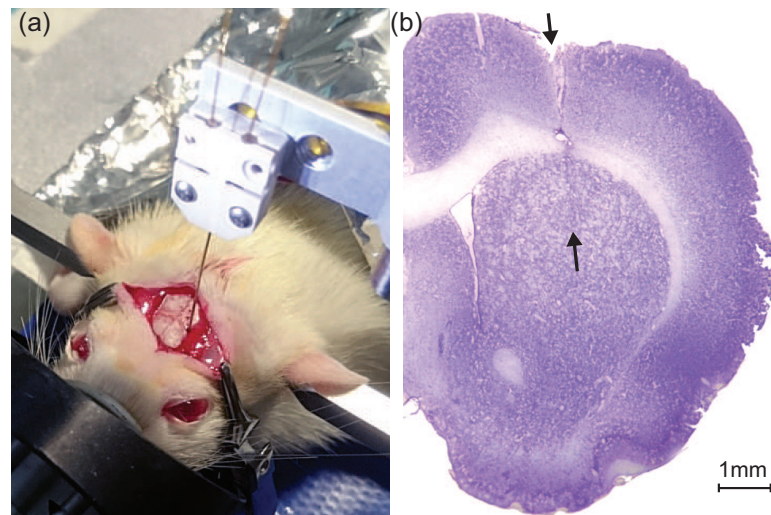


**Figure 4.3** (a) Surgical setup during left brain hemisphere implantation on a rat. The neural probe is maintained in the interface unit which is fixed on the stereotaxic arm. (b) Stained left brain hemisphere after implantation of the neural probe. The black arrows represent the entry point and the end of the probe tip when inserted in the cerebral tissues.

### 4.3.2 Analysis of *In Vivo* Collected Samples

After the sampling process was completed, the brain-fluid samples were distributed on the parylene base plate according to the procedure described in chapter 4.2.4.2. LA-ICP-MS mapping was performed on this substrate in order to detect the presence of elements contained in the brain-fluid samples. Figure 4.4 (a) describes the location of the samples on the parylene base plate prior to analysis. The upper section comprises the 5 brain-fluid samples (orange spots), the middle section parylene only and the bottom section comprises 5 control samples constituted of 0.9 % NaCl saline solution (white spots). The charts represented in figure 4.4 (b) show the relative abundance (arbitrary unit) of selected element as a function of the spatial positioning. We observe a strong signal for sodium (Na), magnesium (Mg), potassium (K) and calcium (Ca) at the position where the brain-fluid samples were distributed. As expected the signal of the K and Na is particularly high, these ions being the most abundant in the brain extracellular fluid (Eric R. Kandel et al. 2013). As expected, no signal is observed in the parylene-covered region (second row of the laser trace, every charts). The chart of the Na is of particular interest since the signal is also

## Chapter 4. *In Vivo* Neurochemical Sampling

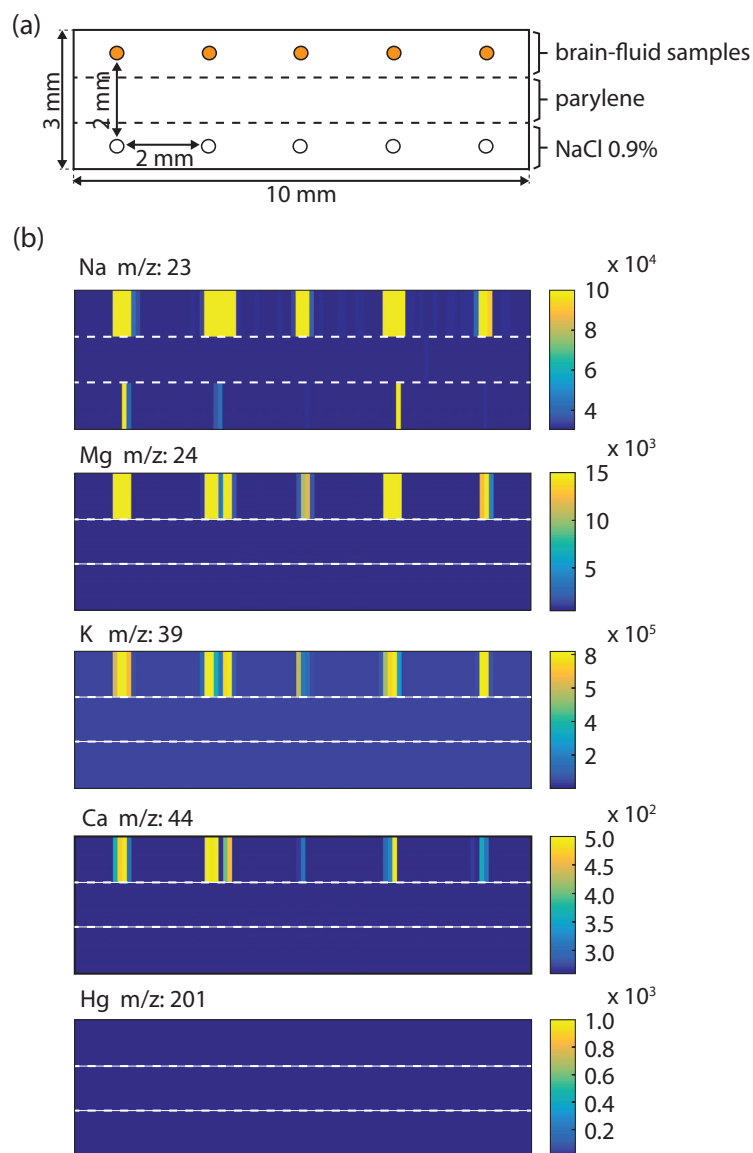


**Figure 4.4** (a) Samples configuration prior to analysis. The upper section includes the 5 brain-fluid samples (orange spots) while the bottom section comprises 5 control samples of saline solution (0.9 % NaCl, white spots). (b) Relative abundance (a.u.) of the elements Na, Mg, K, Ca and Hg (negative control) found on the brain-fluid samples.

present over the samples containing the perfused saline solution only (0.9 % NaCl, control). This was expected and is confirmed by the charts referring to other elements which do not present any signal on the same region. The last chart of figure 4.4 (b) shows the relative abundance of mercury (Hg) well-known as a neurotoxic metal (Michalke et al. 2010). We clearly conclude that no trace of Hg is present in the brain-fluid samples which was expected and therefore

constitutes a negative control. We observe that the width of each droplet on the first line is variable, the second droplet signal being particularly large, the third being small. The third droplet dried spot was probably hit by the laser at the edge of the beam path. This probably resulted from a slight misalignment of the droplet dried spots with respect to the path of the laser beam. Figure 4.5 provides an example of such a misalignment. Figure 4.5 (a) shows the droplet dried spots (black) and the location of the parylene holes (white crosses). Figure 4.5 (b) shows the laser beam trace over the dried spots (laser focus diameter is  $100\mu\text{m}$ ) while figure 4.5 (c) shows the equivalent droplet area "seen" by the laser and the detection equipment. Finally, the signal output relative intensities are represented on figure 4.5 (d). Apart from the sample initial volume, the pixel widths depend on the speed of acquisition of the MS equipment as well as the speed of the laser beam (acquisition rate = 1 Hz, laser beam speed =  $100\mu\text{ms}^{-1}$ ). The method of analysis implemented in this study is particularly

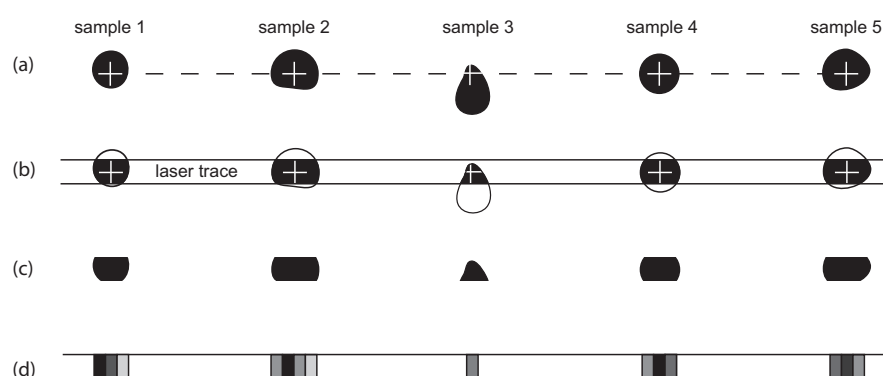


**Figure 4.5** (a) Dried spot contours of the brain-fluid samples (black) disposed over the parylene base plate holes (signaled by white crosses). (b) Laser trace over the dried spots. (c) Equivalent area of the dried spots seen by the detection equipment. (d) Final signal readout after analysis (darker means more concentrated).

powerful in the sense it is not limited to a single analyte but can be implemented on multiple elements with a single sample. Furthermore, it is compatible with the constitution of a time-based molecular concentration record, reflecting the brain neurochemical composition overtime. In figure 4.6 (a), we present the relative abundance charts for copper (Cu), iron (Fe) and zinc (Zn) taken from 3 successive brain fluid samples. These metal elements are of particular interest for the neuroscientists since links with degenerative diseases have recently been

## Chapter 4. *In Vivo* Neurochemical Sampling

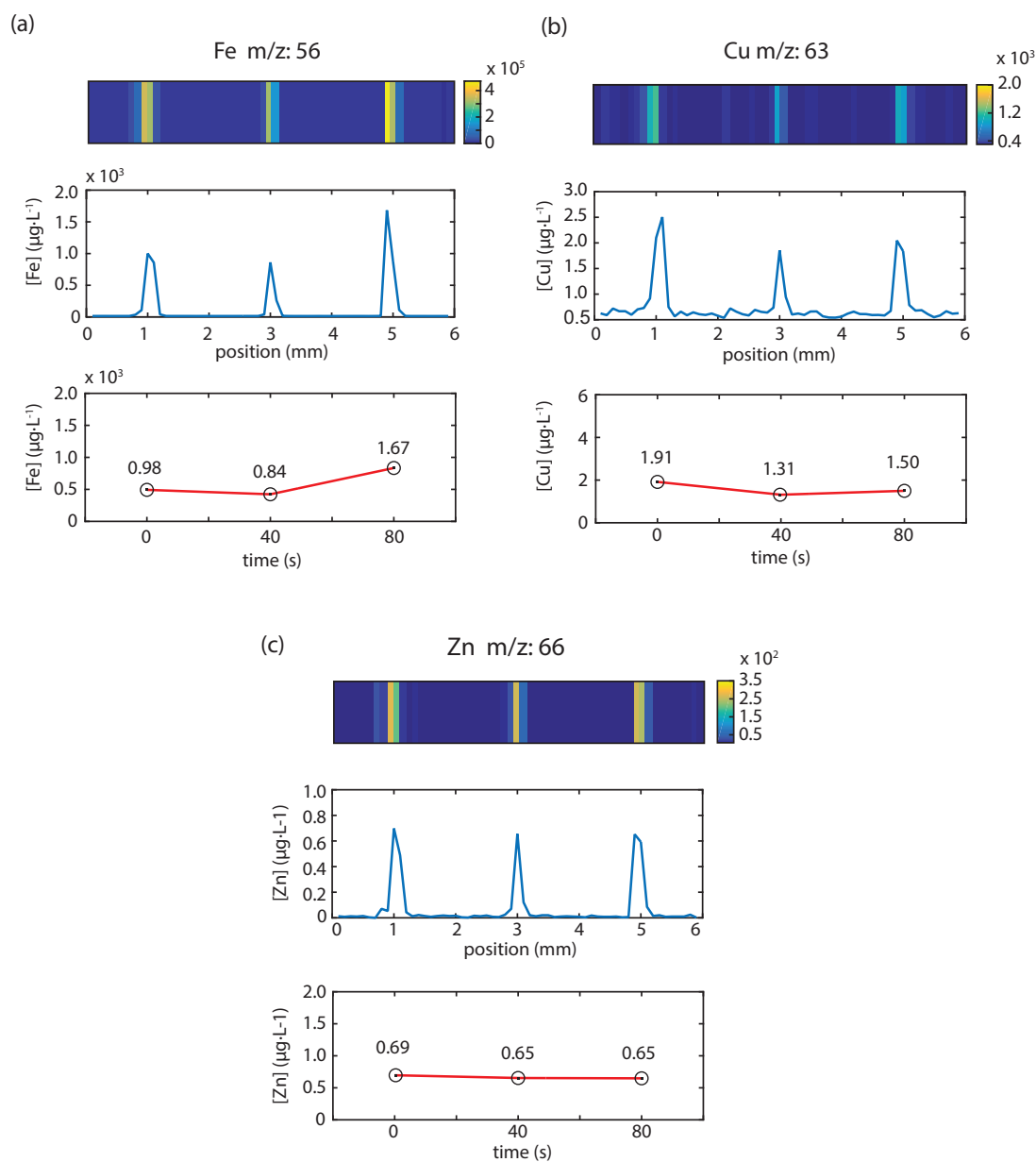


**Figure 4.6** (a) Cu , (b) Fe and (c) Zn quantification performed in three successive brain-fluid samples collected *in vivo*. For each element, the three graphs show (i) the trace metal relative abundance (a.u.), (ii) the spatial element concentration readout after detection and (iii) the temporal evolution of the concentration found in brain-fluid samples (sampling interval = 40 s).

highlighted. In particular Cu, Fe and Zn concentrations have been evaluated in Parkinson's disease (PD) mouse models (Matusch et al. 2010; Hare et al. 2009). Figure 4.6 (b) shows the corresponding metal distribution over the analysed

polyethylene base plate. Each peak is correlated with the position of the highest color intensities found in figure 4.6 (a). Figure 4.6 (c) shows the temporal evolution of the concentration found in brain-fluid samples (maximum value reached for each peak). This reflects the neurochemical composition of the implanted region overtime. The sampling interval was 40 s (sampling rate = 1.5 min<sup>-1</sup>). The metal concentration values reported are relatively stable in time which confirms the measurement method proposed here is consistent. Indeed, over this lap of time, we rather expect a constant biochemical composition of the cerebral tissues.

Second column of table 4.1 reports the mean concentration computed over the 3 brain-fluid samples (mean  $\pm$  SD) for each metal elements. We found for Fe  $1.17 \pm 0.44 \times 10^3 \mu\text{gL}^{-1}$ , for Cu  $1.58 \pm 0.31 \mu\text{gL}^{-1}$  and for Zn ( $0.67 \pm 0.03 \mu\text{gL}^{-1}$ ). We compared these values with recently reported basal concentration level of metal elements found in the rat hippocampus ECF measured using microdialysis (C. K. Su et al. 2008; Chung et al. 2007). The mean Cu and Zn concentration found here are in good agreement with the reported values (0.77 - 2.48 and 0.51 - 5.22  $\mu\text{gL}^{-1}$ , respectively). Unfortunately due to the limited number of studies performed in this field no data was available for the concentration of Fe in rat brain ECF. In our samples we measured Fe concentrations ( $1.17 \pm 0.44 \times 10^3 \mu\text{gL}^{-1}$ ) that were 3 orders of magnitude higher than for Cu ( $1.58 \pm 0.31 \mu\text{gL}^{-1}$ ) and Zn ( $0.67 \pm 0.03 \mu\text{gL}^{-1}$ ). In human cerebrospinal fluid (CSF), Fe baseline concentration is reported to be in the range of 22-235  $\mu\text{gL}^{-1}$  which is only slightly higher than Cu and Zn with 18.2-34  $\mu\text{gL}^{-1}$  and 17-32.9  $\mu\text{gL}^{-1}$ , respectively (Michalke et al. 2010). These values, which however pertain to the human CSF, indicate that the Fe concentration measured in our samples is abnormally high. This might be due to local damage to the brain microvasculature which may have caused micro-release of blood in proximity with the sampling inlet of the probe (residues of red blood cells are known for their high Fe concentration). When analysing the concentration of metal elements in a PD animal model, Hare *et al.* also described similar increase of Fe concentration localized around the needle track (Hare et al. 2009).

## Chapter 4. *In Vivo* Neurochemical Sampling

---

**Table 4.1** Mean Fe, Cu and Zn concentration found in the 3 the brain-fluid samples (mean  $\pm$  SD). The values are compared with the metal concentration found in ECF matrix from rat hippocampus.

element	brain-fluid samples ( $\mu\text{gL}^{-1}$ )	ECF rat ( $\mu\text{gL}^{-1}$ )
Fe	$1.17 \pm 0.44 \times 10^3$	-
Cu	$1.58 \pm 0.31$	0.77 - 2.48
Zn	$0.67 \pm 0.03$	0.50 - 5.22

### 4.3.3 Discussion

In this study we demonstrated a novel method for *in vivo* acute neurosampling using an advanced neural probe system combined with a MS-based detection method. The associated analysis platform comprises a specifically developed parylene base plate which allows for an efficient brain-fluid sample isolation while maintaining the droplets order and avoiding cross-contamination. The flat sample configuration makes it potentially compatible with multiple surface-based analysis method. Although we used ICP-MS in this work, the parylene base plate could easily be adapted and used in another spectroscopic-based equipment. For instance, MALDI-MS would be compatible and widen the range of analysis, allowing the identification and quantification of larger molecules such as proteins or metabolites. The off-line measurement approach implemented in this work is interesting since it drastically simplifies the *in vivo* measurement phase. Disconnection of the collection capillary from the probe and storage at  $-20^\circ\text{C}$  of the droplet train was demonstrated to be particularly convenient. Distribution of the collected droplets on the parylene base plate even weeks after the implantation could be easily performed without affecting the samples. Another major advantage is that the brain-fluid samples are enclosed between PFD plugs in a glass capillary and thus fully isolated from oxidation which often occurs on molecules such as neurotransmitters (e.g the Dopamine degradation to Dopamine o-quinone). A limit of the current method lies in the distribution of the droplets on the parylene base plate which is a manual operation. It introduces variability in the positioning of the droplets on the grid of holes. An option to



overcome this limitation would be to automate the droplet distribution process by controlling the relative position of the capillary on the grid, possibly using a robotic arm. Precisely controlled positioning of the capillary, combined with a constant positive flow should result in a regular distribution of the droplets over the parylene base plate. During preliminary testing of the distribution process, we have noticed that even in the absence of holes, it was possible to immobilize droplets and locally distribute solutes on the parylene film. Automating the distribution procedure could therefore allow to eliminate the need for performing the holes in the parylene layer, thus simplifying the fabrication process. A major attribute of the neural probe is related to its unique droplet collection system. This sampling approach is compatible both with high temporal resolution, but can also be operated in a slow, "on-demand" mode. Various applications can be envisaged to monitor biological events such as synaptic neurotransmission or changes in the basal chemical composition, which occur at very different time scales (milliseconds vs. hours). The segmentation of the collected liquid avoids Taylor dispersion and maintains the temporal history of the samples. This approach however requires the droplets to remain tightly separated. In the current device, the temporal resolution is defined at 40 s which is the lapse of time between two consecutive sampling of interstitial brain fluid. However, merging of droplets occurs in the zone where the collection capillary is connected to the neural probe outlet. This is due to the difference of area between the probe microchannel cross section ( $40\ \mu\text{m} \times 80\ \mu\text{m}$ ) and the inner diameter of the collection capillary ( $\text{ID} = 250\ \mu\text{m}$ ). Consequently, around 20 droplets (Volume = 0.84 nL) merge at this specific point until the constitution of a larger droplet, big enough to be transported by the carrier phase (PFD). This constitutes a loss of temporal resolution. A way to address this issue would be to reduce the fused silica capillaries dimension (e.g.  $\text{ID} = 50\ \mu\text{m}$ ) thus reducing the gap of area between both cross sections. This would however require to redesign another connector used at this fluidic junction and, possibly, the probe itself to facilitate the integration. As shown in figure 4.6 (a), the inner surface of the collection capillary, which is initially hydrophobic following silane gas treatment, becomes hydrophilic after the passage of the liquid sampled in the brain. This change in surface properties of the capillary inner wall may as well contribute to the

## Chapter 4. *In Vivo* Neurochemical Sampling

---

contact between droplets. Improving the capillary wall hydrophobic properties could address this limitation. This could be achieved by the deposition of a stable hydrophobic film (1 - 2  $\mu\text{m}$ ) on the inner wall of the capillary. The role in brain function of major cations, such as  $\text{Na}^+$ ,  $\text{K}^+$ ,  $\text{Ca}^+$  and  $\text{Mg}^{2+}$  have been thoroughly characterized. Although less studied, transition metal elements are also known to play critical roles in synaptic transmission, and might be implicated in neurological diseases (Cheng Kuan Su et al. 2010; Burdette et al. 2003). For instance, Fe is a cofactor for a variety of enzymes responsible for the synthesis of dopamine in synapses (Cheng Kuan Su et al. 2010; Moos, Nielsen, et al. 2007; Moos and Rosengren Nielsen 2006), Cu is hypothesized to inhibit the voltage-gated calcium channel of synapses and is responsible for impaired neurotransmission when its concentration is too high (Cheng Kuan Su et al. 2010; Zatta et al. 2007; Schlieff et al. 2006) while  $\text{Zn}^{2+}$  is involved in the release of the glutamate and  $\gamma$ -aminobutyric acid (GABA) release (Cheng Kuan Su et al. 2010; Mocchegiani et al. 2005; Takeda, Minami, et al. 2004; Takeda, Hirate, et al. 2003). Although our system is compatible to different type of surface-based analysis, LA-ICP-MS is a promising method for neuroscience applications since it allows to draw a "picture" of trace elements distribution in a brain section at a given time. Compared to the current approach consisting in mapping a brain tissue sections from an animal sacrificed at a given point in time, the method proposed here is minimally invasive and allows for multiple recordings performed on a same animal. This is of particular interest when the focus of the study is linked to neurodegenerative studies like Parkinson's (PD) or Alzheimer's (AD) disease which develop over long time scale. Our approach doesn't allow to perform multi-site chemical mapping but it gives access to a 3<sup>rd</sup> dimension, the time evolution, at a very precise location recorded in the brain which can be of major interest when studying PD or AD.

### 4.4 Conclusions

In this chapter is demonstrated the first *in vivo* validation of a microscale droplet collection system included at the very distal tip of a neural probe. Neurochemi-

cals present in the brain ECF of a rat were successfully sampled with this device. A specific parylene base plate is proposed as an interface between the brain-fluid samples (organized in a droplet-train) and the surface-based detection method. This parylene base plate allows for fixing the droplets in position while maintaining their order and avoiding cross contamination, thus guarantying the time-history consistency of the sampling. This platform is potentially compatible with multiple analysis systems using planar sample configuration as target. LA-ICP-MS was used to analyze the brain-fluid samples. The results confirmed the presence of elements such as Na, Mg, K and Ca which are known for their contribution in the regulation of biological processes at the synaptic level. Furthermore quantification (droplet by droplet) was demonstrated for the trace elements Cu, Fe and Zn known for playing a role in neurodegenerative disease development. The results obtained with this method are similar to concentration values reported in the literature. The collected samples constituted a high resolution spatio-temporal pattern (droplets interval = 40 s) representative of the neurochemical state at the tip of the implanted probe. This tool provides new opportunities with the perspective to study electrical stimulation on tissues and its related neurochemical response. This topic will specifically be addressed in the next chapter.



## Chapter 5

# Neurochemicals Recording During Electrical Stimulation of Cerebral Tissues

### 5.1 Introduction

The device demonstrated in chapter 4 enabled to successfully collect brain-fluid samples *in vivo*. In this chapter, further insight is gained through the establishment of two models which allow to link the brain-fluid samples analysis readout to the actual species concentration in the tissues. Then, the results of the simultaneous tissue electrical stimulation and neurochemical recording is reported. This chapter is consequently subdivided in two distinct sections; (i) a modeling section and (ii) an *in vivo* experimental section. The models developed in this chapter will allow to characterize the droplet sampling rate and its relation to the probe efficiency. This parameter (probe efficiency) is essential for comparing the device performances against the actual recovery efficiency of existing microdialysis approaches. The construction of this chapter slightly differs from the standard structure because of its subdivision in 2 distinct parts. The end-discussion will consequently be focused on the *in vivo* results rather than on the models outcomes. The models

## Chapter 5. Neurochemicals Recording During Electrical Stimulation of Cerebral Tissues

---

perspectives and limits are however addressed at the end of each concerned sections (5.2.1 and 5.2.2).

## 5.2 Modeling

### 5.2.1 Droplet Evaporation Model

Neurochemical measurements typically rely on the estimation of the concentration of species of interests such as neurotransmitters or ions involved in AP transmission. In this section, a model is established to estimate and retrieve the volume concentration ( $C_V[\frac{1}{m^3}]$ ) from surface concentration ( $C_S[\frac{1}{m^2}]$ ) which is a known value obtained from the analysis. This can be particularly useful when only a portion of the dried spot is analyzed; despite an incomplete analysis the initial droplet concentration could be retrieved anyway.

When a droplet is deposited on a flat surface, different profiles are observed which depend on the nature of the substrate, the fluid surface tension and the surrounding environment. As first described by Picknett and Bexon, we identify 2 modes of evaporation for a sessile droplet in still air provided its mass is less than about 1 mg; (i) the Constant Contact Angle (CCA) and (ii) the Constant Wetting Area (CWA) (Picknett et al. 1977). In the CCA mode, the droplet contact angle remains constant during drying while in the CWA mode the wet area remains constant throughout the process as depicted in figure 5.1 (a) and (b), respectively. In our case though, the situation is not trivial since the PFD is also present during a part of the evaporation cycle. From observations, we notice the droplet exhibits a mixed-mode behavior which we can separate in two phases. In a first phase the droplet exhibits a CCA behavior until complete evaporation of PFD. Then, in a second phase, the droplet transit to a CWA regime until complete sample drying occurs. The PFD, which is denser than water ( $\rho = 1972 \text{ k/m}^3$ ), forms a pillow around the droplet and modifies the local interface properties. It seems therefore reasonable to assume the presence of PFD in the first phase tends to render the situation super-hydrophobic, seen from the droplet (McHale et al.

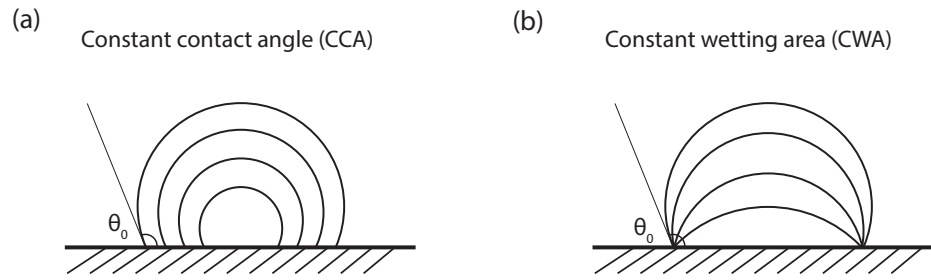


**Figure 5.1** (a) Constant contact angle mode in which the contact angle  $\theta$  remains constant and equal to  $\theta_0$  throughout the evaporation process. (b) Constant contact area in which the wet surface remains constant while  $\theta$  decreases during the drying process.

2005). CCA regime is in all likelihood caused by the presence of the hydrophobic surrounding PFD. In such a situation, the final dried spot radius is defined by the first evaporation phase where the CCA mode occurs and the wet area decreases. Figure 5.2 summarizes the different phases upon complete drying. Picknett and Bexon proposed in 1977 a theoretical analysis allowing to predict the evaporation rate of sessile droplets in the CCA mode (Picknett et al. 1977). Maxwell's equation describing the evaporation rate of a drop in an infinite medium is given by:

$$\frac{dM}{dt} = -4\pi Dr(c_0 - c_i) \quad (5.1)$$

where  $M$  is the mass of a sphere of radius  $r$ ,  $D$  is the molecular vapor diffusion constant in air,  $c_0$  the vapor density close to the sphere surface and  $c_i$  far from the sphere. As we are in the CCA mode, the contact angle is constant ( $\theta = \theta_0$ ) and the relation can be written:

$$\frac{dM}{dt} = \frac{-kE\frac{c}{r}M^{1/3}}{2\rho^{1/3}} \quad (5.2)$$

with

$$k = 4\pi D(c_0 - c_i) \quad (5.3)$$

$$E = \left( \frac{3}{\pi(1 - \cos(\theta_0))^2(2 + \cos(\theta_0))} \right)^{1/3} \quad (5.4)$$

## Chapter 5. Neurochemicals Recording During Electrical Stimulation of Cerebral Tissues

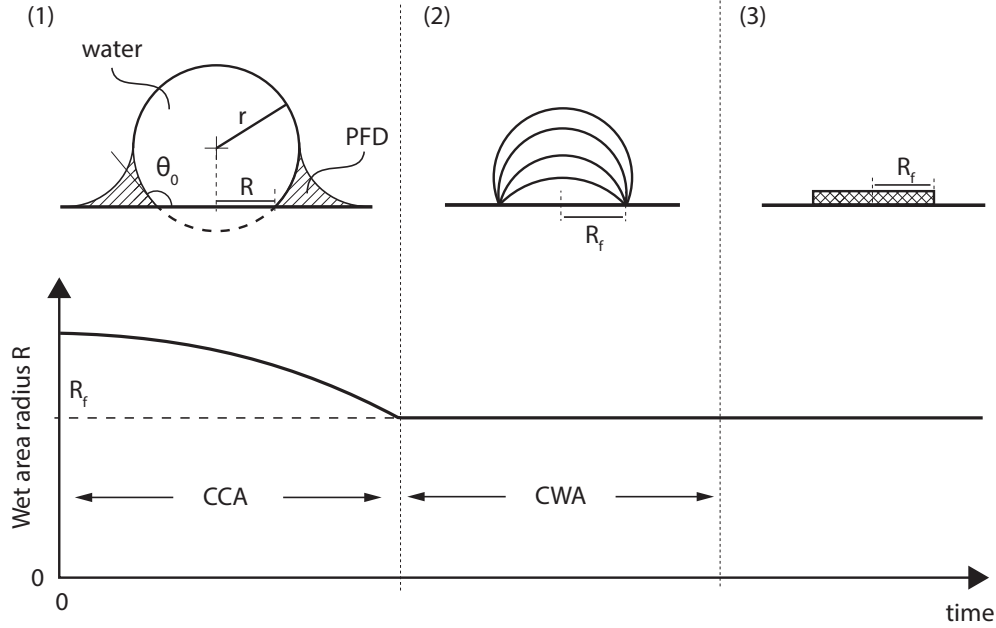


**Figure 5.2** Droplet drying process and associated evaporation mode of a brain-fluid sample after distribution on the parylene base plate. In the first phase (1) the water droplet of radius  $r$  cohabits with the PFD and exhibits a contact angle  $\theta_0$  with the surface. In this phase the evaporation mode is assumed to be in a CCA regime. In the second phase (2), the PFD is completely evaporated and the situation corresponds to a CWA evaporation mode. At this stage the final dried spot diameter ( $R_f$ ) is already known as  $R$  remains constant. The final phase (3) is reached when the sample is dried. The graph shows the expected evolution of the wet area radius  $R$  as a function of these three phases over time.

$$\frac{C}{r} = 0,00008957 + 0,6333 \cdot \theta_0 + 0,116 \cdot \theta_0^2 - 0,08878 \cdot \theta_0^3 + 0,01033 \cdot \theta_0^4 \quad (5.5)$$

where  $k$ ,  $E$ ,  $\frac{C}{r}$  and  $\rho$  (the sphere fluid density) are constants.  $E$  is a constant expressing the link between the mass  $M$  to the volume of the sessile drop ( $M = \rho \frac{r^3}{E^3}$ ).  $C$  is the evaporation capacitance of the equiconvex lens formed by the sessile droplet and its image in the substrate. The expression of the ratio  $\frac{C}{r}$  is given here for  $0.175 \leq \theta_0 \leq \pi$  as it covers most of the contact angles<sup>1</sup>. The equation

<sup>1</sup>Another relation is reported for  $\theta_0 < 0.175$  in (Picknett et al. 1977)



5.2 can be integrated which gives:

$$M = M_0 - \left( \frac{tkE\frac{C}{r}}{3\rho^{1/3}} \right)^{2/3} \quad (5.6)$$

where t is the time. From the mass M we can extract the radius of the sessile drop r with the relation:

$$r = E \left( \frac{M}{\rho} \right)^{1/3} \quad (5.7)$$

The final wet area radius R reads then:

$$R = r \cdot \cos \left( \theta_0 - \frac{\pi}{2} \right) \quad (5.8)$$

From there it is possible to compute the wet area radius over time during the first phase of drying, in the CCA mode. At the issue of this phase, the final radius  $R_f$  of the dried spot is known. The wet area radius R of a 21 nL (=  $2.1 \times 10^{-8}$  kg) water droplet can be predicted with the set of parameters defined in table 5.1.

**Table 5.1** Parameters used in the dried spot model to predict the evaporation behavior of a water droplet in presence of PFD.

parameter	value	units
$M_0$	$2.1 \times 10^{-8}$	kg
$\rho$	1000	kg/m <sup>3</sup>
$\theta_0$	135	°
D	$2.82 \times 10^{-5}$	m <sup>2</sup> /s
$c_0$	$2.32 \times 10^{-2}$	kg/m <sup>3</sup>
$c_i$	$1.21 \times 10^{-2}$	kg/m <sup>3</sup>

Figure 5.3 shows the variation of R (wet area radius) over time as predicted by the model (blue line). The model prediction has been compared to experimental data acquired by monitoring the evaporation of a 21 nL water droplet on a parylene base plate. The sample was prepared and extracted from a PFD-water droplet train and distributed over a parylene base plate (free of hole). Optical measurements (normal to the surface) of the wet area radius R evolution by image

## Chapter 5. Neurochemicals Recording During Electrical Stimulation of Cerebral Tissues

analysis using the software ImageJ was performed along the evaporation cycle. The initial contact angle  $\theta_0$  was evaluated at  $\theta_0 = 135$  deg. The experimental data are showed in figure 5.3 in orange. The image sequence during the droplet

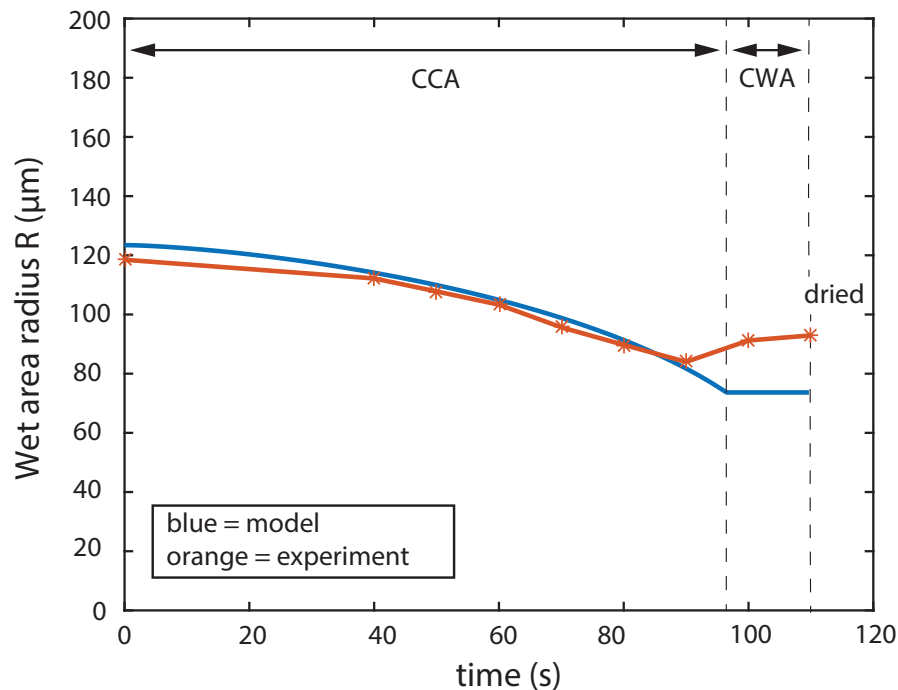


**Figure 5.3** Variation of radius R over time during the evaporation of a water droplet ( $V = 21$  nL) in presence of PFD. This situation is similar to the brain-fluid samples drying process. The blue curve is the model prediction while the orange curve comes from measured experimental data. The prediction values are valid in the CCA mode, during the first drying phase.

drying cycle including the data from the image analysis is provided in figure 5.4. The white circle is superposed to the contact area circle and its diameter value displayed on each sub-figure.

### 5.2.1.1 Discussion

We notice the model is in good agreement with the experimental values recorded. The first phase (CCA mode) lasts for 97 sec while the second phase (CWA mode) is shorter with 12 sec until the sample is dried. The model prediction becomes imprecise near the transition between the CCA and CWA mode; the model predicts

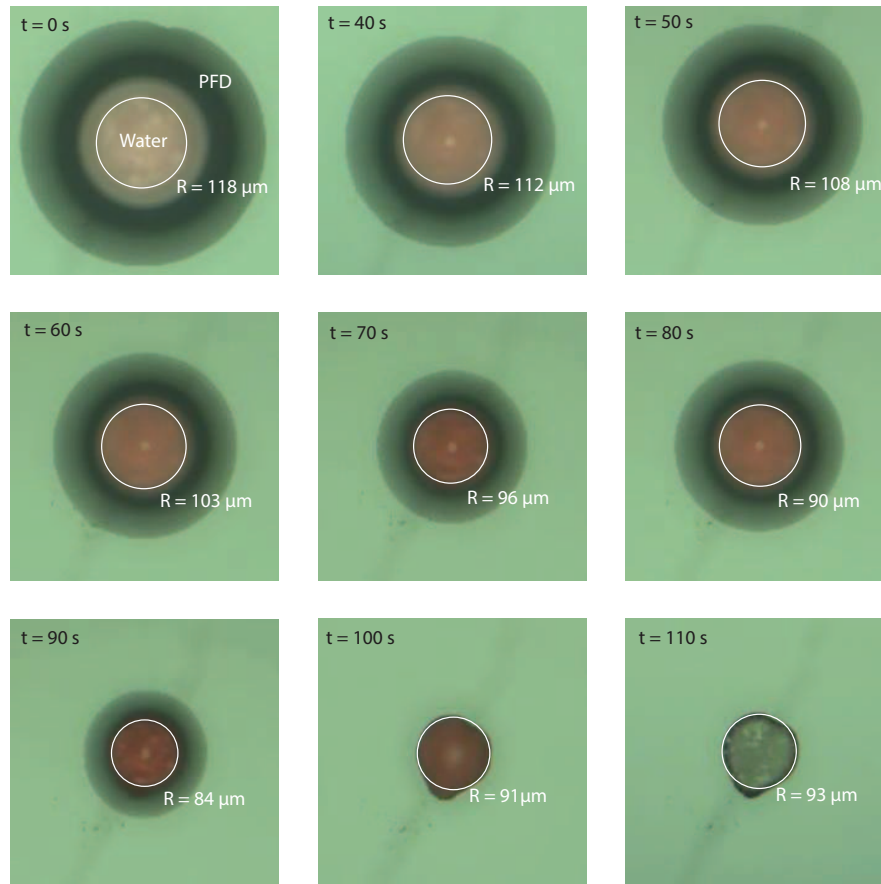


**Figure 5.4** Image sequence of a water droplet ( $V = 21$  nL) during evaporation on a parylene substrate, in presence of PFD. The wet area radius  $R$  (white circle) is measured at each time step. These experimental data were compared to the  $R$  values predicted by the model.

a lower  $R_f$  (final diameter) than the experimental values reached. We even notice the  $R_f$  measured increases instead of remaining stable. This difference might be explained by unanticipated surface tension phenomena occurring when the PFD disappears and the system transit from a "gas-liquid(water)-liquid(PFD)-solid" interface to a standard "gas-liquid-solid" interface. In this transition phase, the contact angle probably quickly transits from the initial obtuse angle  $\theta_0$  ( $= 135$  deg) to an acute angle. In a parylene-water-air systems, the contact angle has been reported to be equal to  $\theta = 89$  deg (Orejon et al. 2011). This transition would explain why the diameter increases until finding a new equilibrium position (droplet pinning) instead of remaining stable, as initially assumed by this model.

If the model correlates well with the data acquired, the influence of several

## Chapter 5. Neurochemicals Recording During Electrical Stimulation of Cerebral Tissues

---

parameters presented in this approach have not been tested. The influence of the initial droplet volume or the impact of the presence of NaCl in the brain-fluid samples are central ones. It might therefore be advised to repeat the experiment several times varying these parameters in order to validate its predictive behavior. This would further allow to provide a model confidence interval.

Similarly, the image analysis method implemented here is valid as a first approach. However, it can also generate imprecision when measuring  $R_f$  on the dried spot; especially in the final phase where the dried spot is never perfectly circular. Image analysis tools could be used here to precisely monitor the surface change which would be more relevant than extrapolating a diameter value. Another approach would have been to monitor the loss of mass over time instead of measuring the contact radius. This could have been implemented by placing the substrate on a precision lab scale as performed in initial studies (Picknett et al. 1977; Birdi et al. 1989). However, since our system combines two distinct fluid phases (PFD and water) both prone to evaporation, this approach is not implementable here as it would be difficult to distinguish the evaporation of the PFD from the evaporation of the water droplet.

### 5.2.2 *In Vivo* Species Diffusion Model

The model provided in the previous section allows to link the output of the detection method to the actual concentration of a brain-fluid sample. Now one may ask which ratio of the actual ECF concentration found in the cerebral tissues is indeed contained in the brain fluid samples. Unlike microdialysis, the *in vivo* ECF collection performed by the neural probe is similar to the push-pull approaches (W. H. Lee, Thomas R. Slaney, et al. 2013; T. R. Slaney et al. 2011; Kottegoda et al. 2002). In push-pull approaches a solution (or perfusate) is continuously perfused in the cerebral tissues whereas, at the same time, continuous liquid sampling is performed with an adjacent capillary. Thus the collected liquid is a fraction between the ECF-exchanged molecules and the perfusate content. Evaluating how much of the ECF is retrieved from the cerebral tissues is of major interest in our case, as the method involves perfusing liquid in the cerebral tissues.

In microdialysis, the ratio between the actual extracellular concentration and the dialysate is named "relative recovery" or "probe efficiency". This value depends on the flowrate of the dialysate but typically remains under 40 % at usual values (e.g. at  $1 \mu\text{Lmin}^{-1}$ ) (Chefer et al. 2009).

The diffusion equation can be employed in order to predict the relative recovery of the neural probe. The Fick's law (or diffusion equation) describes the diffusion of a solute in a viscous medium at steady state conditions. The relation postulates the flux goes from the high concentration region to the low concentration region, across the concentration gradient. The law reads:

$$\mathbf{J} = -D\nabla\phi \quad (5.9)$$

where  $\mathbf{J}$  is the the diffusion flux vector,  $D$  the diffusion coefficient and  $\phi$  the concentration of the solute. Under the assumption of low Re number, the diffusion of spherical particles through a liquid coefficient is defined by the Stokes-Einstein relation:

$$D = \frac{k_B T}{6\pi\eta a} \quad (5.10)$$

with  $k_B$  the Boltzmann constant ( $= 1.38064852 \times 10^{-23} \text{ JK}^{-1}$ ),  $T$  the temperature,  $\eta$  the dynamic viscosity and  $a$  the particle radius. In steady state conditions, the continuity equation reads:

$$\frac{\partial\phi}{\partial t} = -\nabla \cdot \mathbf{J} \quad (5.11)$$

which can be written, with the precedent definition given in 5.9:

$$\frac{\partial\phi}{\partial t} = -\nabla \cdot (-D\nabla\phi) = D\nabla^2\phi \quad (5.12)$$

and which expresses the variation of the solute concentration over time.

In the following we use this mathematical description to evaluate the relative recovery of the neural probe. In particular, the evaluation of the time taken by an analyte to diffuse from the cerebral tissues to the sampling inlet of the neural

## Chapter 5. Neurochemicals Recording During Electrical Stimulation of Cerebral Tissues

probe is of major interest. We will consider here a spherical drop of perfusate with a known radius  $r_{\text{drop}}$  permanently in place in the cerebral tissues as shown in figure 5.5 (a). As a first approach, we will neglect any sources or sinks present in the system. This situation can equivalently be represented by a mono-dimensional model along the  $x$  axis considering the probe tip as an infinitely small sampling point at the position  $x = 0$ . At initial conditions, the perfusate mean concentration of an analyte  $i$  contained in the brain is zero. At the position  $x = r_{\text{drop}}$ , the analyte concentration rises to  $\Phi_i$  and remains constant in an infinitely long reservoir representing the cerebral tissues.

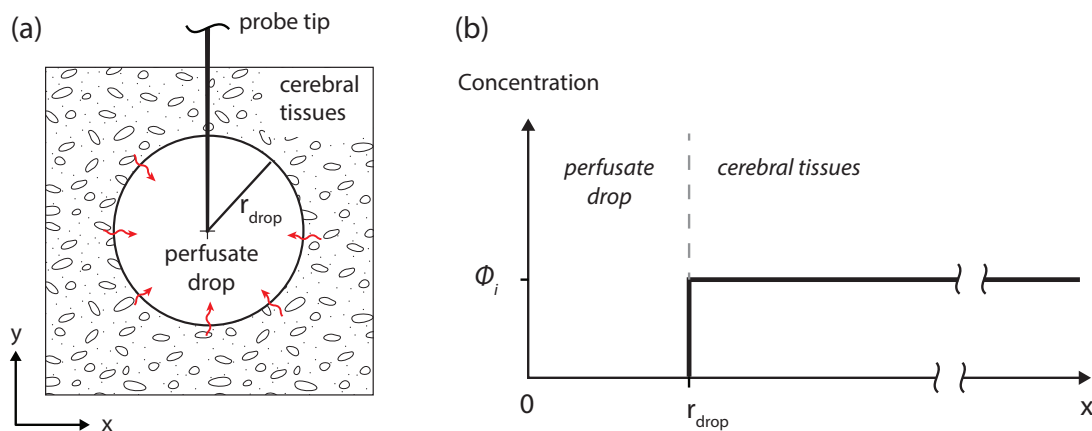


**Figure 5.5** Diffusion model from the cerebral tissues to the neural probe inlet. (a) Bi-dimensional representation of the system including the perfusate drop of radius  $r_{\text{drop}}$  as well as the probe tip inserted in cerebral tissues. (b) Mono-dimensional representation (along the  $x$  axis) of the initial concentration distribution of an analyte  $n$  in the same system. At the position  $r = r_{\text{drop}}$ , the analyte concentration rises to  $\Phi_i$ , its concentration in the brain.

Using the differential equation 5.12 in the mono-dimensional case with the parameters defined in table 5.2 we can predict the diffusion of a Ca ion in the perfusate drop (Lide 2004; Weast 1989). We assumed here the perfusate drop is a pure water spherical volume of radius  $r_{\text{drop}} = 100 \mu\text{m}$  (e.g. of volume = 4.2 nL). The following boundary conditions were used in the model: (i) the molecular diffusion flux was fixed to zero at  $x = 0$  ( $\frac{\partial \phi}{\partial x} = 0$  at  $x = 0$ ) and (ii) an infinite reservoir of diffusing species was considered at  $x \geq r_{\text{drop}}$ . The resulting concentration curve  $\Phi$  (relative to  $\Phi_{Ca\infty}$ , the Ca concentration in the tissues at an infinite distance from  $x = 0$ ) at initial condition ( $t = 0$ ) and its evolution over time (from  $t = 0.1$  s to  $t = 100$  s) is provided in figure 5.6. Ca concentration in the

**Table 5.2** Parameters used in the diffusion model to predict the diffusion of ionic species (Ca, K, Mg) from the cerebral tissues towards the probe inlet.

parameter	value	units
$r_{\text{drop}}$	$100 \times 10^{-6}$	m
$a_{Ca}$	$231 \times 10^{-12}$	m
$a_K$	$280 \times 10^{-12}$	m
$a_{Mg}$	$173 \times 10^{-12}$	m
T	37	°C
$k_B$	$1.380648 \times 10^{-23}$	$\text{JK}^{-1}$
$\eta$	$6.915 \times 10^{-4}$	Pas

perfusate drop (left to the dashed grey line) tends to increase and equalize  $\Phi_{Ca\infty}$  over time. After 100 s, the concentration at the sampling spot ( $x = 0$ ) reaches 85 % of  $\Phi_{Ca\infty}$ , the concentration outside of the perfusate drop, in the cerebral tissues at an infinitely distant location. Under the previously defined conditions the time to reach a relative recovery of 50% and 85% amounts to 7.6 s and 96.3 s, respectively. Table 5.3 compares the time needed to reach these relative recovery values for Mg and K ionic species. We notice significant differences regarding the time to reach a relative recovery of 85 % which is explained by the difference in size of the considered ionic species.

**Table 5.3** Predicted time to reach 50 % and 85% relative recovery in the sampling process as a function of the considered species.

Species	time to 50 % rel. recovery	time to 85 % rel. recovery
Mg	5.67 s	72.13 s
K	9.18 s	116.75 s
Ca	7.57 s	96.31 s

## Chapter 5. Neurochemicals Recording During Electrical Stimulation of Cerebral Tissues

---

### 5.2.2.1 Discussion

The model proposed in this section assumed the diffusion took place in water, which is reasonable for the perfusate drop domain but less appropriate for the cerebral tissues domain. In the cerebral tissues the diffusion coefficient is reduced compared to diffusion in water since the extracellular space comprises narrow spaces and tortuosity limiting molecules motions (without even considering loss of molecules through cellular uptake and binding or blood-brain barrier absorption). The hindrance to diffusion in nervous tissues is generally characterized using the tortuosity  $\Lambda$  which is the square root of the ratio between the free diffusion in water  $D$  and the effective diffusion coefficient  $D^*$  (Harris et al. 1948; Safford 1977):

$$\Lambda = \sqrt{\frac{D}{D^*}} \quad (5.13)$$

The tortuosity is reported to range from 1.4 to 1.7 meaning  $D^*$  accounts for a half to one third of  $D$ , the free diffusion in water (Sykova et al. 2009). From these values we can extrapolate that the time to reach a given concentration at the sampling inlet should be longer than predicted by the model as the diffusion in cerebral tissues is hindered by the tortuosity. The infinite reservoir considered in the model would therefore supply slower the perfusate drop. Dividing the system in two spatial domains with two distinct diffusion coefficients, one for the perfusate drop and one for the cerebral tissue, could allow to enhance the model precision, although this description won't be implemented here.

Another simplification made in this analysis is the omission to consider the sodium contained in the perfusate drop. In term of viscosity, the NaCl 0.9 % is almost similar to pure water, which should have a negligible impact on the model. For the Na ion though, the concentration gradient will be lower than for any other species and the molecular diffusion driving the ions towards the perfusate drop lower. Although not implemented here, the Na distribution change over time could be more precisely evaluated with this model by changing the initial condition its concentration distribution over  $x$ .



This analytical model also allows to define an appropriate sampling frequency when collecting ECF molecules from the cerebral tissues. If the perfusate drop in the tissues is spherical and of radius  $r_{\text{drop}} = 100 \mu\text{m}$  as assumed in this model, the fraction of  $\frac{\Phi}{\Phi_{Ca\infty}}$  collected in the sampling probe after 100 ms represents only 0.006. Consequently the sampling resolution can be largely decreased in order to retrieve a larger fraction of the actual cerebral tissue Ca concentration in the samples. It is therefore recommended to adjust the sampling period to 30 s ( $f = 0.003 \text{ Hz}$ ) in order to reach relative recovery values above 75 %, which is already much higher than achieved with microdialysis approaches under standard sampling conditions (Kennedy 2013).

**Chapter 5. Neurochemicals Recording During Electrical Stimulation of Cerebral Tissues**

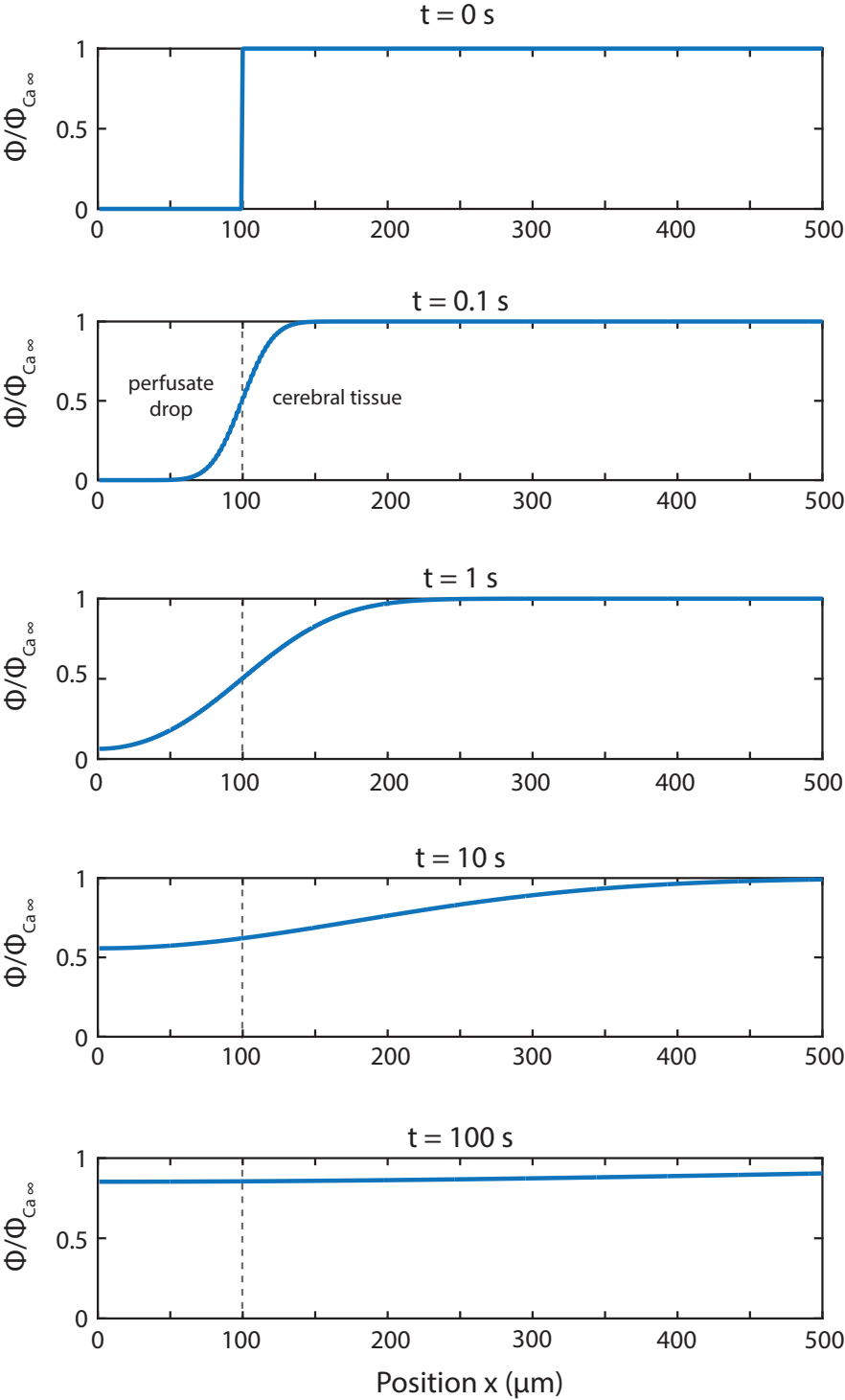


**Figure 5.6** Time evolution of the Ca ions concentration (relative to  $\Phi_{Ca\infty}$ , the Ca concentration at an infinite distance from  $x = 0$ ) in the perfusate drop. The grey dashed line limits the perfusate drop domain from the cerebral tissue domain. At initial condition ( $t = 0\text{ s}$ ), the perfusate drop (radius  $r_{\text{drop}} = 100\text{ }\mu\text{m}$ ) contains no Ca ions. Then the Ca concentration in the perfusate drop increases with time and tends to equalize  $\Phi_{Ca\infty}$ .

## 5.3 Simultaneous Neurochemicals Sampling and Electrical Stimulation

In chapter 4 was demonstrated the *in vivo* droplet collection of neurochemicals using exclusively the microfluidic functions of the neural probe. In this section we propose to electrically stimulate the cerebral tissues while continuously collecting neurochemicals. The objective is to use the neural probe as a trigger of neurochemical activity. Such a combined process could be of major interest for the neuroscientists since direct correlation between neurochemical and electrical activity in cerebral tissues will be observed at unprecedented temporal and spatial resolution.

### 5.3.1 Material and Methods

#### 5.3.1.1 Neural probe

The *in vivo* measurements were performed with a slightly modified version of the neural probe compared to previously described in chapter 4, section 4.2.1. An electrical connector by which the neurostimulation signal is transmitted to the probe tip and the cerebral tissues was bonded to the probe proximal contacts using conductive glue (Epotek H20E, Epoxy technology Inc.). The bonding was further secured using Epoxy glue joining the connector base to the neural probe proximal surface. This connector contacts 8 electrical tracks, each connected to the distal electrodes according to the pairing chart provided in appendix A.1. In term of microfluidics, the same pressure driving equipment units were used (2x MFCS-MZ, Fluigent). PFD was used as the carrier fluid. Two fused silica capillaries (ID =  $250\mu\text{m}$ , OD =  $360\mu\text{m}$  and length = 40 cm) were assembled to the probe via 2 microfluidic connectors (P-771, IDEX HS). This solution allowed for an efficient disconnection and replacement of the collection capillary. The neural probe also includes a perfusion capillary (ID =  $50\mu\text{m}$  and OD =  $196\mu\text{m}$ ) employed to inject perfusate in the tissues (saline solution 0.9 % NaCl) during the

## Chapter 5. Neurochemicals Recording During Electrical Stimulation of Cerebral Tissues

sampling process. Figure 5.7 provides an overview of the neural probe including the new elements previously described. We notice the neural probe is fixed to the interface unit bottom part to facilitate manipulation and fixation on the stereotactic arm.

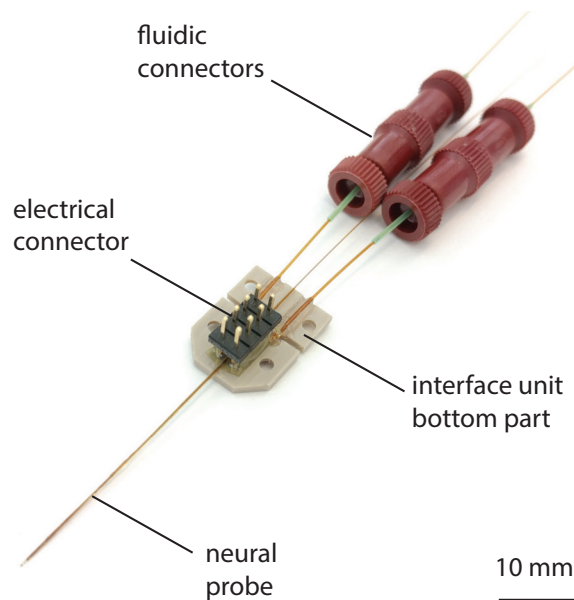


**Figure 5.7** Neural probe including the electrical and fluidic connectors. The device is bonded to the bottom part of the interface unit which facilitates handling during *in vivo* experiments (fixation to the stereotaxic frame).

### 5.3.1.2 Electrical Stimulation

An external pulse generator (Model 2100, A-M system) connected to the neural probe was used to neuromodulate the cerebral tissues in direct proximity with the device distal tip. Train of biphasic pulses of  $300\ \mu\text{A}$  amplitude (peak to peak) and 2 ms duration at a frequency of 60 Hz were delivered during 60 sec as detailed in appendix A.2. The signal was delivered by the largest stimulation electrode (diameter  $d = 150\ \mu\text{m}$ ) of the probe distal tip. The counter electrode consisted in a Pt wire electrode (diameter  $D = 100\ \mu\text{m}$ ) inserted in the superior region of the cortex through the craniotomy hole.

## 5.3. Simultaneous Neurochemicals Sampling and Electrical Stimulation

---

### 5.3.1.3 *In Vivo* Experiment

Three Sprague Dawley female rats (Charles river laboratory) weighting between 245 g and 250 g were included in this experiment. The measurements were performed under Isoflurane anaesthesia (4 % at induction, 2 % for maintenance). An analgesia by buprenorphine (Temgesic, 0.1 mg/kg, injected under the skin of the neck) was performed on each subject before any surgical act. The subjects were fixed in a stereotactic frame and the stereotactic coordinates were set to + 0.5 mm anterior, + 3.0 mm lateral and - 5.0 mm ventral from bregma with the toothbar set to - 3.3 mm to reach the brain striatum. After the craniotomy (hole diameter 0.8 mm), the neural probe was inserted slowly in the tissues while injecting the saline solution through the perfusion capillary at a constant flow rate of 50 nL/min in order to avoid any clogging issues. Two minutes after the target area was reached, the droplet sampling system was turned on. A positive pressure  $P_{in} = 50$  mbar and a negative pressure  $P_{out} = -400$  mbar was applied (relatively to the local pressure) during 20 min. 10 s prior to starting the droplet collection sampling, the saline solution was injected at a flow rate of 100 nL/min. The droplet sampling process was then started. 1 min after, an electrical stimulation was applied to the cerebral tissues for a period of 1 min (while maintaining the droplet sampling in parallel). 11 min after the beginning of the droplet sampling, electrical stimulation was applied again for a period of 1 min. The droplet sampling procedure was continued for an additional 9 min and stopped 21 min after its beginning. The saline perfusion was maintained during the entire sampling procedure. After the phase, the probe was slowly retracted from the tissues and the animal sacrificed. At the end of the experiment, the collection capillary in which the droplets were collected was disconnected and stored at - 20 °C. Particular attention was provided to maximize the animals well-being during the experiment. All the procedures were performed in accordance with the local animal care authorities.

## Chapter 5. Neurochemicals Recording During Electrical Stimulation of Cerebral Tissues

---

### 5.3.1.4 Analysis Method

The analysis of the collected brain-fluid samples was performed using an ICP mass spectrometer equipment (7700 series ICP, Agilent technologies) coupled to a solid state laser ablation system (NWR213, ESI) which comprises a focused Nd:YAG system used to laser ablate the sample material. The following parameters were set; laser energy density  $4.27 \text{ J/cm}^2$ , energy output 23 %, laser focus spot size  $50 \mu\text{m}$ , laser pulse duration 20 ns, repetition rate 20 Hz, scanning speed  $50 \mu\text{ms}^{-1}$ , carrier gas flow rate 800 ml/min and MS acquisition rate 1 Hz. After the *in vivo* collection, the brain-fluid samples were distributed on a similar platform than the previously described parylene base plate (chapter 5, section 4.2.4). The parylene base plate comprised 20 holes in a row, each of  $20 \mu\text{m}$  diameter, drilled using an Excimer laser (Optek LSV3). The brain fluid samples were distributed and dried on this platform. Two-dimensional imaging was performed on the dried spots, each laser pass being separated by  $50 \mu\text{m}$ , giving a pixel resolution of  $50 \times 50 \mu\text{m}^2$ . All data were visualized using MSiReader and processed using Matlab (Robichaud et al. 2013).

### 5.3.2 Results

The samples extracted from the cerebral tissues comprised 3 sets of droplet trains. The 1<sup>st</sup> set included 16 brain-fluid samples, the 2<sup>nd</sup> 17 while the 3<sup>rd</sup> included 11 brain-fluid samples. The ICP mass spectrometry analysis on these samples revealed the presence of Na, Mg, K and Ca in the brain-fluid samples in significant relative abundance for every set of droplets. Traces of Mn, Fe and Cu metals were found as well, the signal of Cu being in general stronger than the other ones. No traces of Hg were found in any samples, as expected, which constitutes a negative control. These results are similar than found in chapter 5 which consolidate the validity of our findings. Figure 5.8 shows the relative abundance maps for the elements Na, Mg, K and for every set of extracted droplet trains (only the 8 first droplets are shown).

As it can be observed on the heat maps of figure 5.8, the spatial resolution is

### 5.3. Simultaneous Neurochemicals Sampling and Electrical Stimulation

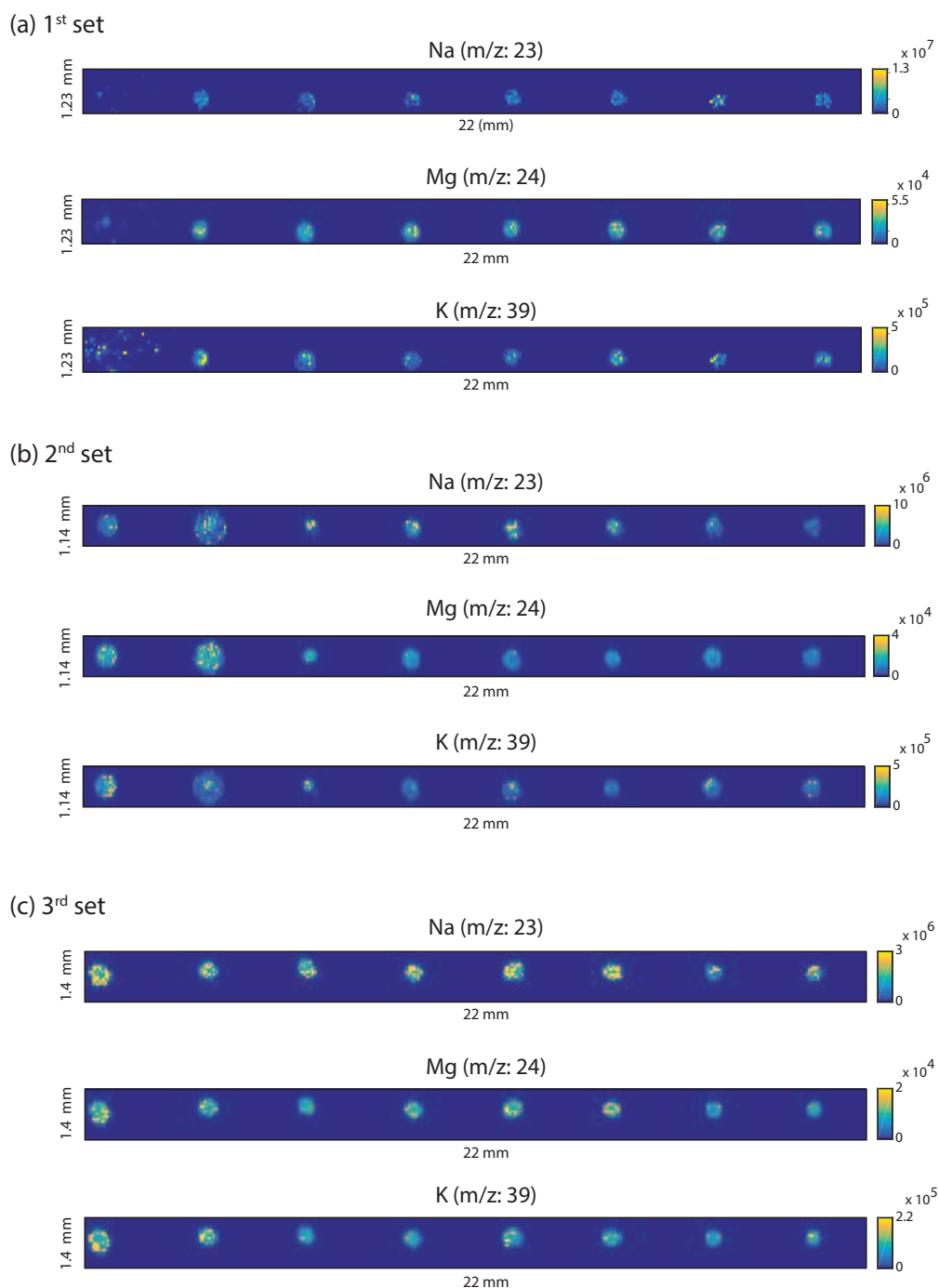


**Figure 5.8** Relative abundance of Na, Mg and K found in the brain-fluid samples after ICP-MS detection. The results are provided for 3 successive sets of independently collected brain-fluid samples ((a), (b) and (c)). (Only the first 8 brain-fluid samples are shown here)

drastically enhanced compared to the results from chapter 5 (figure 4.4). A detailed three-dimensional plot of a single dried spot (second dried spot) is

## Chapter 5. Neurochemicals Recording During Electrical Stimulation of Cerebral Tissues

provided in figure 5.9. The peak height is proportional to the relative abundance of the Mg element over the dried spot surface. We notice the signal intensity distribution is relatively homogeneous over the dried spot surface; no coffee-stain effect is detectable.

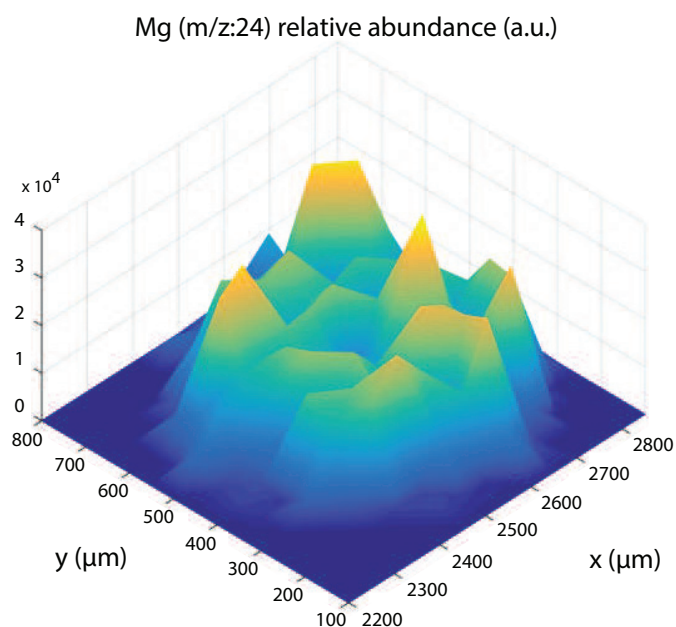


**Figure 5.9** Selected dried spot from the second set of samples represented in 3 dimensions. Mg relative intensity is represented on the vertical axis.

In figure 5.10 is provided the detection results of a complete time sequence including the two periods of electrical stimulation. Figure 5.10 (a) shows the relative abundance for the Mg on the 16 dried spots of the first set of samples. The time lapse between two successive brain fluid samples was evaluated at  $t = 100$  s. Consequently, the maximum relative abundance peak value extracted for K, Na, Mg and Pt is provided as a function of the time in figure 5.10 (b). These plots refer to the temporal *in vivo* evolution of the neurochemicals over a sampling period of 15 min with two electrical neurostimulation periods of 1 min (between sample 2 and 3 and between 12 and 13). We observe that K relative intensity significantly increased as a response to the electrical stimulation while Na and Mg remained stable.

Interestingly, Pt relative abundance also increases during both periods of neu-



### 5.3. Simultaneous Neurochemicals Sampling and Electrical Stimulation

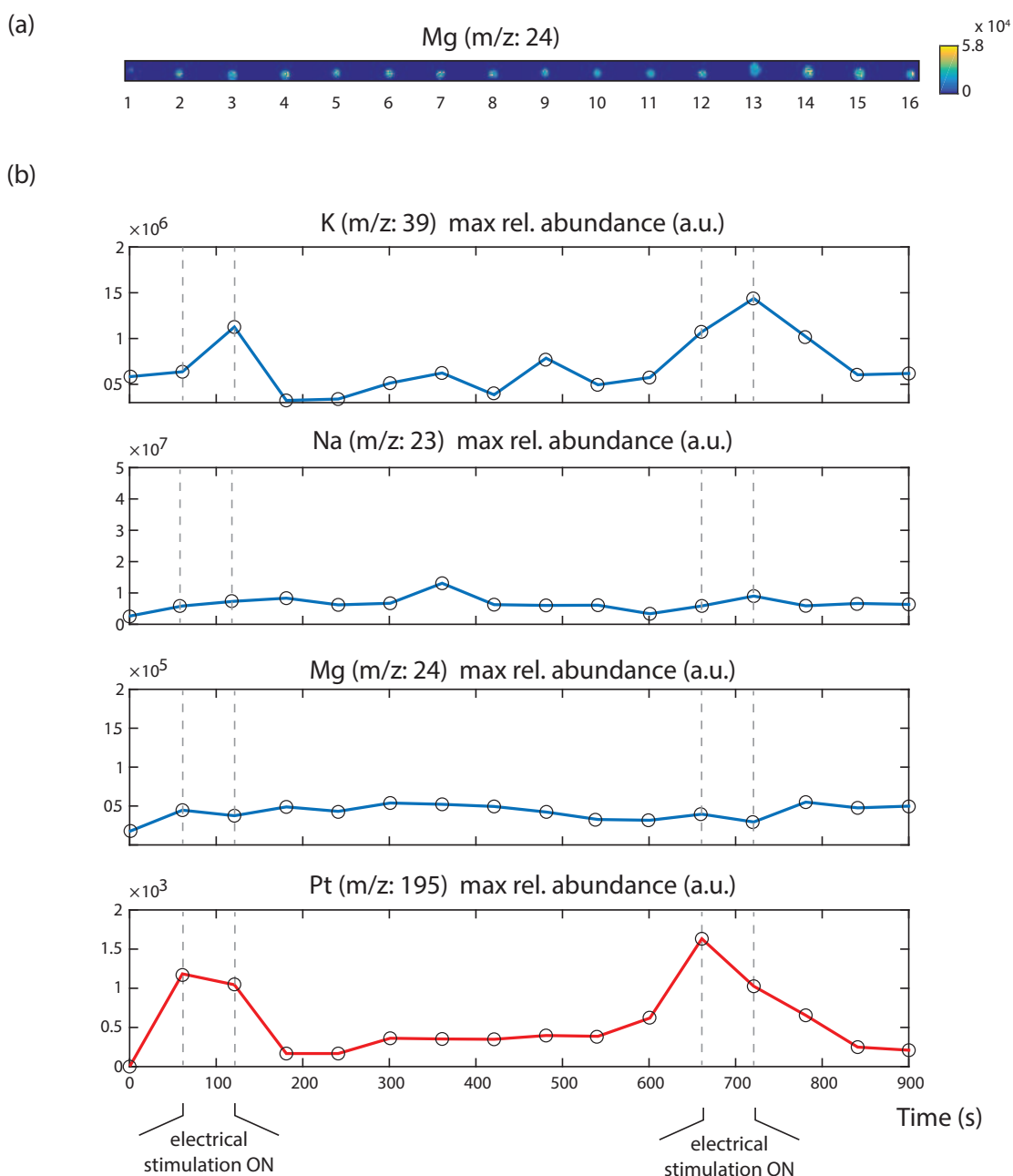


**Figure 5.10** Detection results of *in vivo* collected brain-fluid samples (1<sup>st</sup> set) with simultaneous electrical neurostimulation of the tissues. (a) Mg relative abundance distribution found in the collected brain-fluid samples using ICP mass spectrometry. This set comprised 16 brain-fluid samples each separated by a lapse of time of 60 s. (b) Temporal evolution of the maximum relative abundance found in each brain-fluid sample for K, Na, Mg and Pt. The periods of electrical stimulation as defined by the experimental protocol are provided at the bottom of the figure.

## Chapter 5. Neurochemicals Recording During Electrical Stimulation of Cerebral Tissues

---

rostimulation, in correlation with the K increase. It is assumed that during stimulation Pt particles are released in the tissues which would explain the reported increase. This is an important result which confirms the stimulation periods are indeed synchronized with the applied stimulation periods as defined by the experimental protocol (1 min stimulation at  $t = 1$  min and  $t = 11$  min). We can therefore consider the Pt trace as a "marker" of the stimulation periods.

Apart from K and Pt, no other elements showed a significant answer to the neurostimulation phases (the elements assessed included Ca, Mn, Fe, Cu and Zn). Although not provided here, similar results were observed in each of the 3 sets of brain-fluid samples. In particular, the correlation of the electrical stimulation periods with K increase and Pt increase is reported in every set of results which further validates our findings.

### 5.4 Discussion

Most cells maintain an internal environment negatively charged relative to the extracellular space. This is the case for neurons which keep a resting potential set to -70 mV as reported in the experimental work of Hodgkin and Huxley on nerve conduction (Hodgkin and Huxley 1952). This negative potential is maintained thanks to the ion pumps and voltage-gated ion channels;  $K^+$  ions are pumped in the cell while  $Na^+$  ions are removed continuously resulting in a stable resting membrane state. When an AP propagates along an axon, the neuron cell membrane goes through a depolarization phase (internal potential starts to increase) and reach, at the AP peak, a positive potential of +40 mV. During this phase, the  $Na^+$  channels are open and a  $Na^+$  influx is observed towards the inner compartment of the axon. After this peak phase, the  $K^+$  channels open and the  $K^+$  ions consequently leave the axon and penetrate the extracellular space; the inner potential of the neuron therefore decreases to reach a hyperpolarized state of -75 mV, 5 mV under the resting potential. This state persists for a few milliseconds before the  $K^+$  channels closes and the neuron stabilize at its resting potential again.

The electrical stimulation applied during this experiment probably induced a depolarization of the neurons followed by a hyperpolarization. In particular it seems the neurons are maintained in a hyperpolarized-locked state. This would explain the significant rise of extracellular K signal measured simultaneously with the stimulation periods while the Na<sup>+</sup> signal remained stable (and didn't decrease due to depolarization as expected). Prior to hyperpolarization, the neuron should experience a depolarization phase accompanied with a local extracellular depletion of Na<sup>+</sup> ions. In our measurements we didn't detect such a depletion though. This is probably explained by the very high Na<sup>+</sup> content found in the ECF (145 mmol) which renders small variations hardly detectable. In comparison, K<sup>+</sup> concentration in ECF is 30 times lower with (4.5 mmol) (Boron et al. 2017). It is to mention Na detection is further hindered by the local injection of a saline perfusate during the sampling which tends to constantly renew the extracellular Na content.

It is interesting to put these results in perspective with the DBS treatment for PD and Essential Tremors (ET). In this therapy, electrical stimulation at precise brain locations (e.g. STN and Globus Pallidus (GPi)) is delivered which drastically reduces the symptoms of these neurological disorders. The therapeutic mechanism behind the treatment is not clearly understood although it is clinically very effective. One of the first stated mechanism was that the stimulation produced an inhibitory effect on the stimulated target which was well aligned with the improved symptoms observed after thalamotomy or pallidotomy (surgical ablations) (Montgomery et al. 2008; McIntyre et al. 2004). Although this hypothesis is disputed and that many other mechanisms of action have been proposed as well, this would go in the same direction than our results stating that the electrical stimulation pattern applied tends to hyperpolarize and "paralyze" the signals propagation of the direct neural environment around the probe electrode. As a future perspective of this technology, using the recording electrodes included on the device could help to decode the functional mechanism lying behind electrical stimulation. Indeed, this would provide valuable information regarding the electrical activity (firing rate) of a stimulated neuronal network and thus improve our understanding of the mechanism involved here.

## Chapter 5. Neurochemicals Recording During Electrical Stimulation of Cerebral Tissues

---

Finally, it is interesting to note the extension of the electrical stimulation in the tissues was probably limited to roughly a half sphere of 1 mm diameter over the stimulation electrode (radius =  $75\ \mu\text{m}$ ) as evaluated in section 2.1.3.2 of chapter 2 (Newman 1966). The level of stimulation performed on the neural probe was far under the safety limit as defined per the study of Shannon (R. V. Shannon 1992). We therefore didn't expect having produced any damages to the neurons during the stimulation periods.

### 5.5 Conclusions

In the first part of this chapter was provided a model describing the droplet evaporation behavior as well as a model characterizing the species diffusion into the perfusate drop. In summary, the outcomes of this first section are:

- An analytic description validated experimentally of the mixed behavior observed during droplet evaporation in presence of PFD (first CCA mode then CWA mode)
- A description of the species diffusion which takes place in the perfusate drop. This model allows to link the droplet sampling rate to the relative recovery of the neural probe

With these two models, it is now possible to retrieve the actual tissues concentration in direct proximity to the probe sampling inlet from the detection results, even if the dried spot is partially analyzed.

The second section of this chapter presented a method for simultaneously record neurochemical activity and electrically stimulate in the cerebral tissues in rats brain. Three sets of brain-fluid samples were successfully collected and analyzed using ICP mass spectrometry. The main outcomes of this second *in vivo* study are:

- The  $\text{K}^+$  ion concentration significantly increased during electrical stimulation periods. This result was confirmed on each of the 3 implanted

animals.

- The Pt signal significantly increased during electrical stimulation as well, which makes it a good "marker" of the stimulation periods.
- The cerebral tissues seemed to be placed in a hyperpolarized state as a reaction to the electrical stimulation, which is consistent with the  $K^+$  increase measured.

It is equally important to note that other species have been found in significant quantities on the samples analyzed. In particular Na, Mg, K and Ca were found in every sets of droplets, confirming the results of the precedent *in vivo* study results (chapter 4). Metal traces were also detected for the Fe, Cu and the Zn although the signal was generally lower than reported in chapter 4.



# Chapter 6

## Conclusions and Future Perspectives

The objective of this work is to contribute to the field of neurotechnology and neurophysiology by providing new strategies of interaction with the cerebral tissues. A major effort was provided to combine an efficient fluidic collection system with an electrical stimulation platform on a same device, using microtechnology approaches. Such a system allows to provide a more reliable technique for performing neurophysiological studies in comparison with existing solutions. In summary, this thesis brought the following outcomes:

- **Neural probe microfabrication**

Microfabrication methods have been shown to enable the production of a minimally invasive device (needle-like) comprising a microfluidic network (channel cross sections:  $40 \times 80 \mu\text{m}^2$ ) as well as microelectrodes. The use of polymer materials such as polyimide combined with noble metals (platinum and titanium) allowed to produce a flexible, biocompatible neural probe. The fabrication approach enabled to integrate a compact microdroplet generation system at the distal tip of the probe. In addition to being compatible with high temporal resolution sampling of *in vivo* fluid, this sampling mechanism is proposed as a novel approach solving Taylor dispersion that usually occurs in non-segmented flow.

- **Device performances**

The *ex vivo* assessment of the main neural probe functions allowed to guarantee that its behavior was compatible with the intended field of use. In particular, the mechanical stiffness of the probe was shown to be high enough to withstand penetration in cerebral cortex while remaining flexible. The electrical behavior of the probe was thoroughly assessed by impedance spectroscopy and the probe was experimentally demonstrated to reach a collection frequency as high as 6 Hz (meaning one droplet every 170 ms). This result largely overcomes the typical temporal resolution reached by microdialysis (ca. 10 min) and renders the system compatible with the time range of fast synaptic signal transmission (< second).

- ***In vivo* pilot animal study**

The neural probe was successfully tested *in vivo* as part of a pilot animal trial performed on rats. The device was inserted in the Striatum of a rat brain and collected brain-fluid samples organized in droplet trains. The implantation procedure and the system functions (such as the fluidic control) were shown to be well compatible with the surgery setup. Histological study performed on brain tissue sections post implantation demonstrated minimal tissue damage around the probe track.

- **A platform for samples analysis**

A custom analysis platform enabling the detection of the brain-fluid samples was developed. The proposed approach consisted in the sequential distribution of the collected samples on a microfabricated target plate, maintaining spatial separation and order between droplets, thus guarantying the time-history of the sampling. ICP mass spectroscopy allowed to detect Na, Mg, K and Ca in significant quantities, reflecting the neurochemical content of the brain extracellular space. The method was further proven to be quantitative and allowed to measure consistent concentration values for Fe, Cu and Zn. The established method of detection gave access to a broad range of information regarding the neurochemical state of the implanted medium.



---

- **System modeling**

A mathematical description of the droplet drying process and the *in vivo* species diffusion provided a method for retrieving the actual tissue concentration (volume concentration) from the analysis output (surface concentration). The dependence between the probe relative recovery and the droplet sampling rate was assessed using the models. With our system, relative recovery which overpasses 75 % is predicted by adjusting the sampling period to 30 s (0.03 Hz).

- **2<sup>nd</sup> *In vivo* animal study**

A second *in vivo* animal study involving 3 different subjects allowed to record the neurochemical activity of the cerebral tissues during 20 min including during electrical stimulation periods. The results demonstrated an increased neurochemical activity in response to the electrical stimulation. In particular, a rise in the K<sup>+</sup> ion concentration during electrical stimulation was confirmed in each of the 3 implanted animals. The electrical stimulation seem to have set the neurons in a permanent hyperpolarized state, provoking a K<sup>+</sup> ions efflux out of the cells.

The high temporal resolution was defined as a major specification of the neural probe. This placed considerable constraints on the design process as well as on the microfluidic driving control. The mathematical models implemented in chapter 5 highlighted the diluting effect of the perfusion on the species present in cerebral tissues; indeed, the larger the exchange zone (or the perfusate drop), the lower is the probe relative recovery. This pointed out the existing tradeoff between the temporal resolution and the desired relative recovery value. At usual dialysate flow rates (e.g. 1  $\mu$ L/min), standard microdialysis relative recovery values remain under 40 % (Chefer et al. 2009). The developed *in vivo* diffusion model predicts a relative recovery above 50 % with a sampling frequency set to 0.1 Hz leading to a temporal resolution of 10 s. The latter is largely above the actual microdialysis performance (c.a. 10 min) which, today, is mainly limited by the resolution of the analysis method (Kennedy 2013). However, the model description did not consider the continuous renewal of the perfusate drop; the system was assumed to be in steady state which is an approximation. The model prediction could

## Chapter 6. Conclusions and Future Perspectives

---

be further improved by considering a source and a sink nearby the sampling spot. Considering these elements, one may claim that a high temporal resolution sampling only makes sense if the perfusion drop volume is drastically decreased (which implies a tight link with the tissues) and/or the perfusion flow rate is maintained at a slow level.

The material choices had an impact on the mechanical behavior of the probe shank. The use of polymers (Polyimide, SU-8 resin) allowed to provide a rather flexible structure which was moreover proven to be rigid enough to be inserted in the cerebral tissues. In case of a long-term implantation use, mechanically flexible brain interfaces are known to reduce tissue inflammation and fibrosis, as they better match the viscoelastic properties of cerebral tissues (Mercanzini, Colin, et al. 2009; Minev et al. 2015). Yet, in our study, the neural probe was used in an acute application with a maximum implantation time of two hours. One may argue that a rigid structure would have been more appropriate and lead to the same results. Silicon-based probe including microchannels and microelectrodes have indeed been used for drug delivery applications (J. Chen et al. 1997; H. J. Lee et al. 2015). The mechanical rigidity of these solutions facilitate the physical connection of external equipment on the probe (e.g. electrical and fluidic interfaces). However, the brittle characteristic of silicon renders it poorly compatible with handling during implantation; the sharp edges of silicon also remain a traumatic aspect for the tissues. Another point relates to the droplet sampling process. The surface properties of the microchannel play a decisive role for the proper handling of a droplet-segmented flow. Silicon microchannels are generally created by Deep-Reactive Ion Etching (DRIE) resulting in rather hydrophilic-like surface properties. This situation is not recommended in our case since aqueous droplets are carried in an oil phase (PFD) which requires hydrophobic channel walls. With respect to all these aspects, the choice of polymer-based and mechanically flexible materials seems reasonable.

The simultaneous electrical stimulation and neurochemical sampling allowed to detect significant changes in  $K^+$  concentration in the cerebral tissues. As a first approach, we computed the maximum relative abundance found over each dried spot and analyzed these data. Computing the mean dried spot intensity over

the dried spot surface instead could certainly contribute to refine the analysis by averaging the occasional non-uniform distribution of the concentration peaks. Additionally, a quantitative analysis of the data should allow to derive the surface concentration values (dried spots) leading to a reasonable estimation of the actual cerebral tissue volume concentration. This would request a supplementary experimental step to define the calibration curves but would also offer valuable information.

## 6.1 Outlooks

The main contribution of this thesis is to provide a device for the precise recording of neurochemical activity in response to electrical stimulation with a dedicated analytic platform. The extension of the detection method to Matrix Assisted Laser Desorption/Ionisation (MALDI) mass spectrometry would represent a significant increment, giving access to a large number of biomolecules including proteins and neurotransmitters.  $\alpha$ -Synuclein is a presynaptic protein which may contribute to the pathophysiology of PD by its a toxic effect ultimately leading to the death of dopaminergic neurons (Stefanis 2012). The *in vivo* detection of  $\alpha$ -synuclein concentration evolution over time in electrically stimulated PD animal models would certainly provide interesting perspectives regarding disease pathophysiological mechanisms and the impact of DBS.

The monitoring of neurotransmitter concentration changes locally triggered by electrical stimulation would be equally interesting for the early detection of neurological disorders. In particular the Da level in response to stimulation at several time steps of PD evolution could lead to a better characterization of the disease. Such new approaches could open the doors to the development of better diagnostic tools leading to earlier disorder detection. These approaches could have a profound medical impact, as early PD treatment is more effective and result in a prolonged quality of life for the affected patients (Noyes et al. 2013; Pahwa et al. 2010; Hauser 2009).

On the actual device, the sample analysis is performed post implantation, in

## Chapter 6. Conclusions and Future Perspectives

---

a second step. In a near future, it will probably be possible to implement the neurochemical detection in real time, on the same device. This could lead to more efficient electrical stimulation therapy of the CNS and PNS by using a closed-loop system control. A major step towards this direction would be to adjust the electrical stimulation pattern delivered in a DBS target such as the STN while optimizing the elicited neurochemical response with the best therapeutic effect.

Another major clinical application of this technology is related to the analysis of seizure focal zones during epilepsy treatment. Surgical management of epilepsy involves electrical brain mapping performed using electrodes to detect the focal position of the seizures and their relative proximity to important neural functions (speech, vision, sensory, motor, etc). The use of the neural probe intraoperatively could here facilitate the localization of the seizure focal point by detecting biomarkers associated with epilepsy (Jerome et al. 2014). Such approach would allow the surgeon to be more precise and thus preserve larger zones of functional cerebral tissues resulting in a direct benefit for the patient.

# Bibliography

- Ali-Cherif, Anaïs et al. (2012). “Programmable Magnetic Tweezers and Droplet Microfluidic Device for High-Throughput Nanoliter Multi-Step Assays”. In: *Angewandte Chemie International Edition* 51.43, pp. 10765–10769.
- Altuna, A., E. Bellistri, et al. (2013). “SU-8 based microprobes for simultaneous neural depth recording and drug delivery in the brain.” In: *Lab on a chip* 13.7, pp. 1422–30.
- Altuna, A., L. Menendez de la Prida, et al. (2012). “SU-8 based microprobes with integrated planar electrodes for enhanced neural depth recording.” In: *Biosensors and Bioelectronics* 37.1, pp. 1–5.
- Anastassiou, Costas A. et al. (2006). “Subsecond Voltammetric Separation between Dopamine and Serotonin in the Presence of Ascorbate”. In: *Analytical Chemistry* 78, pp. 6990–6998.
- Anna, S. L., N. Bontoux, and H. A. Stone (2003). “Formation of dispersions using flow focusing in microchannels”. In: *Applied Physics Letters* 82.3, pp. 364–366.
- Aris, R. (1956). “On the Dispersion of a Solute in a Fluid Flowing through a Tube”. In: *Proceedings of the Royal Society A: Mathematical, Physical and Engineering Sciences*. 1200, pp. 67–77.
- Armstrong-James, Michael and Julian Millar (1979). “Carbon fibre microelectrodes”. In: *Journal of Neuroscience Methods* 1.3, pp. 279–287.
- Azevedo, Frederico A.C. et al. (2009). “Equal numbers of neuronal and nonneuronal cells make the human brain an isometrically scaled-up primate brain”. In: *The Journal of Comparative Neurology* 513.5, pp. 532–541.

## Bibliography

---

- Baroud, Charles N, Francois Gallaire, and Rémi Dangla (2010). “Dynamics of microfluidic droplets.” In: *Lab on a chip* 10.16, pp. 2032–2045.
- Bassous, E., H. H. Taub, and L. Kuhn (1977). “Ink jet printing nozzle arrays etched in silicon”. In: *Applied Physics Letters* 31.2, pp. 135–137.
- Becker, J Sabine, Andreas Matusch, et al. (2010). “Bioimaging of metals in brain tissue by laser ablation inductively coupled plasma mass spectrometry (LA-ICP-MS) and metallomics.” en. In: *Metallomics : integrated biometal science* 2.2, pp. 104–11.
- Becker, J Sabine, Miroslav Zoriy, et al. (2010). “Bioimaging of metals by laser ablation inductively coupled plasma mass spectrometry (LA-ICP-MS).” In: *Mass spectrometry reviews* 29.1, pp. 156–75.
- Becker, J. Sabine et al. (2007). “Laser ablation inductively coupled plasma mass spectrometry (LA-ICP-MS) in elemental imaging of biological tissues and in proteomics”. In: *Journal of Analytical Atomic Spectrometry* 22.7, p. 736.
- Bédurier, Amélie et al. (2015). “Detection of Alzheimer’s disease amyloid-beta plaque deposition by deep brain impedance profiling”. In: *Journal of Neural Engineering* 12.2, p. 024001.
- Benveniste, Helene et al. (1984). “Elevation of the Extracellular Concentrations of Glutamate and Aspartate in Rat Hippocampus During Transient Cerebral Ischemia Monitored by Intracerebral Microdialysis”. In: *Journal of Neurochemistry* 43.5, pp. 1369–1374.
- Berdondini, Luca et al. (2009). “Active pixel sensor array for high spatio-temporal resolution electrophysiological recordings from single cell to large scale neuronal networks”. In: *Lab on a Chip* 9.18, p. 2644.
- Birdi, K. S., D. T. Vu, and A. Winter (1989). “A Study of the Evaporation Rates of Small Water Drops Placed on a Solid Surface”. In: *J. Phys. Chem.* 93.1, pp. 3702–3703.
- Bogue, R (2013). “Recent developments in MEMS sensors: a review of applications, markets and technologies”. In: *Sensor Review* 33.4, pp. 300–304.
- Boron, Walter F. and Emile L. Boulpaep (2017). *Medical physiology*. Elsevier, p. 1312.

- Bourne, James A. (2003). "Intracerebral microdialysis: 30 years as a tool for the neuroscientist". In: *Clinical and Experimental Pharmacology and Physiology* 30.1-2, pp. 16–24.
- Bragin, A. et al. (1995). "Gamma (40-100 Hz) oscillation in the hippocampus of the behaving rat." In: *The Journal of neuroscience : the official journal of the Society for Neuroscience* 15.1 Pt 1, pp. 47–60.
- Bredesen, Dale E (2009). "Neurodegeneration in Alzheimer's disease: caspases and synaptic element interdependence." In: *Molecular neurodegeneration* 4, p. 27.
- Bretherton, F. P. (1961). "The motion of long bubbles in tubes". In: *Journal of Fluid Mechanics* 10.02, p. 166.
- Bruus, Henrik. (2008). *Theoretical microfluidics*. Oxford University Press, p. 346.
- Bui, Minh-Phuong Ngoc et al. (2011). "Enzyme Kinetic Measurements Using a Droplet-Based Microfluidic System with a Concentration Gradient". In: *Analytical Chemistry* 83.5, pp. 1603–1608.
- Burdette, Shawn C and Stephen J Lippard (2003). "Meeting of the minds: metallo-neurochemistry." In: *Proceedings of the National Academy of Sciences of the United States of America* 100.7, pp. 3605–10.
- Campbell, P. K. et al. (1991). "A silicon-based, three-dimensional neural interface: Manufacturing processes for an intracortical electrode array". In: *IEEE Transactions on Biomedical Engineering* 38.8, pp. 758–768.
- Carson, Stephen et al. (2015). *Ericsson Mobility Report*. Tech. rep., pp. 4–7.
- Cepeda, David E. et al. (2015). "Experimental evaluation and computational modeling of tissue damage from low-flow push–pull perfusion sampling in vivo". In: *Journal of Neuroscience Methods* 242, pp. 97–105.
- Chapman, P H, E R Cosman, and M A Arnold (1990). "The relationship between ventricular fluid pressure and body position in normal subjects and subjects with shunts: a telemetric study." In: *Neurosurgery* 26.2, pp. 181–9.
- Chefer, Vladimir I et al. (2009). "Overview of brain microdialysis." In: *Current protocols in neuroscience* Chapter 7, Unit7.1.
- Chen, D. et al. (2008). "The chemistode: a droplet-based microfluidic device for stimulation and recording with high temporal, spatial, and chemical resolution."

## Bibliography

---

- In: *Proceedings of the National Academy of Sciences of the United States of America* 105.44, pp. 16843–48.
- Chen, J. et al. (1997). “A multichannel neural probe for selective chemical delivery at the cellular level”. In: *IEEE Transactions on Biomedical Engineering* 44.8, pp. 760–769.
- Chichkova, Rossitza I. and Lara Katzin (2010). “EMG and Nerve Conduction Studies in Clinical Practice”. In: *Practical Neurology* Jan-Feb, pp. 32–38.
- Chitravas, Numthip et al. (2011). “Treatable neurological disorders misdiagnosed as Creutzfeldt-Jakob disease”. In: *Annals of Neurology* 70.3, pp. 437–444.
- Cho, Sung-Hoon et al. (2008). “Biocompatible SU-8-Based Microprobes for Recording Neural Spike Signals From Regenerated Peripheral Nerve Fibers”. In: *IEEE Sensors Journal* 8.11, pp. 1830–1836.
- Chung, Y. T. et al. (2007). “In Vivo Monitoring of Multiple Trace Metals in the Brain Extracellular Fluid of Anesthetized Rats by Microdialysis-Membrane Desalter-ICPMS”. In: *Analytical chemistry* 79, pp. 8900–8910.
- Ciuti, Gastone et al. (2015). “MEMS Sensor Technologies for Human Centred Applications in Healthcare, Physical Activities, Safety and Environmental Sensing: A Review on Research Activities in Italy”. In: *Sensors* 15.3, pp. 6441–6468.
- Czosnyka, M and J D Pickard (2004). “Monitoring and interpretation of intracranial pressure.” In: *Journal of neurology, neurosurgery, and psychiatry* 75.6, pp. 813–821.
- De Witt Hamer, Philip C et al. (2012). “Impact of intraoperative stimulation brain mapping on glioma surgery outcome: a meta-analysis.” In: *Journal of clinical oncology : official journal of the American Society of Clinical Oncology* 30.20, pp. 2559–65.
- DeKosky, Steven T. and Kenneth Marek (2003). “Looking Backward to Move Forward: Early Detection of Neurodegenerative Disorders”. In: *Science* 302.5646, pp. 830–834.
- Dittrich, Petra S and Andreas Manz (2006). “Lab-on-a-chip: microfluidics in drug discovery.” In: *Nature reviews. Drug discovery* 5.3, pp. 210–218.
- Duffau, H et al. (2005). “Contribution of intraoperative electrical stimulations in surgery of low grade gliomas: a comparative study between two series without



- (1985-96) and with (1996-2003) functional mapping in the same institution.”  
In: *Journal of neurology, neurosurgery, and psychiatry* 76.6, pp. 845–51.
- Eric R. Kandel et al. (2013). *Principles of Neural Science, Fifth Edition* | *Neurology Collection* | McGraw-Hill Medical. Cenveo Publisher Services.
- Evans, Randolph W. (2009). “Diagnostic Testing for Migraine and Other Primary Headaches”. In: *Neurologic Clinics* 27.2, pp. 393–415.
- Feynman, Richard P. (1960). *There’s plenty of room at the bottom*. Tech. rep. Annual meeting of the American Physical Society - Caltech, 29th.
- Filler, Aaron G. (2009). *The History, Development and Impact of Computed Imaging in Neurological Diagnosis and Neurosurgery: CT, MRI, and DTI*. Tech. rep., pp. 1–76.
- Fontaine, Denys, Clement Hamani, and Andres Lozano (2009). “Efficacy and safety of motor cortex stimulation for chronic neuropathic pain: critical review of the literature”. In: *Journal of Neurosurgery* 110.2, pp. 251–256.
- Fuerstman, Michael J et al. (2007). “The pressure drop along rectangular microchannels containing bubbles.” In: *Lab on a chip* 7.11, pp. 1479–1489.
- Fukaya, Chikashi and Takamitsu Yamamoto (2015). “Deep Brain Stimulation for Parkinson’s Disease: Recent Trends and Future Direction”. In: *Neurologia medico-chirurgica* 55.5, pp. 422–431.
- Garris, Paul A. et al. (1997). “Real-time measurement of electrically evoked extracellular dopamine in the striatum of freely moving rats.” In: *J. Neurochem.* 68.1, pp. 152–61.
- Gasilova, Natalia et al. (2014). “On-Chip Spyhole Mass Spectrometry for Droplet-Based Microfluidics”. In: *Angewandte Chemie International Edition* 53.17, pp. 4408–4412.
- Gaylor, James M. et al. (2013). “Cochlear Implantation in Adults”. In: *JAMA Otolaryngology–Head & Neck Surgery* 139.3, p. 265.
- Gesteland, R.C. et al. (1959). “Comments on Microelectrodes”. In: *Proceedings of the Ire* 47.11, pp. 1856–62.

## Bibliography

---

- Grill, Warren M (2005). “Safety considerations for deep brain stimulation: review and analysis”. In: *Expert Review of Medical Devices* 2.4, pp. 409–420.
- Gu, Shuqing et al. (2014). “A droplet-based microfluidic electrochemical sensor using platinum-black microelectrode and its application in high sensitive glucose sensing”. In: *Biosensors and Bioelectronics* 55, pp. 106–112.
- Gupta, A. and R. Kumar (2009). “Effect of geometry on droplet formation in the squeezing regime in a microfluidic T-junction”. In: *Microfluidics and Nanofluidics* 8.6, pp. 799–812.
- HajjHassan, Mohamad, Vamsy Chodavarapu, and Sam Musallam (2008). “NeuroMEMS: Neural Probe Microtechnologies”. In: *Sensors* 8.10, pp. 6704–6726.
- Hampel, Harald et al. (2011). “The future of Alzheimer’s disease: The next 10 years”. In: *Progress in Neurobiology* 95.4, pp. 718–728.
- Han, Zuoyan, Yuen Yan Chang, et al. (2012). “Measuring rapid kinetics by a potentiometric method in droplet-based microfluidic devices”. In: *Chem. Commun.* 48.10, pp. 1601–1603.
- Han, Zuoyan, Wentao Li, et al. (2009). “Measuring Rapid Enzymatic Kinetics by Electrochemical Method in Droplet-Based Microfluidic Devices with Pneumatic Valves”. In: *Analytical Chemistry* 81.14, pp. 5840–5845.
- Hare, Dominic et al. (2009). “Quantitative elemental bio-imaging of Mn, Fe, Cu and Zn in 6-hydroxydopamine induced Parkinsonism mouse models”. In: *Metallomics* 1.1, pp. 53–58.
- Harris, E.J. and G. P. Burn (1948). “The transfer of sodium and potassium ions between muscle and the surrounding medium”. In: *Transactions of the Faraday Society* 45.1, pp. 508–528.
- Hauser, Robert A. (2009). “New considerations in the medical management of early Parkinson’s disease: Impact of recent clinical trials on treatment strategy”. In: *Parkinsonism & Related Disorders* 15, S17–S21.
- Hébert, Clément et al. (2015). “Microfabrication, characterization and in vivo MRI compatibility of diamond microelectrodes array for neural interfacing”. In: *Materials Science and Engineering: C* 46, pp. 25–31.

- Hodgkin, A L and A F Huxley (1952). "A quantitative description of membrane current and its application to conduction and excitation in nerve." In: *The Journal of physiology* 117.4, pp. 500–44.
- Hodgkin, A L and B Katz (1949). "The effect of sodium ions on the electrical activity of giant axon of the squid." In: *The Journal of physiology* 108.1, pp. 37–77.
- Jain, Samay, Steven E. Lo, and Elan D. Louis (2006). "Common Misdiagnosis of a Common Neurological Disorder". In: *Archives of Neurology* 63.8, p. 1100.
- Jankovic, J (2008). "Parkinson's disease: clinical features and diagnosis." In: *Journal of neurology, neurosurgery, and psychiatry* 79.4, pp. 368–76.
- Jerome, Engel Jr. et al. (2014). "EPILEPSY BIOMARKERS". In: 54.0 4, pp. 61–69.
- Jordan, John E. et al. (2014). "Acr - Asnr - Spr Practice Parameter for the Performance and Interpretation of Magnetic Resonance Imaging ( Mri ) of the Brain". In: 1076.Revised 2008, pp. 1–16.
- Jung, Wooseok et al. (2015). "Point-of-care testing (POCT) diagnostic systems using microfluidic lab-on-a-chip technologies". In: *Microelectronic Engineering* 132, pp. 46–57.
- Kelly, Ryan T. et al. (2009). "Dilution-Free Analysis from Picoliter Droplets by Nano-Electrospray Ionization Mass Spectrometry". In: *Angewandte Chemie International Edition* 48.37, pp. 6832–6835.
- Kennedy, R. T. (2013). "Emerging trends in in vivo neurochemical monitoring by microdialysis". In: *Current Opinion in Chemical Biology* 17.5, pp. 860–867.
- Kennedy, R. T., J. E. Thompson, and T. W. Vickroy (2002). "In vivo monitoring of amino acids by direct sampling of brain extracellular fluid at ultralow flow rates and capillary electrophoresis". In: *Journal of Neuroscience Methods* 114.1, pp. 39–49.
- Kilby, Jack S. (1959). *Miniaturized electronic circuits*.
- (1976). "Invention of the integrated circuit". In: *IEEE Transactions on Electron Devices* 23.7, pp. 648–654.

## Bibliography

---

- Kottegoda, Sumith, Imtiazuddin Shaik, and Scott A Shippy (2002). “Demonstration of low flow push-pull perfusion”. In: *Journal of Neuroscience Methods* 121.1, pp. 93–101.
- Kovacs, G. T. A. (1994). “Introduction to the Theory, Design and Modeling of Thin-Film Microelectrodes for Neural Interfaces”. In: *Enabling Technologies for Cultured Neural Networks*. Academic Press, pp. 121–166.
- Lee, Bruce and Andrew Newberg (2005). “Neuroimaging in traumatic brain imaging.” In: *NeuroRx : the journal of the American Society for Experimental NeuroTherapeutics* 2.2, pp. 372–83.
- Lee, Hyunjoo J. et al. (2015). “A multichannel neural probe with embedded microfluidic channels for simultaneous in vivo neural recording and drug delivery”. In: *Lab Chip* 15.6, pp. 1590–1597.
- Lee, Woong Hee, Thitaphat Ngernsutivorakul, et al. (2016). “Microfabrication and in Vivo Performance of a Microdialysis Probe with Embedded Membrane”. In: *Analytical Chemistry* 88.2, pp. 1230–1237.
- Lee, Woong Hee, Thomas R. Slaney, et al. (2013). “Microfabricated Sampling Probes for in Vivo Monitoring of Neurotransmitters”. In: *Analytical Chemistry* 85.8, pp. 3828–3831.
- Levie, R. de (1965). “The influence of surface roughness of solid electrodes on electrochemical measurements”. In: *Electrochimica Acta* 10, pp. 113–130.
- Li, Qiang et al. (2010). “Fraction collection from capillary liquid chromatography and off-line electrospray ionization mass spectrometry using oil segmented flow.” In: *Analytical chemistry* 82.12, pp. 5260–7.
- Lide, David R. (2004). *CRC Handbook of Chemistry and Physics*. Ed. by David R. Lide. CRC Press Inc.
- Lindsay, Solitaire et al. (2007). “Discrete microfluidics with electrochemical detection.” In: *The Analyst* 132.5, pp. 412–416.
- Ljungberg, T. and U. Ungerstedt (1978). “Classification of neuroleptic drugs according to their ability to inhibit apomorphine-induced locomotion and gnawing: evidence for two different mechanisms of action.” In: *Psychopharmacology* 56.3, pp. 239–247.

- Marsden, C.D. (1990). "Parkinson's disease". In: *The Lancet* 335.8695, pp. 948–949.
- Matusch, Andreas et al. (2010). "Cerebral Bioimaging of Cu, Fe, Zn, and Mn in the MPTP Mouse Model of Parkinson's Disease Using Laser Ablation Inductively Coupled Plasma Mass Spectrometry (LA-ICP-MS)". In: *Journal of the American Society for Mass Spectrometry* 21.1, pp. 161–171.
- Maynard, E. M., C. T. Nordhausen, and R. A. Normann (1997). "The Utah Intracortical Electrode Array: A recording structure for potential brain-computer interfaces". In: *Electroencephalography and Clinical Neurophysiology* 102.3, pp. 228–239.
- McHale, G. et al. (2005). "Analysis of droplet evaporation on a superhydrophobic surface". In: *Langmuir* 21.24, pp. 11053–11060.
- McIntyre, Cameron C et al. (2004). "Uncovering the mechanism(s) of action of deep brain stimulation: activation, inhibition, or both". In: *Clinical Neurophysiology* 115.6, pp. 1239–1248.
- Mercanzini, A., K. Cheung, et al. (2007). "Demonstration of cortical recording and reduced inflammatory response using flexible polymer neural probes". In: *2007 IEEE 20th International Conference on Micro Electro Mechanical Systems (MEMS)*. 21-25, pp. 573–576.
- Mercanzini, A., P. Colin, et al. (2009). "In vivo electrical impedance spectroscopy of tissue reaction to microelectrode arrays." In: *IEEE transactions on bio-medical engineering* 56.7, pp. 1909–1918.
- Mercer, H D and R L White (1978). "Photolithographic fabrication and physiological performance of microelectrode arrays for neural stimulation." In: *IEEE transactions on bio-medical engineering* 25.6, pp. 494–500.
- Merrill, Daniel R and Patrick A Tresco (2005). "Impedance characterization of microarray recording electrodes in vitro." In: *IEEE transactions on bio-medical engineering* 52.11, pp. 1960–5.
- Metz, S., A. Bertsch, et al. (2004). "Flexible polyimide probes with microelectrodes and embedded microfluidic channels for simultaneous drug delivery and multi-channel monitoring of bioelectric activity". In: *Biosensors and Bioelectronics* 19.10, pp. 1309–1318.

## Bibliography

---

- Metz, S., S. Jiguet, et al. (2004). "Polyimide and SU-8 microfluidic devices manufactured by heat-depolymerizable sacrificial material technique." In: *Lab on a chip* 4.2, pp. 114–20.
- Metz, S., F. Oppliger, et al. (2000). "Fabrication and test of implantable thin-film electrodes for stimulation and recording of biological signals". In: *1st Annual International IEEE-EMBS Special Topic Conference on Microtechnologies in Medicine and Biology*. 1, pp. 10–14.
- Michalke, Bernhard and Volker Nischwitz (2010). "Review on metal speciation analysis in cerebrospinal fluid-current methods and results: A review". In: *Analytica Chimica Acta* 682.1, pp. 23–36.
- Michel, Christoph M. and Micah M. Murray (2012). "Towards the utilization of EEG as a brain imaging tool". In: *NeuroImage* 61.2, pp. 371–385.
- Millar, Julian et al. (1985). "Electrochemical, pharmacological and electrophysiological evidence of rapid dopamine release and removal in the rat caudate nucleus following electrical stimulation of the median forebrain bundle". In: *European Journal of Pharmacology* 109.3, pp. 341–348.
- Minev, I. R et al. (2015). "Electronic dura mater for long-term multimodal neural interfaces". In: *Science* 347.6218, pp. 23–28.
- Miranda, Luís Felipe José Ravic et al. (2011). "Factors influencing possible delay in the diagnosis of Alzheimer ' s disease Findings from a tertiary Public University Hospital". In: *Dementia e Neuropsychologia* 5.4, pp. 328–331.
- Mirsattari, Seyed M, Teneille E Gofton, and Derek J Chong (2011). "Misdiagnosis of epileptic seizures as manifestations of psychiatric illnesses." In: *The Canadian journal of neurological sciences. Le journal canadien des sciences neurologiques* 38.3, pp. 487–493.
- Mocchegiani, Eugenio et al. (2005). "Brain, aging and neurodegeneration: Role of zinc ion availability". In: *Progress in Neurobiology* 75.6, pp. 367–390.
- Montgomery, Erwin B. and John T. Gale (2008). "Mechanisms of action of deep brain stimulation (DBS)". In: *Neuroscience & Biobehavioral Reviews* 32.3, pp. 388–407.
- Moos, Torben, Thomas Rosengren Nielsen, et al. (2007). "Iron trafficking inside the brain". In: *Journal of Neurochemistry* 103.5, pp. 1730–1740.

- Moos, Torben and Thomas Rosengren Nielsen (2006). "Ferroportin in the Postnatal Rat Brain: Implications for Axonal Transport and Neuronal Export of Iron". In: *Seminars in Pediatric Neurology* 13.3, pp. 149–157.
- Nemani, Krishnamurthy V. et al. (2013). "In vitro and in vivo evaluation of SU-8 biocompatibility". In: *Materials Science and Engineering: C* 33.7, pp. 4453–4459.
- Newman, J. (1966). "Resistance for Flow of Current to a Disk". In: *Journal of The Electrochemical Society* 113.5, pp. 501–02.
- Nordstrom, C H et al. (2003). "Assessment of the lower limit for cerebral perfusion pressure in severe head injuries by bedside monitoring of regional energy metabolism". In: *Anesthesiology* 98.4, pp. 809–814.
- Nordström, Carl-Henrik (2010). "Cerebral energy metabolism and microdialysis in neurocritical care". In: *Child's Nervous System* 26.4, pp. 465–472.
- Noyes, Katia and Bianca Weinstock-Guttman (2013). "Impact of diagnosis and early treatment on the course of multiple sclerosis". In: *American Journal of Managed Care* 19.17 SUPPL, pp. 321–331.
- Oregon, Daniel, Khellil Sefiane, and Martin E. R. Shanahan (2011). "Stick–Slip of Evaporating Droplets: Substrate Hydrophobicity and Nanoparticle Concentration". In: *Langmuir* 27.21, pp. 12834–12843.
- Pahwa, Rajesh and Kelly E Lyons (2010). "Early diagnosis of Parkinson's disease: recommendations from diagnostic clinical guidelines." In: *The American journal of managed care* 16 Suppl I, pp. 94–99.
- Paul, Bence et al. (2015). "Visualising mouse neuroanatomy and function by metal distribution using laser ablation-inductively coupled plasma-mass spectrometry imaging". In: *Chem. Sci.* 6.10, pp. 5383–5393.
- Paul, William and G. L. Pearson (1955). "Pressure Dependence of the Resistivity of Silicon". In: *Physical Review* 98.6, pp. 1755–1757.
- Pei, Jian et al. (2009). "Analysis of Samples Stored as Individual Plugs in a Capillary by Electrospray Ionization Mass Spectrometry". In: *Analytical Chemistry* 81.15, pp. 6558–6561.



## Bibliography

---

- Perry, Maura, Qiang Li, and Robert T. Kennedy (2009). “Review of recent advances in analytical techniques for the determination of neurotransmitters”. In: *Analytica Chimica Acta* 653.1, pp. 1–22.
- Peters, F. and D. Arabali (2013). “Interfacial tension between oil and water measured with a modified contour method”. In: *Colloids and Surfaces A: Physicochemical and Engineering Aspects* 426, pp. 1–5.
- Petersen, Ronald C (2009). “Early diagnosis of Alzheimer’s disease: is MCI too late?” In: *Current Alzheimer research* 6.4, pp. 324–30.
- Petit-Pierre, Guillaume, Arnaud Bertsch, and Philippe Renaud (2016). “Neural probe combining microelectrodes and a droplet-based microdialysis collection system for high temporal resolution sampling”. In: *Lab Chip* 16.5, pp. 917–924.
- Pfann, W. G. and R. N. Thurston (1961). “Semiconducting Stress Transducers Utilizing the Transverse and Shear Piezoresistance Effects”. In: *Journal of Applied Physics* 32.10, pp. 2008–2019.
- Picknett, R. G. and R. Bexon (1977). “The evaporation of sessile or pendant drops in still air”. In: *Journal of Colloid And Interface Science* 61.2, pp. 336–350.
- Porkka-Heiskanen, Tarja et al. (1997). “Adenosine: A Mediator of the Sleep-Inducing Effects of Prolonged Wakefulness”. In: *Science* 276.5316, pp. 1265–1268.
- Poser, C M (1997). “Misdiagnosis of multiple sclerosis and beta-interferon.” In: *Lancet (London, England)* 349.9069, p. 1916.
- Redgrave, Peter (1977). “A modified push-pull system for the localised perfusion of brain tissue”.
- Reitz, Christiane and Richard Mayeux (2014). “Alzheimer disease: Epidemiology, diagnostic criteria, risk factors and biomarkers”. In: *Biochemical Pharmacology* 88.4, pp. 640–651.
- Richardson, R.R., J.A. Miller, and W.M. Reichert (1993). “Polyimides as biomaterials: preliminary biocompatibility testing”. In: *Biomaterials* 14.8, pp. 627–635.
- Robichaud, Guillaume et al. (2013). “MSiReader: an open-source interface to view and analyze high resolving power MS imaging files on Matlab platform.” In: *Journal of the American Society for Mass Spectrometry* 24.5, pp. 718–21.



- Rodriguez, Francisco J. et al. (2000). "Polyimide cuff electrodes for peripheral nerve stimulation". In: *Journal of Neuroscience Methods* 98.2, pp. 105–118.
- Rossel, S., L. Gonzales, and L. Hernandez (2003). "One-second time resolution brain microdialysis in fully awake rats. Protocol for the collection, separation and sorting of nanoliter dialysate volumes." In: *Journal of Chromatography B* 784.2, pp. 385–93.
- Rousche, P. J. et al. (2001). "Flexible polyimide-based intracortical electrode arrays with bioactive capability". In: *IEEE Transactions on Biomedical Engineering* 48.3, pp. 361–370.
- Sabine Becker, J. (2013). "Imaging of metals in biological tissue by laser ablation inductively coupled plasma mass spectrometry (LA-ICP-MS): state of the art and future developments". In: *Journal of Mass Spectrometry* 48.2, pp. 255–268.
- Safford, R. E. (1977). "Calcium diffusion in transient and steady states in muscle". In: *Biophys J.* 20.1, pp. 113–136.
- Sall, Barry (2013). "Regulation of Medical Devices". In: *Madame Curie Bioscience Database*. Landes Bioscience.
- Sansuk, Siriwat et al. (2013). "Ultrasensitive Detection of Dopamine Using a Carbon Nanotube Network Microfluidic Flow Electrode". In: *Analytical Chemistry* 85.1, pp. 163–169.
- Schlieff, Michelle L. and Jonathan D. Gitlin (2006). "Copper Homeostasis in the CNS: A Novel Link Between the NMDA Receptor and Copper Homeostasis in the Hippocampus". In: *Molecular Neurobiology* 33.2, pp. 81–90.
- Seemann, R. et al. (2011). "Droplet based microfluidics". In: *Reports on Progress in Physics* 75.1, p. 016601.
- Seo, Jong-Mo et al. (2004). "Biocompatibility of polyimide microelectrode array for retinal stimulation". In: *Materials Science and Engineering: C* 24.1, pp. 185–189.
- Sexton, Daniel J (2011). *Lumbar puncture: Technique; indications; contraindications; and complications in adults*. Tech. rep., pp. 1–9.
- Shannon, Richard J et al. (2013). "Cerebral microdialysis in clinical studies of drugs: pharmacokinetic applications." In: *Journal of pharmacokinetics and pharmacodynamics* 40.3, pp. 343–58.

## Bibliography

---

- Shannon, Robert V. (1992). "A Model of Safe Levels for Electrical Stimulation". In: *IEEE Transactions on Biomedical Engineering* 39.4, pp. 424–426.
- Sharp, Andrew A et al. (2009). "In vivo penetration mechanics and mechanical properties of mouse brain tissue at micrometer scales." In: *IEEE transactions on bio-medical engineering* 56.1, pp. 45–53.
- Sheinerman, Kira S and Samuil R Umansky (2013). "Early detection of neurodegenerative diseases: circulating brain-enriched microRNA." In: *Cell cycle (Georgetown, Tex.)* 12.1, pp. 1–2.
- Shlamovitz, Gil Z (2007). *Lumbar puncture*. Tech. rep. November, pp. 2–5.
- Slaney, T. R. et al. (2011). "Push-Pull Perfusion Sampling with Segmented Flow for High". In: *Analytical Chemistry* 83, pp. 5207–13.
- Smith, Charles S. (1954). "Piezoresistance Effect in Germanium and Silicon". In: *Physical Review* 94.1, pp. 42–49.
- Soe, Aung K., Saeid Nahavandi, and Khashayar Khoshmanesh (2012). "Neuroscience goes on a chip". In: *Biosensors and Bioelectronics* 35.1, pp. 1–13.
- Solomon, Andrew J. and Brian G. Weinshenker (2013). "Misdiagnosis of Multiple Sclerosis: Frequency, Causes, Effects, and Prevention". In: *Current Neurology and Neuroscience Reports* 13.12, p. 403.
- Song, H., J. D. Tice, and R. F. Ismagilov (2003). "A microfluidic system for controlling reaction networks in time." In: *Angewandte Chemie International Edition* 42.7, pp. 768–72.
- Stefanis, Leonidas (2012). " $\alpha$ -Synuclein in Parkinson's disease." In: *Cold Spring Harbor perspectives in medicine* 2.2, a009399.
- Steigert, J et al. (2008). "A versatile and flexible low-temperature full-wafer bonding process of monolithic 3D microfluidic structures in SU-8". In: *Journal of Micromechanics and Microengineering* 18.9, p. 095013.
- Stieglitz (2004). "Electrode materials for recording and stimulation". In: *Neuroprosthetics: Theory and Practice*. Vol. 2. Series on Bioengineering and Biomedical Engineering. WORLD SCIENTIFIC, pp. 475–516.
- Stieglitz, T. et al. (2000). "Micromachined, Polyimide-Based Devices for Flexible Neural Interfaces". In: *Biomedical Microdevices* 2.4, pp. 283–294.

- Stone, J. et al. (2010). "Who is referred to neurology clinics?-The diagnoses made in 3781 new patients". In: *Clinical Neurology and Neurosurgery* 112.9, pp. 747–751.
- Su, C. K., T. W. Li, and Y. C. Sun (2008). "Online In-Tube Solid-Phase Extraction Using a Nonfunctionalized PVC Tube Coupled with ICPMS for in Vivo Monitoring of Trace Metals in Rat Brain Microdialysates". In: *Analytical Chemistry* 80.18, pp. 6959–6967.
- Su, Cheng Kuan et al. (2010). "In vivo monitoring of the transfer kinetics of trace elements in animal brains with hyphenated inductively coupled plasma mass spectrometry techniques". In: *Mass Spectrometry Reviews* 29.3, pp. 392–424.
- Sun, Shuwen and Robert T Kennedy (2014). "Droplet Electrospray Ionization Mass Spectrometry for High Throughput Screening for Enzyme Inhibitors." In: *Analytical chemistry* 86, pp. 9309–9314.
- Sun, Y. et al. (2009). "Assessment of the biocompatibility of photosensitive polyimide for implantable medical device use". In: *Journal of Biomedical Materials Research Part A* 90A.3, pp. 648–655.
- Sussulini, Alessandra et al. (2012). "Quantitative imaging of Cu, Fe, Mn and Zn in the L-DOPA-treated unilateral 6-hydroxydopamine Parkinson's disease mouse model by LA-ICP-MS". In: *Biomedical Spectroscopy and Imaging* 1.2, pp. 125–136.
- Sykova, Eva and Charles Nicholson (2009). "Diffusion in Brain Extracellular Space". In: 88.4, pp. 1277–1340.
- Takeda, Atsushi, Maki Hirate, et al. (2003). "Release of glutamate and GABA in the hippocampus under zinc deficiency". In: *Journal of Neuroscience Research* 72.4, pp. 537–542.
- Takeda, Atsushi, Akira Minami, et al. (2004). "Differential effects of zinc on glutamatergic and GABAergic neurotransmitter systems in the hippocampus". In: *Journal of Neuroscience Research* 75.2, pp. 225–229.
- Taylor, G. (1953). "Dispersion of Soluble Matter in Solvent Flowing Slowly through a Tube". In: *Proceedings of the Royal Society A: Mathematical, Physical and Engineering Sciences* 219.1137, pp. 186–203.

## Bibliography

---

- Terzuolo, C a and T Araki (1961). “An analysis of intra- versus extracellular potential changes associated with activity of single spinal motoneurons.” In: *Annals of the New York Academy of Sciences* 94, pp. 547–558.
- Tilson, H. A. and S. B. Sparber (1970). “On the use of the push-pull cannula as a means of measuring biochemical changes during ongoing behavior”. In: *Behavior Research Methods & Instrumentation* 2.3, pp. 131–134.
- Timofeev, I. et al. (2011). “Cerebral extracellular chemistry and outcome following traumatic brain injury: a microdialysis study of 223 patients”. In: *Brain* 134.2, pp. 484–494.
- Tsivgoulis, Georgios and Andrei V. Alexandrov (2016). “Ultrasound in Neurology”. In: *continuum: Lifelong Learning in Neurology* 22.5, pp. 1655–1677.
- Tufte, O. N., P. W. Chapman, and Donald Long (1962). “Silicon Diffused-Element Piezoresistive Diaphragms”. In: *Journal of Applied Physics* 33.11, pp. 3322–3327.
- Van de Pol, F.C.M. et al. (1989). “A thermo-pneumatic actuation principle for a microminiature pump and other micromechanical devices”. In: *Sensors and Actuators* 17.1-2, pp. 139–143.
- Venton, B. J., T. E. Robinson, and R. T. Kennedy (2006). “Transient changes in nucleus accumbens amino acid concentrations correlate with individual responsivity to the predator fox odor 2,5-dihydro-2,4,5-trimethylthiazoline.” In: *Journal of neurochemistry* 96.1, pp. 236–46.
- Verzeano, M and K Negishi (1960). “Neuronal activity in cortical and thalamic networks.” In: *The Journal of general physiology* 43(6)Suppl, pp. 177–195.
- Vreeland, Richard F. et al. (2015). “Biocompatible PEDOT:Nafion Composite Electrode Coatings for Selective Detection of Neurotransmitters in Vivo”. In: *Analytical Chemistry* 87.5, pp. 2600–2607.
- Wang, J. (2000). “Survey and Summary: From DNA biosensors to gene chips”. In: *Nucleic Acids Research* 28.16, pp. 3011–3016.
- Wang, Xuewan et al. (2012). “A graphene–cobalt oxide based needle electrode for non-enzymatic glucose detection in micro-droplets”. In: *Chemical Communications* 48.52, p. 6490.

- Weast, Robert C. (1989). *CRC Handbook of Chemistry and Physics*.
- Williams, Justin C., Robert L. Rennaker, and Daryl R. Kipke (1999). "Long-term neural recording characteristics of wire microelectrode arrays implanted in cerebral cortex". In: *Brain Research Protocols* 4.3, pp. 303–313.
- Wong, Harris, C J Radke, and S Morris (1995). "The motion of long bubbles in polygonal capillaries. Part 2. Drag, fluid pressure and fluid flow". In: *Journal of Fluid Mechanics* 292.1995, pp. 95–110.
- Wu, Yuncheng, Weidong Le, and Joseph Jankovic (2011). "Preclinical Biomarkers of Parkinson Disease". In: *Archives of Neurology* 68.1, pp. 22–30.
- Xiang, Ling et al. (2014). "Vertically Aligned Carbon Nanotube-Sheathed Carbon Fibers as Pristine Microelectrodes for Selective Monitoring of Ascorbate in Vivo". In: *Analytical Chemistry* 86.8, pp. 3909–3914.
- Xie, Chong et al. (2015). "Three-dimensional macroporous nanoelectronic networks as minimally invasive brain probes". In: *Nature Materials* 14.12, pp. 1286–1292.
- Zachek, Matthew K. et al. (2010). "Microfabricated FSCV-compatible microelectrode array for real-time monitoring of heterogeneous dopamine release". In: *The Analyst* 135.7, p. 1556.
- Zapata, A. et al. (2009). "Detection and quantification of neurotransmitters in dialysates." In: *Current protocols in neuroscience* Chapter 7. Unit 7.4, pp. 1–30.
- Zatta, Paolo and Adrian Frank (2007). "Copper deficiency and neurological disorders in man and animals". In: *Brain Research Reviews* 54.1, pp. 19–33.
- Zeck, G and P Fromherz (2001). "Noninvasive neuroelectronic interfacing with synaptically connected snail neurons immobilized on a semiconductor chip." In: *Proceedings of the National Academy of Sciences of the United States of America* 98.18, pp. 10457–10462.
- Zetterstrom, T. and U. Ungerstedt (1984). "Effects of apomorphine on the in vivo release of dopamine and its metabolites, studied by brain dialysis". In: *European Journal of Pharmacology* 97.97, pp. 29–36.

## Bibliography

---

Zhang, Huifa et al. (2012). “Massively Parallel Single-Molecule and Single-Cell Emulsion Reverse Transcription Polymerase Chain Reaction Using Agarose Droplet Microfluidics”. In: *Analytical Chemistry* 84.8, pp. 3599–3606.

# Appendix A

## Appendix

### A.1 Probe Electrical Pairing Chart

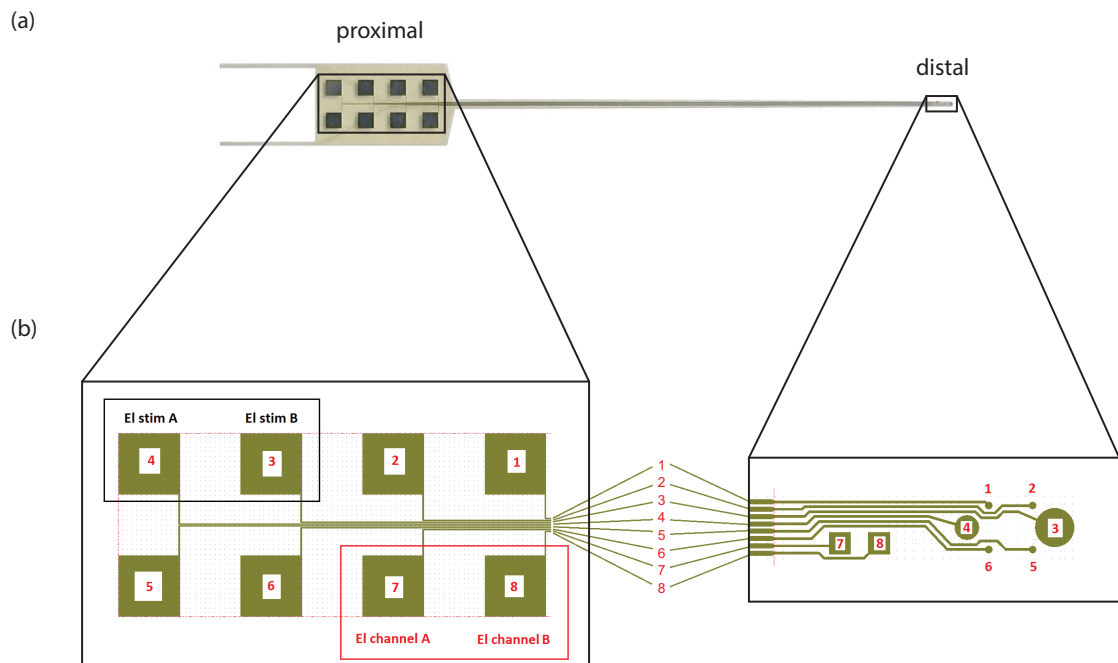


**Figure A.1** Chart of the pairing between the proximal contacts and the distal electrodes. (a) general view of the probe including the proximal and distal region. (b) Detail of the pairing. Each distal electrode is attributed to a proximal contact.

## A.2 Electrical Stimulation Pattern

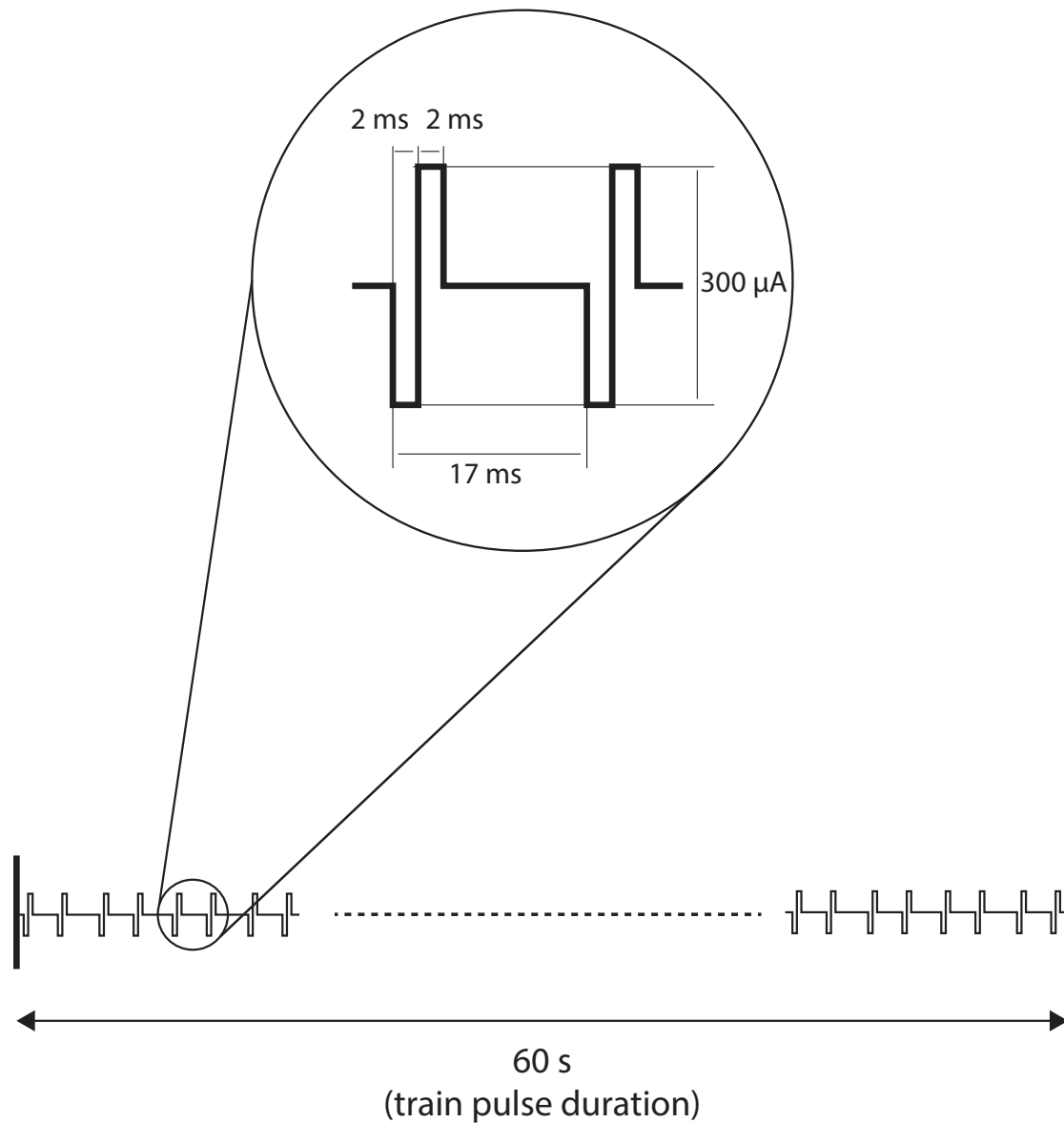


**Figure A.2** Detail of the electrical stimulation performed during the second *in vivo* experiment. Train of biphasic pulses of 300  $\mu\text{A}$  amplitude and 2 ms duration at a frequency of 60 Hz were delivered during 60 sec.



# List of Publications

## Papers included in this thesis

- *G. Petit-Pierre, A. Bertsch and P. Renaud.* "Neural probe combining microelectrodes and a droplet-based microdialysis system for high temporal resolution sampling", *Lab Chip.*, 16(5), pp 917-24, (2016)
- *G. Petit-Pierre, P. Colin, E. Laurer, J. Déglon, A. Bertsch, A. Thomas, B. L. Schneider and Philippe Renaud.* "In vivo neurochemical measurements in cerebral tissues using a droplet-based monitoring system", submitted (under peer-review process)
- *G. Petit-Pierre, P. Colin, E. Laurer, J. Déglon, A. Bertsch, A. Thomas, B. L. Schneider and P. Renaud.* "Cerebral tissues chemical neuromodulation in response to electrical stimulation", manuscript in preparation

## Conference proceedings

- *G. Petit-Pierre, A. Bertsch, P. Renaud.* "A novel neural probe for the direct sampling of extracellular fluid at high temporal and spatial resolution", *Nanobiotech Montreux*, (2015)
- *G. Petit-Pierre, C. Darbellay, A. Bertsch, P. Renaud.* "Droplet extraction module for the analysis of segmented flow generated by a neural probe", *RSC MicroTAS*, (2016)



# Curriculum Vitae



## Guillaume Petit-Pierre

PhD, Biotechnology & Bioengineering



Ch. des Cytises 17  
CH-1255 Veyrier  
Mobile: +41 (0)78 616 00 82  
guillaume.petit.pierre@gmail.com

Age 33  
Married

**French, English, German**

### OBJECTIVE

---

To share my creativity, my strong analytical background and my management skills in order to develop a startup company in medical technologies

### PROFESSIONAL EXPERIENCE

---

<b>EPF Lausanne</b>	<b>Research Assistant</b> PhD project in Biotechnology and Bioengineering LMIS4, group of <b>Prof. Philippe Renaud</b> <ul style="list-style-type: none"><li>• Development and management of multi-scale projects in the field of Neurotechnology.</li><li>• Brain interfaces design, <i>in vivo</i> signal recording, chemical and electrical stimulation</li><li>• Cleanroom microfabrication</li><li>• Teaching:<ul style="list-style-type: none"><li>- Lab work course: Microsystems and sensors</li><li>- 7 student projects supervised</li></ul></li></ul>	<b>2013 - 2017</b> (3 years, 10 months)
<b>Valtronic SA</b>	<b>Project Leader</b> Department of active implants, Les Charbonnières <ul style="list-style-type: none"><li>• Management of complex projects in the medical industry</li><li>• Supervision of a development engineer team (3-5 people)</li><li>• Design and development of high-end technology implants (class 3 medical devices)</li><li>• Process developments (Silicone and Epoxy over-moulding, laser micro-welding)</li><li>• Establishment of a new production line in cleanroom environment</li></ul>	<b>2010 - 2013</b> (2 years, 10 months)
<b>Zimmer GmbH</b>	<b>Research engineer, Internship</b> Department of Research on Materials, Winterthur <ul style="list-style-type: none"><li>• Study of knee prosthesis failure cases – interface implant/living tissues</li><li>• Design, development and realization of a custom tensile mechanical test</li><li>• Execution of experimental tests (under ISO standards requirements)</li><li>• Cost and time optimization of the fabrication processes</li></ul>	<b>2008</b> (4 months)

### EDUCATION

---

<b>EPF Lausanne</b>	<b>PhD, Biotechnology and Bioengineering</b>	<b>2013-2017</b>
<b>ETH Zurich</b>	<b>Master of Science, Mechanical engineering</b> Area of specialization: <b>Medical Technologies</b> <u>Master Thesis</u> : Development of a microfluidic manipulator device (MEMS)	<b>2007-2009</b>
<b>EPF Lausanne</b>	<b>Bachelor of Science, Mechanical engineering</b> <u>Bachelor Thesis</u> : Structural dynamic analysis of the “SwissCube” satellite	<b>2004-2007</b>

## LANGUAGES

---

<b>French</b>	Mother tongue
<b>English</b>	Fluent (C1, European standards)
<b>German</b>	Good knowledge (B2, European standards)

## COMPUTER SKILLS

---

CAD:	Solidworks, Catia V5, Pro Engineer
FEA:	Solidworks simulation, Abaqus, COMSOL multiphysics
Programming:	Matlab, Labview

## SCIENTIFIC PUBLICATIONS

---

- 2017(exp.)**      **Cerebral tissues chemical neuromodulation in response to electrical stimulation**, manuscript in preparation *Guillaume Petit-Pierre, Philippe Colin, Estelle Laurer, Julien Déglon, Arnaud Bertsch, Aurélien Thomas, Bernard L. Schneider and Philippe Renaud*
- 2017(exp.)**      **In vivo neurochemical measurements in cerebral tissues using a droplet-based monitoring system**, submitted, under peer-review. *Guillaume Petit-Pierre, Philippe Colin, Estelle Laurer, Julien Déglon, Arnaud Bertsch, Aurélien Thomas, Bernard L. Schneider and Philippe Renaud*
- 2016**              **Neural probe combining microelectrodes and a droplet-based microdialysis system for high temporal resolution sampling**, *Guillaume Petit-Pierre, Arnaud Bertsch and Philippe Renaud*, Lab Chip., 16(5), pp 917-24
- 2014**              **Rotation of fibers and other non-spherical particles by the acoustic radiation torque**, *Thomas Schwarz, Philipp Hahn, Guillaume Petit-Pierre and Jurg Dual*, Microfluidics and Nanofluidics, 18(1), pp 65-79
- 2013**              **Rotation of non-spherical micro-particles by amplitude modulation of superimposed orthogonal ultrasonic modes**, *Thomas Schwarz, Guillaume Petit-Pierre and Jurg Dual*, J Acoust Soc Am., 133(3), pp 1260-8

## PATENT

---

- 2016**              **Endoluminal nerve modulation device and methods for using thereof**  
*Guillaume Petit-Pierre, Philippe Renaud - Provisional - PCT/IB2016/053030*

## EXTRA-PROFESSIONAL ACTIVITIES

---

- |                    |  |                  |
|--------------------|--|------------------|
| <b>Aeronautics</b> | <b>Private Pilot</b> (PPL/A), training started at age 16   | from <b>2001</b> |
|                    | <b>Air tow Pilot</b> (towing of glider aircrafts), Montricher, Switzerland   | from <b>2007</b> |
| <b>Interests</b>   | <b>Ski mountaineering, hiking and climbing</b><br>(Participation to the "Patrouille des Glaciers" 2010, 2012, 2014 and 2016) |                  |

